

Fall 2007

# Development of a numerical model to predict impact forces on a North Atlantic right whale during collision with a vessel

Jason J. Raymond

*University of New Hampshire, Durham*

Follow this and additional works at: <https://scholars.unh.edu/thesis>

---

## Recommended Citation

Raymond, Jason J., "Development of a numerical model to predict impact forces on a North Atlantic right whale during collision with a vessel" (2007). *Master's Theses and Capstones*. 309.  
<https://scholars.unh.edu/thesis/309>

This Thesis is brought to you for free and open access by the Student Scholarship at University of New Hampshire Scholars' Repository. It has been accepted for inclusion in Master's Theses and Capstones by an authorized administrator of University of New Hampshire Scholars' Repository. For more information, please contact [nicole.hentz@unh.edu](mailto:nicole.hentz@unh.edu).

**DEVELOPMENT OF A NUMERICAL MODEL TO PREDICT  
IMPACT FORCES ON A NORTH ATLANTIC RIGHT WHALE  
DURING COLLISION WITH A VESSEL**

BY

**JASON J RAYMOND**  
B.S. University of Maine, 2001

THESIS

Submitted to the University of New Hampshire  
in Partial Fulfillment of  
the Requirements for the Degree of

Master of Science  
in  
Mechanical Engineering

September 2007

UMI Number: 1447901

### INFORMATION TO USERS

The quality of this reproduction is dependent upon the quality of the copy submitted. Broken or indistinct print, colored or poor quality illustrations and photographs, print bleed-through, substandard margins, and improper alignment can adversely affect reproduction.

In the unlikely event that the author did not send a complete manuscript and there are missing pages, these will be noted. Also, if unauthorized copyright material had to be removed, a note will indicate the deletion.

**UMI**<sup>®</sup>

---

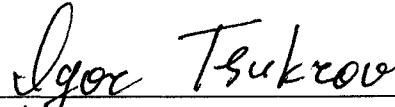
UMI Microform 1447901

Copyright 2007 by ProQuest Information and Learning Company.

All rights reserved. This microform edition is protected against unauthorized copying under Title 17, United States Code.

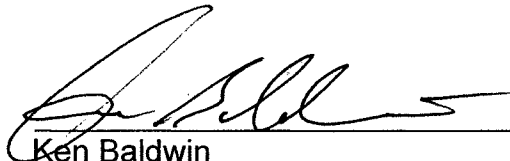
ProQuest Information and Learning Company  
300 North Zeeb Road  
P.O. Box 1346  
Ann Arbor, MI 48106-1346

This thesis has been examined and approved.



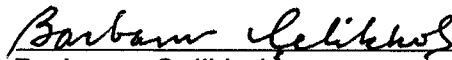
---

Igor Tsukrov  
Thesis Director  
Associate Professor of Mechanical Engineering



---

Ken Baldwin  
Professor of Ocean Engineering



---

Barbaros Celikkol  
Professor of Mechanical Engineering



---

Dr. Michael Moore  
Senior Research Specialist  
Woods Hole Oceanographic Institution

6/15/07

---

Date

## ACKNOWLEDGMENTS

First and foremost, I would like to express thanks to my advisor, Igor Tsukrov, for working with me throughout this process. I could not have completed this work without his guidance and patience. I would also like to express my sincere gratitude to Regina Campbell-Malone from the Woods Hole Oceanographic Institute. Her contributions were fundamental to my work from beginning to end. Additionally, I would like to thank the members of my graduate committee, Dr. Ken Baldwin, Dr. Barbaros Cellikol, and Dr. Michael Moore. I would also like to thank the National Oceanic and Atmospheric Administration Fisheries Department for providing funding of this work. Finally I would like to thank Elena for her support and understanding throughout this process.

## TABLE OF CONTENTS

ACKNOWLEDGEMENTS .....	iii
TABLE OF CONTENTS .....	iv
LIST OF TABLES.....	vi
LIST OF FIGURES .....	vii
ABSTRACT.....	ix

CHAPTER.....	PAGE
--------------	------

INTRODUCTION .....	1
1. THEORETICAL FOUNDATION AND MODELING TOOLS .....	6
1.1. Finite Element Analysis (FEA).....	6
1.2. Selection of modeling tool .....	7
1.2.1. ALGOR.....	7
1.2.2. MSC.Dytran.....	8
1.2.3. MSC.Marc/Mentat.....	9
1.3. Hyperelastic material models .....	10
1.4. Verification using classical methods.....	12
1.5. Dynamic analysis .....	14
1.5.1. Houbolt integration scheme.....	15
1.5.2. Newmark-Beta integration scheme.....	16
2. DEVELOPMENT OF THE WHALE MODEL.....	17
2.1. Geometric model.....	17
2.2. Modeling of material properties .....	23
2.2.1. Mechanical Properties of bone material .....	24
2.2.2. Soft tissue modeling .....	26
2.2.3. Epidermal Tissue.....	27
2.2.3.1. Compression test.....	27
2.2.3.2. Test Procedure .....	27
2.2.3.3. Experimental data processing.....	28
2.2.3.4. Validation using finite element analysis simulation .....	31
2.2.4. Fibroelastic tissue model .....	33
2.2.5. Equivalent linear elastic soft tissue model.....	36
2.3. Finite element mesh.....	38

3. DEVELOPMENT OF THE SHIP MODEL .....	42
3.1. Selection of hull geometry .....	42
4. NUMERICAL SIMULATION OF COLLISION.....	46
4.1. Parameters of numerical simulations .....	46
4.2. Initial conditions.....	47
4.2.1. 15-knot direct impact load case .....	50
4.2.2. 10-knot direct impact load case .....	50
4.2.3. 5-knot direct impact load case .....	50
4.2.4. 15-knot indirect impact with greater hull draft .....	50
4.3. Contact and boundary conditions.....	51
4.4. Hydrodynamics of ship approach .....	53
5. RESULTS OF SIMULATIONS.....	55
5.1. Data processing procedure to find surface loading on mandible.....	56
5.1.1. Determining the area of impact .....	56
5.1.2. Average impact stress .....	59
5.2. Summary of results .....	60
5.2.1. 15-knot direct impact collision results .....	61
5.2.2. 10-knot direct impact collision results .....	68
5.2.3. 5-knot direct impact collision results .....	72
5.2.4. 15-knot indirect impact with greater hull draft .....	76
5.3. Contact forces and overall dynamics of collision.....	78
5.4. Comparison of simulation results to classical dynamics solution .....	82
6. CONCLUSIONS AND RECOMMENDATIONS.....	84
6.1. Observations from modeling .....	84
6.2. Future work .....	85
6.2.1. Whale external geometry.....	86
6.2.2. Soft tissue model.....	86
6.2.3. Skeletal model .....	87
6.2.4. Dynamics and gravity forces .....	87
6.3. Implications for predicting fatal whale bone fractures.....	88
REFERENCES .....	89

## LIST OF TABLES

2.1. Eg2150 Necropsy data (Moore 2003, Appendix G) .....	18
2.2. Eg2150 Necropsy data (Moore 2003, Appendix H).....	19
2.3. Results summary for cortical bone mechanical testing .....	26
2.4. Summary of epidermal tissue material parameters for strain energy density functions.....	29
2.5. Percent error between material models and experimental data .....	33
2.6. Material parameters for 2-term Ogden soft tissue model .....	36
2.7. Summary of finite element mesh properties.....	41
5.1. Post-processing summary for determination of average impact loads.....	58
5.2. Summary of collision duration and impact force for direct impact cases.....	83



## LIST OF FIGURES

1.1. Image depicting the damage of sharp trauma resulting from a propeller strike (Photo by Robert Bonde).....	2
1.2. Fractured right whale mandible resulting from ship strike blunt trauma (Photo by Andrea Bogomolni).....	2
2.1. Representation of North Atlantic right whale .....	20
2.2. Geometric model of right whale .....	21
2.3. Scanned image of right whale skeleton (courtesy of Dr. Richard M. Levy, University of Calgary).....	22
2.4. Simplified solid model of right whale skeleton.....	23
2.5. Detail of right whale mandible bone section (Image by Regina Campbell-Malone) .....	24
2.6. Cross-section of right whale Eg2150 mandible (Image by Regina Campbell-Malone) .....	25
2.7. Experimental test specimen setup, epidermal tissue (photo by R. Campbell-Malone) .....	28
2.8. Uniaxial compression data for 0-20% compression range .....	30
2.9. Uniaxial compression data for 0-35% compression range .....	30
2.10. Finite element model of test specimen.....	32
2.11. Results comparison for finite element analyses of test specimen .....	33
2.12. Constitutive model curve fit for fibroelastic tissue data .....	34
2.13. Stress-Strain curve for modified specimen finite element model with 2-term Ogden material model .....	37
2.14. Finite element mesh section showing bone and soft tissue make-up .....	39
2.15. Rigid links connecting rostrum and spine.....	40
2.16. Right whale length to weight relationship. Figure 1.d from (Moore et al., 2005) .....	41
3.1. Typical Very Large Crude Carrier (VLCC) (photo by Frontline).....	43
3.2. Schematic of VLCC used to generate hull model (drawing by Frontline) ....	44
3.3. Hull model generated for use in numerical simulations.....	44
3.4. Photo depicting whale “hung up” on bulbous bow of vessel .....	45
4.1. Direct impact scenario, viewed from side.....	48
4.2. Direct impact scenario, viewed from beneath .....	49
4.3. Indirect impact scenario with hull having greater draft .....	49
4.4. Contact area applied to rigid hull surface for direct impact collision .....	52
4.5. Contact area applied to rigid hull surface for indirect impact collision .....	52
4.6. Contact area applied to the whale finite element mesh.....	53
5.1. Determination of mandible impact area – 15 knot load case .....	57
5.2. Detailed mandible model with impact area shown (Tsukrov et al., 2006) ....	59
5.3. Average impact stress on contact area of interest .....	60

5.4. 15-knot direct impact collision progression, full whale model.....	62
5.5. 15-knot direct impact, full whale maximum stress at t=0.140 sec .....	63
5.6. 15-knot direct impact collision progression, deformation of skeleton .....	64
5.7. 15-knot direct impact, skeleton maximum stress at t=0.140 sec.....	65
5.8. 15-knot direct impact collision progression, whale cross-section .....	66
5.9. 15-knot direct impact, cross-section maximum stress at t=0.140 sec .....	67
5.10. 10-knot direct impact collision progression, full whale model.....	69
5.11. 10-knot direct impact, full whale maximum stress at t=0.164 sec .....	70
5.12. 10-knot direct impact collision progression, deformation of skeleton .....	71
5.13. 10-knot direct impact, skeleton maximum stress at t=0.164 sec.....	72
5.14. 5-knot direct impact collision progression, full whale model.....	73
5.15. 5-knot direct impact, full whale maximum stress at t=0.216 sec .....	74
5.16. 5-knot direct impact collision progression, deformation of skeleton .....	75
5.17. 5-knot direct impact, skeleton maximum stress at t=0.216 sec.....	76
5.18. 15-knot indirect impact collision progression, full whale model.....	77
5.19. 15-knot indirect impact collision progression, skeleton deformation .....	78
5.20. Comparison of maximum impact force for direct impact load cases .....	79
5.21. Comparison of impact force to whale displacement during 15-knot collision event.....	81
5.22. Comparison of impact force to whale displacement during 10-knot collision event.....	81
5.23. Comparison of impact force to whale displacement during 5-knot collision event.....	82
6.1. Plot representing maximum impact for relative to vessel approach speed ..	85

## ABSTRACT

### DEVELOPMENT OF A NUMERICAL MODEL TO PREDICT IMPACT FORCES ON A NORTH ATLANTIC RIGHT WHALE DURING COLLISION WITH A VESSEL

by

Jason J. Raymond

University of New Hampshire, September, 2007

The North Atlantic right whale is under a great deal of public and private concern due to their endangered status and shrinking numbers. Of the 40 animals examined post-mortem (1970-2006), 21 deaths (52.5%) were caused by vessel-whale collision injuries, such as skull fractures. Several methods have been proposed to help reduce the number of fatalities. One such method is to place restrictions on ship speed within right whale critical habitats. However, no quantitative data exist regarding the effect of reduced vessel speed on the likelihood of fatality. The objective of this study is to develop a numerical model of the collision event to determine forces acting on the whale during impact. This will provide data on the mechanics of a ship-whale collision needed to form a basis for informed decisions regarding regulation of shipping traffic.

A representative three-dimensional finite element model of a whale has been developed using inputs from various sources. The mechanical properties of bone material and soft tissue were assigned based on experimental work and published data. The external geometry was created based on data available from necropsy findings. A simplified skeleton containing the major components was estimated based on the size of the external whale geometry. A surface model of a very large crude carrier was created as the representative hull model for the simulations. Since mandible fracture is assumed to be a fatal endpoint of collision, the relative positions of the whale and ship were chosen such that direct impact occurs on the mandible. Numerical simulations were performed for vessel approach speeds of 5, 8, 10, 12, and 15 knots. From the simulation results, the impact forces as a function of time and the overall collision dynamics can be determined. The resultant transient load curves can be applied to a detailed mandible model to predict what impact velocities result in mandible fracture.

## INTRODUCTION

North Atlantic right whales are one of the world's rarest mammals, with fewer than 400 whales remaining. Even with present efforts, the North Atlantic right whale has shown little signs of recovery despite over 50 years as a protected species. Efforts are being made to monitor and prevent the perceived decline of the right whale population. One of the main reasons attributed to causing the reduction in population are collisions with vessels. This, combined with fatalities caused by entanglement in fishing gear and a low rate of reproduction, threatens to further decrease the right whale population. A total of 71 confirmed right whale mortalities have been documented between 1970 and 2006 (Campbell-Malone et al., 2006, Campbell-Malone, 2007). Of the 40 animals examined post-mortem (1970-2006), 21 deaths (52.5%) were from ship strike. Injuries due to ship strike are separated into two distinct categories: 1) Sharp trauma resulting from propeller or rudder strike, 2) Blunt trauma resulting from direct hull contact. Figure 1.1 below illustrates the lacerations resulting from a propeller strike. Figure 1.2 shows a fractured mandible bone resulting from blunt trauma due to a ship strike. This damage due to blunt trauma was not apparent from external evidence. It was only discovered upon performing a complete necropsy of the whale carcass. Of the 21 carcasses displaying evidence of ship strike, 11 were found to result from sharp trauma, 9 from blunt trauma, and 1 confirmed ship strike for which the mechanism of trauma was unclear.

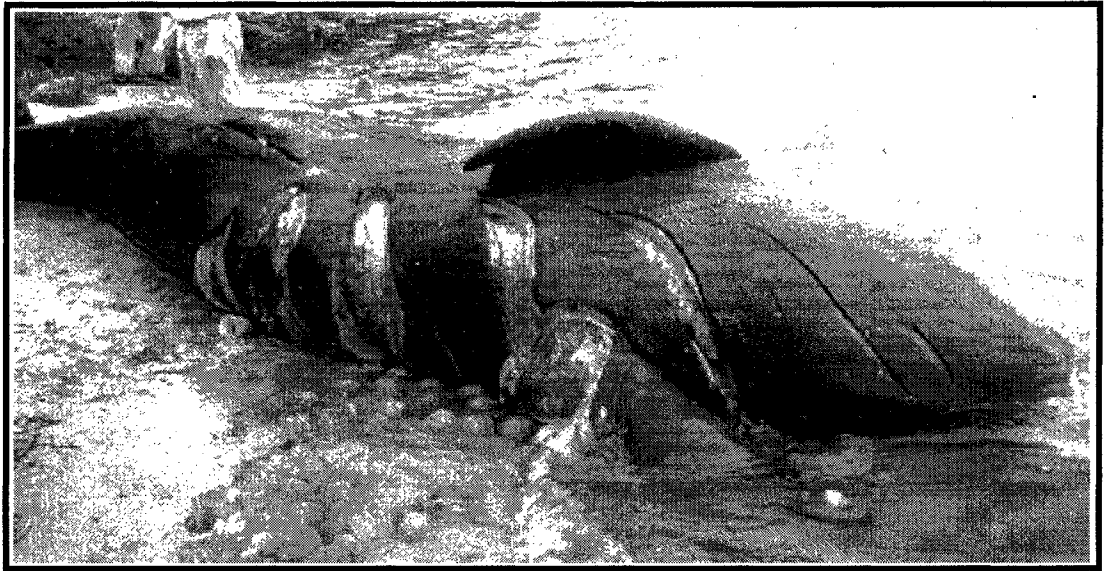


**Figure 1.1.** Image depicting the damage of sharp trauma resulting from a propeller strike (Photo by Robert Bonde)

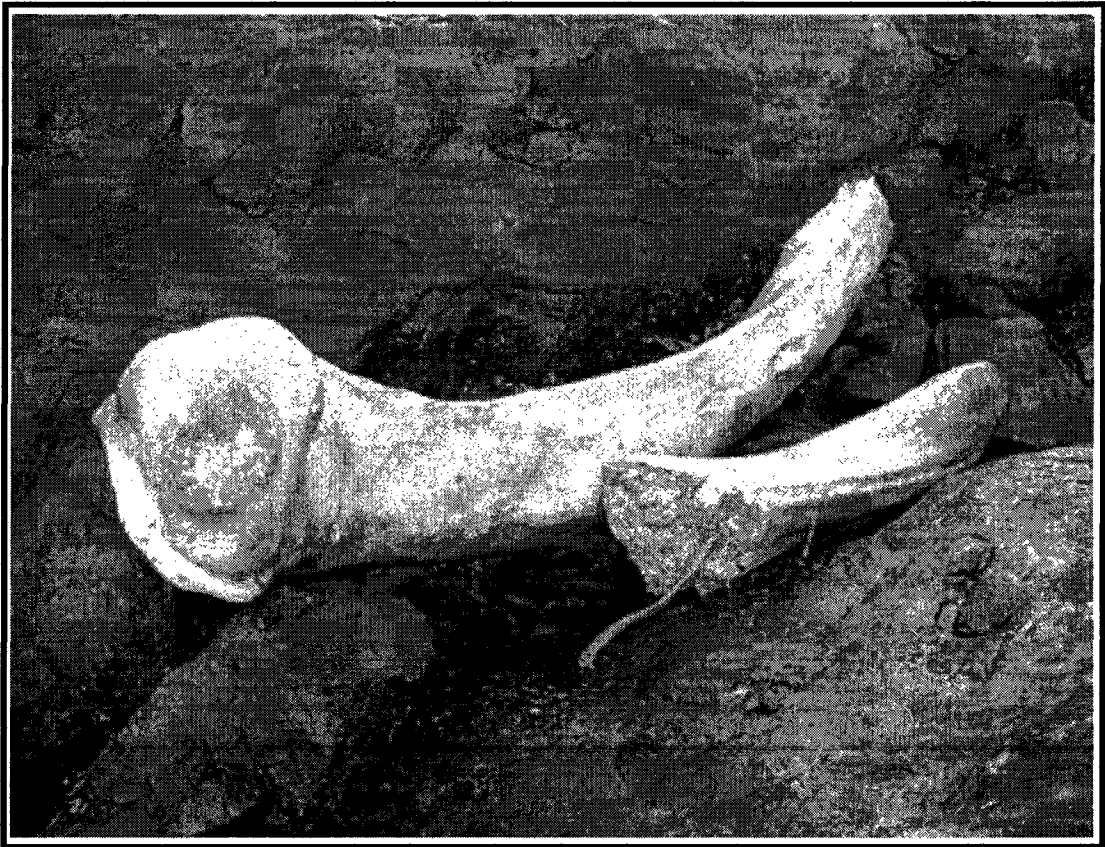


**Figure 1.2.** Fractured right whale mandible resulting from ship strike blunt trauma (Photo by Andrea Bogomolni)

Presently, there are a number of groups working to reduce the impact of the shipping industry on the right whale population. Along this vein, several solutions are being investigated. These include whale detection methods, acoustical deterrents, as well as modifications and regulations on shipping traffic. Though there are many detection possibilities being discussed, the problem remains as to what the clear directives of a ship will be once a whale has been detected in its path. Measures such as rerouting or providing alternate shipping lanes or the implementation of speed restrictions for ships in areas of high whale population are being explored. Canadian management agencies have successfully reduced the probability of encounter between ships and whales by relocating shipping lanes. Additionally, management agencies have proposed speed restrictions for vessels traversing right whale critical habitat. Presently, no quantitative data are available that would help to inform decisions regarding reasonable and effective reduction in vessel speed.

The nature of most existing models is to predict the probability of vessel-whale interaction in various areas of high right whale population. The models are based on data for past incidences and spatial relations between shipping lanes and right whale critical habitats. These models are effective for decisions regarding modification of shipping lanes and specification of areas in which speed restrictions should be applied. However, they do not give any indication of what would be effective limitations on vessel speed in these critical areas.

Laist et al. (2001) estimated fatal vessel-whale collision speeds using historical records of vessel activity. This was done by correlating the first reported

fatal collisions with the vessel speeds consistent with the time period that these collisions occurred. This is a useful estimate, however, it does not address the actual mechanics of a ship strike. The goal of this research is to generate a predictive model that accurately captures the dynamic properties of collisions between vessels and right whales. Providing a theoretical basis for determining the dynamics and forces involved in collisions with vessels allows for evaluation of the impact of vessel speed restriction on reduction of whale fatalities. This study hopes to supply some quantitative data to supplement studies on regulation to shipping traffic that would help reduce the chance of fatal collisions with right whales. This information could be a useful contribution to effective regulation of speed in right whale critical habitats.

Attempting to determine these impact forces using analytical methods of classical mechanics would fail to capture the complex dynamic characteristics involved. The simplifying assumptions required by classical methods would disregard the key phenomena of the vessel-whale collision dynamics, including large deformations and the whale inertia. By creating a numerical simulation that considers an extensive list of dynamic characteristics, the hope is to determine which collision scenarios are likely to result in fatality. Many factors must be considered in an effort to create the most useful model for approaching such a complex problem. Whale mass, ship velocity, approach characteristics, drag force, whale make-up (e.g. relative proportion and material properties of blubber, bone, skin, and other internal organs) are all factors that affect the dynamics of a ship strike. In this work, numerical simulations by finite element method were

used to analyze a variety of collision scenarios with different approach velocities and relative vessel-whale positions. Finite element analysis has the ability to predict dynamic forces and deformations during collisions for various velocities and geometries of whale and vessel, as well as implementing a number of linear and nonlinear material properties for whale tissue. By performing these simulations, a comprehensive set of data can be created which can be used to determine what types of speed restrictions might help reduce ship strike mortality of this highly endangered species.



## CHAPTER 1

### THEORETICAL FOUNDATION AND MODELING TOOLS

#### **1.1. Finite Element Analysis (FEA)**

Finite element analysis is based on the process of dividing complex structures into a discrete number of elements, referred to as a 'mesh'. The stiffness characteristics of the mesh relate forces to the displacements at the nodes forming each element. The equations that define the behavior of each element are combined into a system of simultaneous equations, which predict the nodal displacements within the complete structure. From these displacements, stresses and strains are calculated. The more elements used, by creating a finer mesh, the closer the mesh becomes to representing a continuous structure. However, this comes at a large cost of computer processing power, especially when considering the complexities involved when nonlinear characteristics are included. Numerical modeling of ship-whale collision includes geometric, material, and boundary condition nonlinearities.

Since nonlinear analysis is extremely computationally intensive, it is advised to begin modeling with simplified models involving coarse meshes. This reduces iteration time for improvements and refinements, as well as help with the overall understanding of the results obtained (MCS Software, 2005a). Once a satisfactory model with a convergent solution is obtained, mesh refinement can

be implemented to ensure that the nonlinearities are accurately captured.

## **1.2. Selection of modeling tool**

There are several commercially available software packages suited for running numerical finite element simulations. All have advantages and disadvantages depending on the analysts needs. Some are better suited for static structure analysis, while others are designed for analyses with a high level of numerical nonlinearity. Three software packages were considered for use in this study:

1. ALGOR with the Mechanical Event Simulator add-on.
2. MSC.Dytran (Explicit Dynamic Analysis)
3. MSC.Marc/Mentat (Nonlinear Analysis)

The following is a discussion of the advantages and disadvantages of each package with respect to the needs of this work.

### **1.2.1. ALGOR**

*ALGOR* is a general-purpose finite element package. The Mechanical Event Simulator (MES) is *ALGOR*'s explicit dynamics add-on. Mechanical Event Simulation combines large-scale motion and stress analysis and includes linear and nonlinear material models ([www.algor.com](http://www.algor.com)). Its main advantage is its robust user interface, which makes it relatively easy to use, with little to no training necessary. It is very easy to import solid geometries from a number of different CAD programs and quickly set up loads and boundary conditions. *ALGOR* has a large material library, which includes a number of hyperelastic material models, including Mooney-Rivlin, Arruda-Boyce, and Ogden constitutive models.

The disadvantages of *ALGOR* were encountered during the solution phase. There was little analysis output to review, and error messages did not give the user a clear picture of what may be causing solution trouble. This made troubleshooting difficult. Also, the lack of transparent control over solution parameters leaves the user with little idea what theoretical or numerical anomalies may be affecting the analysis solution. Another disadvantage was that the solve times seemed to be excessive, even for relatively simple models. This made iterating through various analysis parameters and model improvements cumbersome and time consuming.

### **1.2.2. MSC.Dytran**

*MSC.Dytran*® is a three-dimensional analysis code for analyzing the dynamic, nonlinear behavior of solid components, structures, and fluids. It uses explicit time integration and incorporates features that simulate a wide range of material and geometric nonlinearity (MSC Software, 2005b). It is well suited for short duration impact analyses. The dynamic solution parameters are relatively easy to set up. Preprocessing of the model, using MSC Software Corporation's preprocessor, *MSC.Patran*, is more difficult than with *ALGOR*®. However, the user has much more control over the solution settings. Though this is advantageous, it requires the user to gain a much greater understanding of the many solution parameters available in *MSC.Dytran*. The greatest advantage of *MSC.Dytran* with respect to this work is the ability to handle fluid/structure interaction. This would be very useful due to the drag effects that are present during a collision with a whale floating in the ocean.

The main disadvantage of *MSC.Dytran*® was that it had only one hyperelastic material model, the 2-term Mooney-Rivlin model. Post-processing turned out to be a troublesome task. The software was very unstable, and viewing analysis results was very difficult, as importing the result information generally resulted in the program shutting-down.

### **1.2.3. MSC.Marc/Mentat**

*MSC.Marc*® can be used to perform linear or nonlinear stress analysis in the static and dynamic regimes (MSC Software, 2005d). Its greatest advantage is its material library. *MSC.Marc*® is a favorite in the rubber and polymer industries. As such, it has been built to meet the requirements of customers in this field. *MSC.Marc*® has extensive options for hyperelastic materials in its material library. In addition to this, it has special element formulations and solvers specifically designed to handle the behavior and numerical treatment of incompressible materials (MSC Software, 2005c). *MSC.Marc*® also has support for defining rigid contact bodies from geometric surfaces. This precludes the need to generate a finite element mesh on bodies that are to be assumed completely rigid.

The main disadvantage of *MSC.Marc*® was that it was not specifically designed for dynamic analysis of short duration events involving collision and rigid body motion. Therefore, setting up the models can be cumbersome. Model pre-processing in *MSC.Mentat*® was not as user friendly as in some other software packages. Working with solid geometries, especially those with complex shapes, can be very difficult. Importing solid model geometries from CAD

packages is not as easy as it is with some other finite element analysis software packages.

Based on the above commentary, *MSC.Patran* was chosen for mesh generation and *MSC.Marc/Mentat* was chosen for the remainder of pre-processing, solution, and post-processing.

### **1.3. Hyperelastic material models**

In the analysis of rubbers and elastomers, there are a group of constitutive models referred to as hyperelastic. These models are derived to account for the unique behavior of compliant elastomeric materials such as:

1. Large deformations
2. High degree of nonlinearity
3. Near incompressibility

Hyperelastic material models are characterized by strain energy density functions,  $W$ . Use of these models requires the assumption that the material is elastic and isotropic. By taking the derivative of  $W$  in terms of strain, stress is obtained. Strain energy density functions are described in terms of either stretch ratios or strain invariants, defined as follows:

Stretch ratio:

$$\lambda = \frac{L}{L_0} = \frac{(L_0 + u)}{L_0} \quad (1)$$

where  $L_0$  is the initial length of the specimen, and  $u$  is the displacement due to loading.

Strain invariants:

$$I_1 = \lambda_1^2 + \lambda_2^2 + \lambda_3^2 \quad (2)$$

$$I_2 = \lambda_1^2 \lambda_2^2 + \lambda_2^2 \lambda_3^2 + \lambda_3^2 \lambda_1^2 \quad (3)$$

$$I_3 = \lambda_1^2 \lambda_2^2 \lambda_3^2 \quad (4)$$

where  $\lambda_1$ ,  $\lambda_2$ , and  $\lambda_3$  are the principal stretch ratios in three perpendicular directions.

There are a number of constitutive models available. Each one has advantages and disadvantages depending on test data available. The choice of model is based on the mode of deformation, maximum percent strain, and compressibility. Five strain energy density functions are considered for generating material models of soft tissue. They are:

- 2 term Mooney-Rivlin
- 3-term Mooney-Rivlin
- Arruda-Boyce
- Ogden
- Gent.

The strain energy functions for each of the constitutive models are presented below.

2-term Mooney-Rivlin:

$$W = C_{10}(I_1 - 3) + C_{01}(I_2 - 3) \quad (5)$$

3-term Mooney-Rivlin:

$$W = C_{10}(I_1 - 3) + C_{01}(I_2 - 3) + C_{11}(I_1 - 3)(I_2 - 3) \quad (6)$$

Arruda-Boyce:

$$W = nk\Theta \left[ \frac{1}{2}(I_1 - 3) + \frac{1}{20N}(I_1^2 - 9) + \frac{11}{1050N^2}(I_1^3 - 27) + \frac{19}{7000N^3}(I_1^4 - 80) + \frac{519}{673750N^4}(I_1^5 - 243) \right] \quad (7)$$

Gent:

$$W = \frac{-EI_m}{6} \log \left( \frac{I_m}{I_m - (I_1 - 3)} \right) \quad (8)$$

Ogden:

$$W = \sum_{n=1}^N \frac{\mu_n}{\alpha_n} J^{-\frac{\alpha_n}{3}} (\lambda_1^{\alpha_n} + \lambda_2^{\alpha_n} + \lambda_3^{\alpha_n} - 3) + 4.5K(J^{1/3} - 1)^2 \quad (9)$$

where J is the Jacobian measuring dilatancy.

Equations (5) through (9) represent how the strain energy density functions are implemented by MSC.Marc (MSC Software, 2005c). In these equations,  $C_{10}$ ,  $C_{01}$ ,  $C_{11}$ ,  $\mu_n$ ,  $\alpha_n$ ,  $nK\Theta$ ,  $N$ ,  $E$ ,  $I_m$  are the material parameters that are determined by MSC.Marc using the experimental test data. This procedure involves varying the material parameters to generate a stress-strain curve that best represents the experimental data. Depending on the material behavior and the data available, this procedure is met with varying degrees of success for the different constitutive models.

#### **1.4. Verification using classical methods**

When using numerical tools such as FEA, it is good practice to verify results with classical analytical methods. FEA is a complex tool, which opens the door for many possible errors to be introduced. The resulting solution is greatly dependent on the users input. Thorough understanding is needed to ensure that the analysis inputs, such as element formulations, material properties, and

boundary conditions, are reasonable. Otherwise the solution results might not represent the physical reality of the event being modeled. Hence, by comparing solution to proven methods, accuracy of the simulation can be verified. If a classical, closed-form solution of a simplified problem yields a result that is reasonably close to the simulation predictions, this is indication of sufficient accuracy of the simulation.

For the collision simulation, the theory of linear moment conservation is used as a verification tool. This theory, as described in (Hibbeler, 2006), is implemented as follows:

$$\Delta(mv) = F\Delta t \quad (10)$$

where  $m$  is the mass,  $v$  is the velocity,  $F$  is the impact force, and  $\Delta t$  is the time interval for the collision. For two objects, ship and whale, with initial and final velocities  $v_{si}$ ,  $v_{wi}$  and  $v_{sf}$ ,  $v_{wf}$ , correspondingly, equation (10) is expanded as follows:

$$(m_s v_{si} + m_w v_{wi}) - (m_s v_{sf} + m_w v_{wf}) = \int_0^t F dt \quad (11)$$

If it is assumed that the whale is initially at rest,  $v_{wi} = 0$ , and that the collision is completely inelastic,  $v_{wf} = v_{sf} = V'$ , equation (11) is reduced to:

$$m_s v_{si} - (m_s + m_w) V' = \int_0^t F dt \quad (12)$$

Once the numerical simulations are complete, the collision duration for each load case can be determined. This value, combined with the known velocity, whale mass, and ship mass, is then input into equation (12) to calculate the average impact force. This force is then compared with the results of the numerical analyses.



### **1.5. Dynamic analysis**

Since inertia plays a large role in the mechanics of the collision event, dynamic transient analysis is chosen to incorporate time-dependent response in the numerical model. Nonlinear analysis is required due to the use of contact surfaces and large displacements.

The finite element solution is obtained by applying the equation of motion to the finite element mesh and solving the resulting system of differential equations for the unknown displacement functions.

$$\mathbf{M}\ddot{\mathbf{u}} + \mathbf{C}\dot{\mathbf{u}} + \mathbf{K}\mathbf{u} = \mathbf{F}(t) \quad (13)$$

In this equation,  $\mathbf{M}$ ,  $\mathbf{C}$ , and  $\mathbf{K}$  are the mass, damping, and stiffness matrices, respectively,  $\mathbf{u}$  is the vector of unknown degrees of freedom (nodal displacements), and  $\mathbf{F}(t)$  is the force vector as a function of time.

MSC.Marc offers a number of schemes for performing numerical integration of this equation in time. The three implicit methods are Single-Step Houbolt, Newmark-Beta, and Modal Superposition. In addition, two explicit methods are offered. These are the Central Difference and Fast Central Difference methods. The explicit integration schemes are conditionally stable, requiring special considerations to determine an appropriate time step size,  $\Delta t$ , to maintain stability and accuracy. Therefore, these methods are limited to certain types of problems (i.e. short duration with a large number of increments). The implicit methods are unconditionally stable and can be used with a much larger  $\Delta t$  while maintaining accuracy. The following sections give a brief summary of the Houbolt and Newmark-Beta procedures as described by (Bathe, 1996).

### **1.5.1 Houbolt integration scheme**

For the Houbolt time integration scheme, standard finite difference expressions are used to approximate acceleration and velocity in terms of displacements. The following equations are employed:

$$\ddot{\mathbf{u}}(t + \Delta t) = \frac{1}{\Delta t^2} [2\mathbf{u}(t + \Delta t) - \mathbf{u}(t) + 4\mathbf{u}(t - \Delta t) - \mathbf{u}(t - 2\Delta t)] \quad (14)$$

$$\dot{\mathbf{u}}(t + \Delta t) = \frac{1}{6\Delta t} [11\mathbf{u}(t + \Delta t) - 18\mathbf{u}(t) + 9\mathbf{u}(t - \Delta t) - 2\mathbf{u}(t - 2\Delta t)] \quad (15)$$

Then, to obtain the solution at time  $(t+\Delta t)$ , we consider equation (13) at time  $(t+\Delta t)$ :

$$\mathbf{M}\ddot{\mathbf{u}}(t + \Delta t) + \mathbf{C}\dot{\mathbf{u}}(t + \Delta t) + \mathbf{K}\mathbf{u}(t + \Delta t) = \mathbf{F}(t + \Delta t) \quad (16)$$

Substituting equations (14) and (15) into equation (16) yields the solution for  $\underline{\mathbf{u}}(t+\Delta t)$ , as shown in equation (17).

$$\left( \frac{2}{\Delta t^2} \mathbf{M} + \frac{11}{6\Delta t} \mathbf{C} + \mathbf{K} \right) \mathbf{u}(t + \Delta t) = \mathbf{F}(t + \Delta t) + \left( \frac{5}{\Delta t^2} \mathbf{M} + \frac{3}{\Delta t} \mathbf{C} \right) \mathbf{u}(t) - \left( \frac{4}{\Delta t^2} \mathbf{M} + \frac{3}{2\Delta t} \mathbf{C} \right) \mathbf{u}(t - \Delta t) + \left( \frac{1}{\Delta t^2} \mathbf{M} + \frac{1}{3\Delta t} \mathbf{C} \right) \mathbf{u}(t - 2\Delta t) \quad (17)$$

This solution requires knowledge of velocity at time  $t$  and displacement at  $(t-\Delta t)$  and  $(t-2\Delta t)$ . For the analyses of this study, these velocity and displacement values are given by the initial conditions. The whale is initially at rest, and the vessel approaches at a prescribed velocity.

### **1.5.2 Newmark-Beta integration scheme**

The Newmark method uses the following finite difference approximations:

$$\dot{\mathbf{u}}(t + \Delta t) = \dot{\mathbf{u}}(t) + [(1 - \gamma)\ddot{\mathbf{u}}(t) + \gamma\ddot{\mathbf{u}}(t + \Delta t)]\Delta t \quad (18)$$

$$\mathbf{u}(t + \Delta t) = \mathbf{u}(t) + \dot{\mathbf{u}}(t)\Delta t + \left[ \left( \frac{1}{2} - \beta \right) \ddot{\mathbf{u}}(t) + \beta \ddot{\mathbf{u}}(t + \Delta t) \right] \Delta t^2 \quad (19)$$

In the above equations,  $\gamma$  and  $\beta$  are computational parameters chosen to obtain accuracy and stability. Equations (18) and (19) are combined with the equation of motion (16) at time  $(t + \Delta t)$ .

First, form the effective stiffness matrix,  $\mathbf{K}'$ , and the effective loads at time  $(t + \Delta t)$ ,  $\mathbf{R}'(t + \Delta t)$ , as follows:

$$\mathbf{K}' = \mathbf{K} + \left( \frac{1}{\beta \Delta t^2} \right) \mathbf{M} + \left( \frac{\gamma}{\beta \Delta t} \right) \mathbf{C} \quad (20)$$

$$\begin{aligned} \mathbf{R}'(t + \Delta t) = & \mathbf{R}(t + \Delta t) + \mathbf{M} \left( \frac{1}{\beta \Delta t^2} \mathbf{u}(t) + \frac{1}{\beta \Delta t} \dot{\mathbf{u}}(t) + \frac{1}{2\beta} \ddot{\mathbf{u}}(t) \right) + \\ & \mathbf{C} \left( \frac{\gamma}{\beta \Delta t} \mathbf{u}(t) + \left( \frac{\gamma}{\beta} - 1 \right) \dot{\mathbf{u}}(t) + \frac{\Delta t}{2} \left( \frac{\gamma}{\beta} - 2 \right) \ddot{\mathbf{u}}(t) \right) \end{aligned} \quad (21)$$

Then solve equation (19) for acceleration at time  $(t + \Delta t)$  resulting in equation (22) below:

$$\ddot{\mathbf{u}}(t + \Delta t) = \frac{1}{\beta \Delta t^2} (\mathbf{u}(t + \Delta t) - \mathbf{u}(t)) - \left( \frac{1}{\beta \Delta t} \right) \dot{\mathbf{u}}(t) - \left( \frac{1}{2} - \beta \right) \ddot{\mathbf{u}}(t) \quad (22)$$

Equations (18) and (22) are combined with equations (20) and (21) so that  $\mathbf{K}'$  and  $\mathbf{R}'$  are given in terms of known values.

Finally, find the displacements at  $(t + \Delta t)$  solving the system of linear equations expressed in equation (23) below.

$$\mathbf{K}' \mathbf{u}(t + \Delta t) = \mathbf{R}'(t + \Delta t) \quad (23)$$

## CHAPTER 2

### DEVELOPMENT OF WHALE MODEL

Development of the whale model included construction of solid models to represent the external geometry and the skeleton of the right whale, assignment of the corresponding material properties, and discretization of solids into a finite element mesh. The geometrical whale model developed for numerical simulations consisted of two parts: the skeleton and the outer shell representing blubber, muscle, and organs. The mechanical properties of the outer shell were approximated by the homogenized equivalent soft tissue properties chosen based on the experimental measurements. The methods used to obtain these data are described in subsequent sections. The skeleton was simplified and assigned a single representative material properties based on mechanical testing results. The skeletal and soft tissue geometries were subdivided into a finite element mesh and then combined to form a single solid finite element model with the appropriate material property distribution.

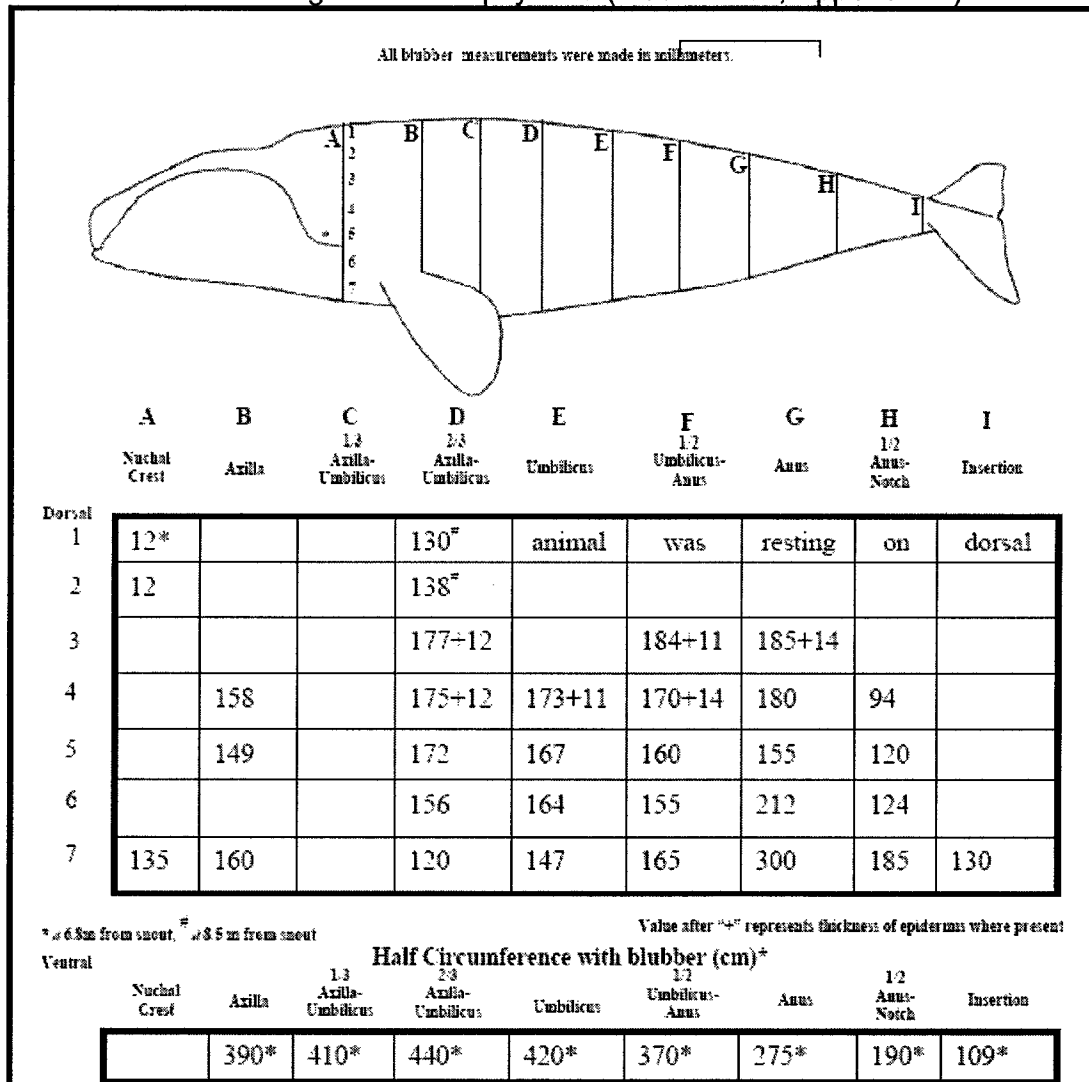
#### **2.1. Geometric Model**

The outer shape of the whale was generated using necropsy data for right whale Eg2150 (Moore, 2003). Tables 2.1 and 2.2 below are excerpted from appendices G and H of this report. These tables contain the measured girths at various points along the length of the whale.

**Table 2.1 Eg2150 Necropsy data (Moore 2003, Appendix G)**

<b>Straight Line Measurements</b>	
1. total length (tip to fluke notch)	1370 cm (44' 11" on ground, 45' 3" tape in air)
2. (to apex of melon)	n/a
3. (to gape of mouth)	361 cm
4. (to center of eye)	360 cm
5. (to center of blowhole)	CBD
6. (anterior insertion of pec. fin)	377 cm
7. (anterior insertion of dors. fin)	n/a
8. (to dorsal fin tip)	n/a
9. (to umbilicus)	740 cm
10. (to center of genital slit)	951 cm
11. (to center of anus)	1010 cm
12. fluke notch to anus	145* taken during blubber flensing
<b>Girths*</b>	*1/2 girth estimates → girth
13. axilla	390 cm → 780 cm
14. anterior insertion of dors. fin	420 cm → 840 cm
15. anus	275 cm → 550 cm
<b>Appendages</b>	
16. dorsal fin height	n/a
17. pect. fin anterior length	217 cm
18. pect. fin max width	145 cm
19. fluke width	511 cm
20. left fluke half width	272 cm
21. ant. leading edge left fluke	298 cm
22. Fluke half width	265.5 cm
23. peduncle to fluke notch	123 cm
<b>Tooth Counts</b>	
	n/a

**Table 2.2 Eg2150 Necropsy data (Moore 2003, Appendix H)**



The data from these tables was used to create a solid model in a computer-aided design (CAD) software program. The CAD software Solidworks® was chosen due to its ability to create geometries by using the “loft” feature to connect a number of cross-sections along a longitudinal axis. This was perfectly suited for use with the length and girth measurements available from the necropsy data. By creating circular sections representing the girth measurements, and orienting them at the given distances along a central axis, an

estimated representation of the whale was generated. Figure 2.1 shows the actual shape of a North Atlantic right whale. The solid model created from necropsy data is shown in figure 2.2.

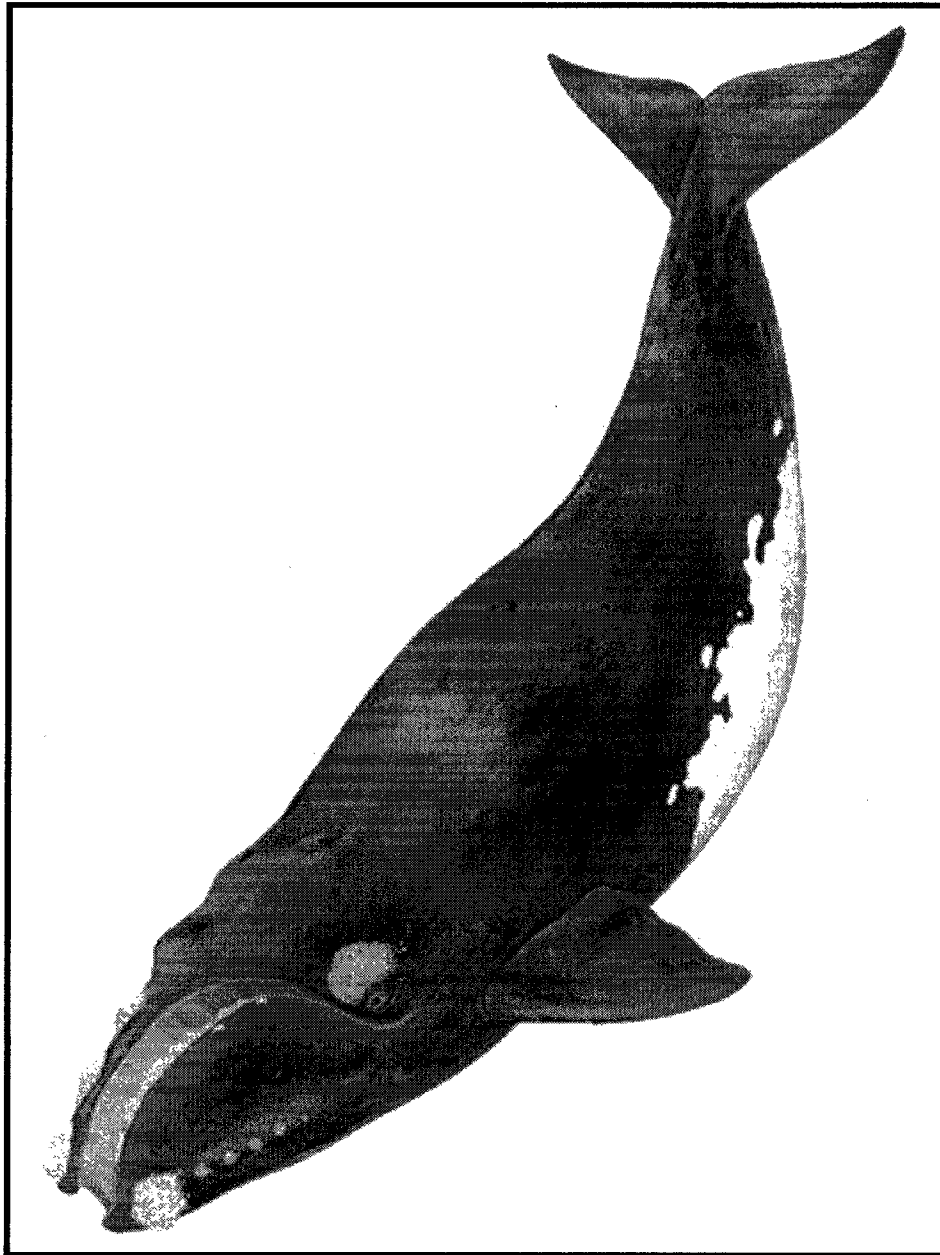


**Figure 2.1.** Representation of a North Atlantic right whale  
(Image by Jeffrey C. Domm, taken from [http://www.dfo-mpo.gc.ca/species-especes/species/fullSize\\_rightWhale\\_2\\_e.asp](http://www.dfo-mpo.gc.ca/species-especes/species/fullSize_rightWhale_2_e.asp))

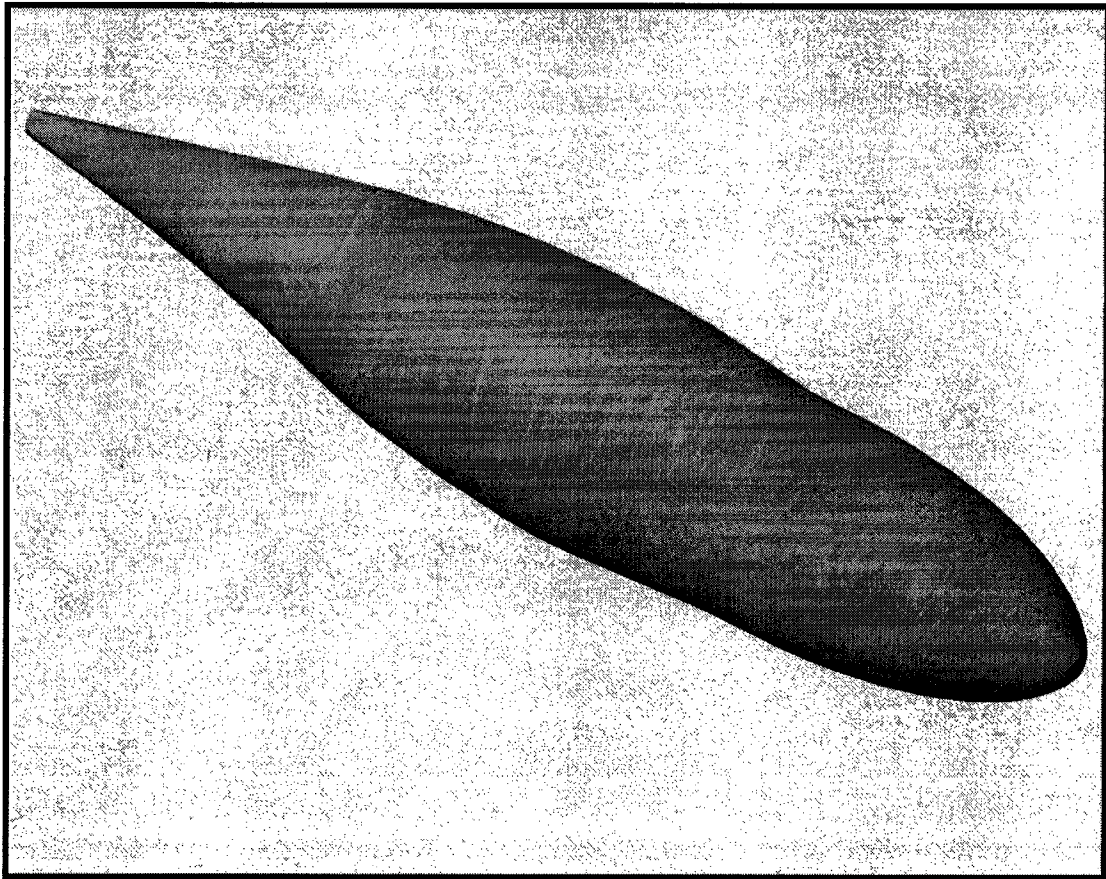


**Figure 2.2.** Geometric model of right whale

Since the necropsy was conducted on the shore with the whale ventral side up, some of the girth measurements may be inaccurate. Also, the surface model was generated assuming circular sections based on the girth measurements. This assumption was made due to lack of more detailed information. For these reasons, this model is not an exact representation of a right whale but it is a sufficient simplification for the purpose of numerical modeling.

The skeletal geometry was created using a scanned image of an actual right whale skeleton as a guide. This image is shown in figure 2.3. The dimensions were estimated based on the rough scale of each part and ensuring



that the skeletal components fit within the external surface created as described above. The resulting skeletal model, created using Solidworks® CAD software, is shown in figure 2.4. For the purpose of this study, mandible fracture was chosen to be the fatal endpoint for whale mortality (Campbell-Malone et al., 2006, Campbell-Malone, 2007). Some elements such as ribs and flippers were not included because of their minor relevance in terms of injuries in animals killed by ship strikes. The diameter of the mandible was assigned based on the dimensions of the whale mandible considered in (Tsukrov et al., 2006).

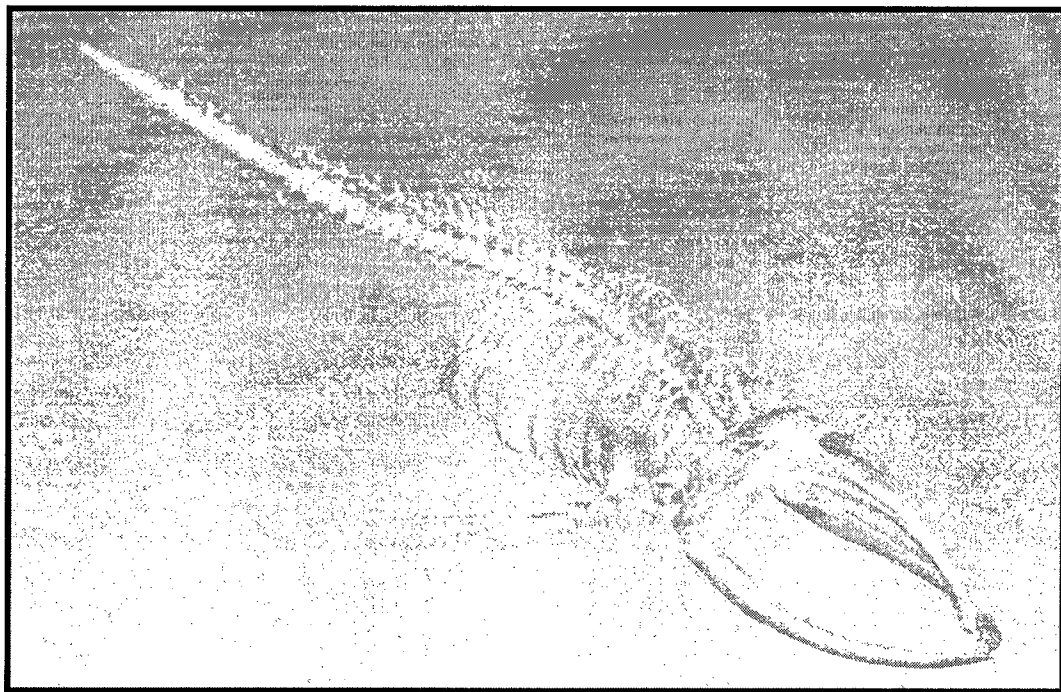


**Figure 2.3.** Scanned image of right whale skeleton (courtesy of Dr. Richard M. Levy, University of Calgary).

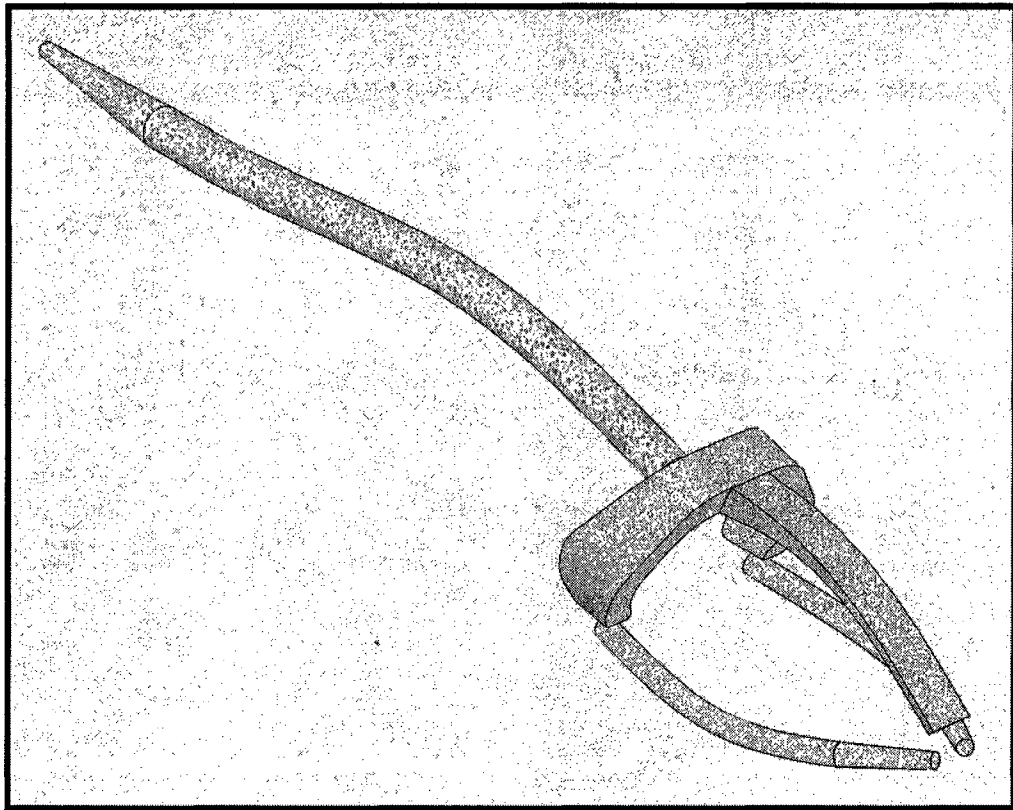


**Figure 2.4.** Simplified solid model of right whale skeleton.

## **2.2. Modeling of material properties**

To obtain useful results, adequate material models were needed to ensure that the dynamics of the collision event were accurately represented. One of the main goals was to determine the forces that act on the whale bones, particularly the mandible. To achieve this, the whale soft tissue needed to be modeled correctly to capture the dissipation of energy within the tissue, which reduces and distributes the load transferred to the bones. The overall whale mass was of concern to ensure that inertial effects were properly captured as inertia has a large effect on the amount of force transferred to the whale during the collision event.

### **2.2.1. Mechanical properties of bone material**

Concurrent studies are focusing on obtaining detailed information on the mechanical properties of the various materials that make the right whale mandible bone (Campbell-Malone, 2007, Tsukrov et al., 2006). The goal of their research is to produce detailed mechanical information for both the hard external bone, called cortical bone, and softer internal bone, called trabecular bone. Figures 2.5 and 2.6 are computed tomography (CT) scans showing details of a right whale mandible. Figure 2.5 shows the detailed external shape and the mandibular canal that runs along the inside of the bone. Figure 2.6 shows the bone cross-section, highlighting the distribution of trabecular and cortical bone.



**Figure 2.5.** Detail of right whale mandible section (Image by Regina Campbell-Malone)

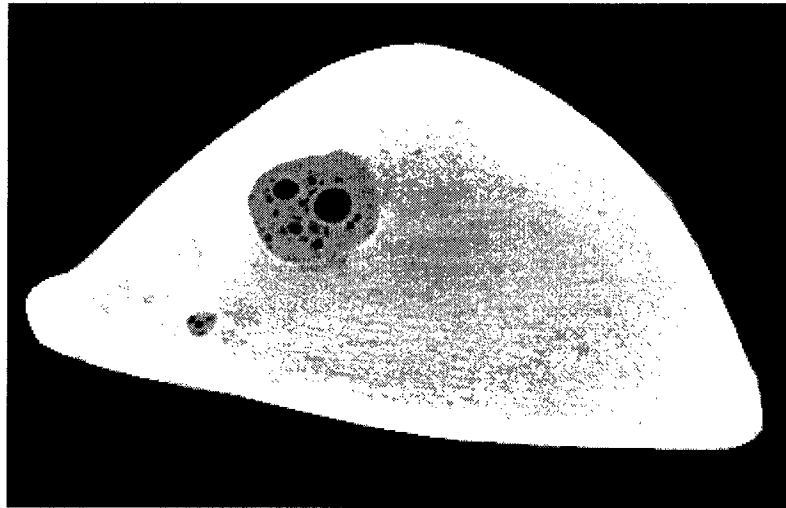


**Figure 2.6.** Cross-section of right whale Eg2150 mandible (Image by Regina Campbell-Malone).

The cortical bone is distinguished as the white area along the boundary of the cross-section. The trabecular bone is the light gray area throughout the middle portion of the cross-section. The dark gray areas are passages for blood vessels and nerves within the bone.

Due to the scale of the whale model generated, it was not feasible to include the amount of detail in the mandible bone depicted in the figures above. Rather, assumptions were required to predict the peak forces in the mandible while simplifying the skeletal model to a reasonable extent. For this study, the entire whale skeleton was represented using the cortical bone mechanical properties developed during the testing of (Campbell-Malone, 2007). Table 2.3 is a summary of these test results.

**Table 2.3** Results summary for cortical bone mechanical testing.

	<b>Elastic Modulus (MPa)</b>	<b>Ultimate Strength (MPa)</b>
<b>Maximum</b>	1360.4	51.7
<b>Minimum</b>	557.9	12.9
<b>Average</b>	854.2	22.9

Data provided by R. Campbell-Malone (WHOI/MIT)

This assumption was reasonable since the cortical bone provides the overall bone with the bulk of its stiffness. The trabecular bone is much softer and plays a minor role in the bones capability to resist load. Based on available data and the table above, the following values were chosen to numerically represent the whale skeleton.

$$E = 8.542e8 \text{ Pa}$$
$$\nu = 0.15$$
$$\rho = 1120 \text{ kg/m}^3,$$

where  $E$  is the elastic modulus,  $\nu$  is the Poisson's ratio, and  $\rho$  is the density.

### **2.2.2. Soft tissue modeling**

A great deal of testing was done to arrive at a satisfactory model to represent the whale soft tissue. Mechanical testing was performed on epidermal (skin) tissue and sub-dermal fibroelastic soft tissue. With these data, material models were generated to numerically represent the whale soft tissue mechanical behavior. For modeling the whale soft-tissue, both viscoelastic and hyperelastic material models were considered. The determination was made that rate-dependency was not needed for an accurate soft-tissue model since damping, or dissipation of the impact wave within the soft tissue, was assumed to have minimal effect on forces transmitted into the mandible bone as a result of impact. The decision was made that the whale soft tissue was best modeled as a

hyperelastic material. The behavior of this material is defined as a total stress-total strain relationship. Rather than following the linear elastic relationship defined by Hooke's law, the nonlinear elastic material response is formulated by a strain energy density function accounting for large strain components. The assumption is also made that the material is *isotropic* and *elastic*. There are a number of hyperelastic material models available. Those considered include the 2- and 3-term Mooney-Rivlin models, as well as the Ogden, Arruda-Boyce, and Gent models. The procedure for obtaining the test data and generating the material models is outlined below.

### **2.2.3. Epidermal tissue**

The first biological whale tissue considered was the epidermal tissue. This is the outer layer of skin, which is generally about 0.9-1.0 inches in thickness. The following describes the procedure used for mechanical testing of this material.

#### **2.2.3.1. Compression Test**

Testing was conducted to obtain experimental load-displacement data for right whale epidermal tissue (Campbell-Malone and Myers, 2006). A uniaxial compression test was conducted on an 8 mm diameter cylindrical sample of skin tissue taken from a flat sheet of tissue once overlaying the right whale jawbone. The initial gauge length of the specimen, with a preload of 0.5N, was 7.39 mm.

#### **2.2.3.2. Test Procedure**

Samples were tested on a Zwick/Roell load frame fitted with a 500N load cell. Initial pre-load of 0.05N was applied. Deformation at this pre-load defined

the initial gauge length ( $L_0$ ) of 7.39mm. This also defined the beginning of the compression test. The test was conducted with the specimen bathed in Phosphate Buffered Saline (1X-PBS). Figure 2.7 below shows the experimental setup. Each specimen test was run for three consecutive compression cycles.

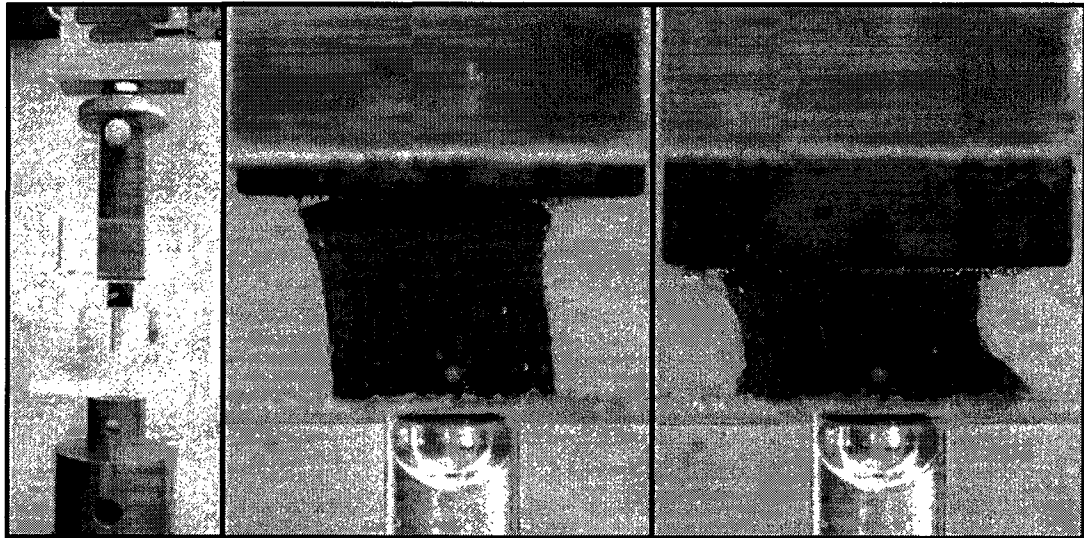


**Figure 2.7.** Experimental test specimen setup, epidermal tissue (photo by R. Campbell-Malone).

### **2.2.3.3. Experimental Data Processing**

The Experimental data was imported into Microsoft Excel®. The test procedure provided load-displacement data. The displacement data were converted to engineering strain by dividing the change in gauge length by the starting gauge length, determined as described above. Load data were converted to engineering stress by dividing the experimental load data by the cross-sectional area of the test specimen.

An engineering stress vs. engineering strain curve was generated for the 3-cycle test data. The first two cycles were for pre-conditioning. The final cycle data was taken as the expected material behavior.

*MSC.Mentat* was used to obtain the material parameters for the various strain energy density functions considered. For detailed definitions of each strain energy density function and their related material parameters, refer to chapter 1.3. Table 2.4 below summarizes the resulting material parameters for the various hyperelastic constitutive models considered. Figures 2.8 and 2.9 show the resulting curves, together with the experimental data curve, for both 20% and 35% compression, respectively. The figures show that there was little variation between the resulting curves for the different models considered. For both compression ranges, any of the available constitutive models would represent the experimental data well.

**Table 2.4.** Summary of epidermal tissue material parameters for strain energy density functions.

<b>MATERIAL MODEL</b>	<b>0-20% Strain Range</b>	<b>0-35% Strain Range</b>
<b>Mooney – 2 term</b>	$C_{10}$ : -0.178541	$C_{10}$ : 0.0289199
	$C_{01}$ : 0.204201	$C_{01}$ : 0.031866
<b>Mooney – 3 term</b>	$C_{10}$ : -0.774102	$C_{10}$ : -0.216635
	$C_{01}$ : 0.759372	$C_{01}$ : 0.246162
	$C_{11}$ : -0.306086	$C_{11}$ : -0.062553
<b>Ogden – 2 term</b>	$\mu_1$ : -0.293425	$\mu_1$ : 26.3377
	$\mu_2$ : 0.273137	$\mu_2$ : -13.6441
	$\alpha_1$ : -7.98495	$\alpha_1$ : -0.112239
	$\alpha_2$ : -8.03312	$\alpha_2$ : -0.233077
	Bulk Modulus: 11,342.8	Bulk Modulus: 15,340.6
<b>Arruda-Boyce</b>	$nK\theta$ : 9.9732e-9	$nK\theta$ : 0.0607923
	N: 0.0121811	N: 1.37702
<b>Gent</b>	E: 0.284446	E: 0.391752
	$I_m$ : 3.36211	$I_m$ : 5.94777



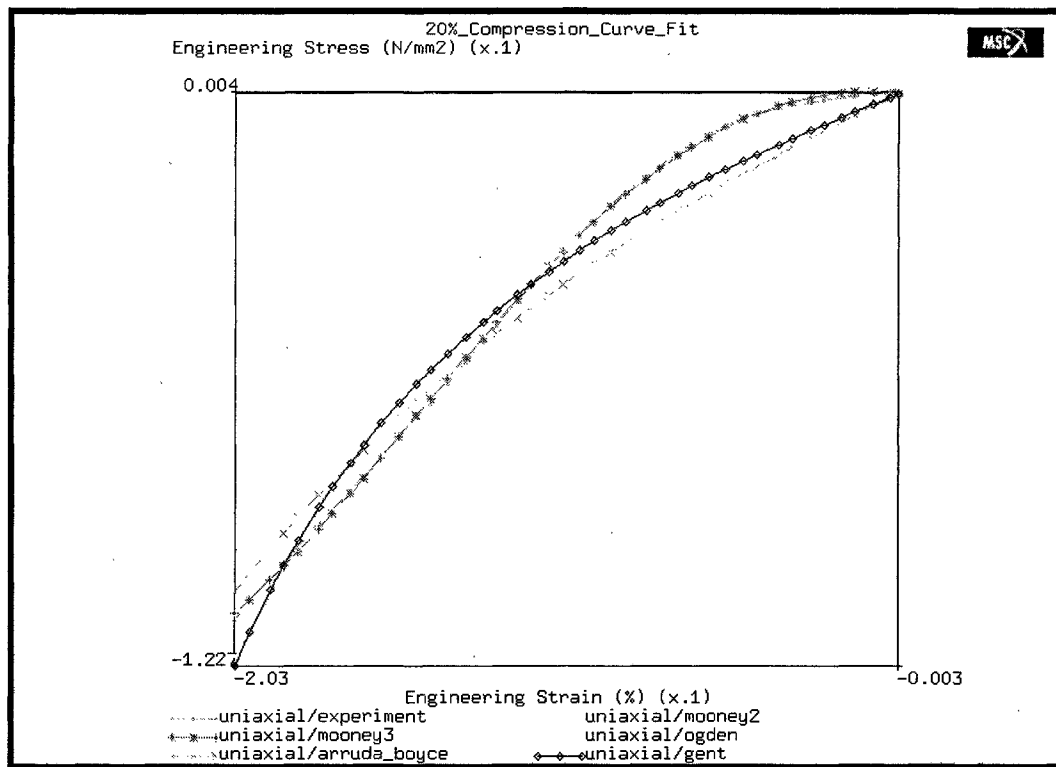


Figure 2.8. Uniaxial compression data for 0-20% compression range

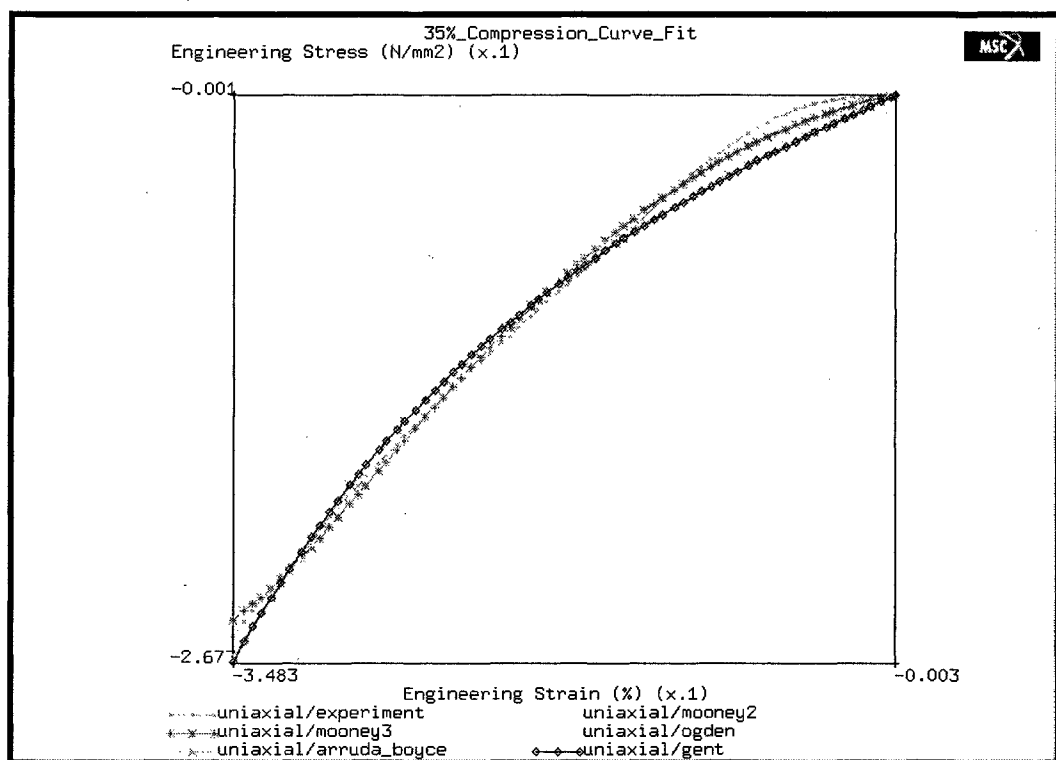


Figure 2.9. Uniaxial compression data for 0-35% compression range

#### **2.2.3.4. Validation using finite element analysis simulation**

To validate the material models derived from the experimental data, finite element analysis was used to numerically recreate the experiment. A model of the test specimen, shown in figure 2.10 (upper and lower contact surfaces shown transparent for clarity) was created in *MSC.Mentat*. This model consists of 759 nodes and 560 hexahedral elements (hex8). Analysis options were set for large displacement, large strain, and constant dilatation. A Full Integration Herrmann Element Formulation element type was used. The Herrmann element formulation was required to overcome analytical difficulties that arise when near-incompressibility is combined with nonlinearities such as large displacement, large strains, and contact. For the analyses using Arruda-Boyce and Gent material models, a large strain updated Lagrange procedure for rubber elasticity was required.

MSC.Marc was used to run a series of analyses for the material models generated with both 20% and 35% compression data. For both data sets, the numerical model was analyzed to 35% compression. This was done to verify the performance of the 20% compression data for compression ranges beyond that of the test data. The numerical results were then plotted and compared with the experimental results. It should be noted that, where there are missing material model curves, solution convergence could not be obtained.

For comparison to the experimental test data, history curves were created for the numerical model by extracting force and displacement data from the upper contact surface, which compresses the modeled sample. With these data,

curves were generated for “Displacement Z vs. Force Z”. This resulted in a load-displacement curve that was directly compared to the experimental data. Figure 2.11 shows the load-displacement plots of all of the material models when subjected to 35% compression. This plot clearly shows that the material models based on 20% compression data do not offer accurate results for compression beyond the tested compression range. All of the material models based on 35% compression data show good correlation to experimental results. Table 2.5 below lists the percent error between the various material models and the experimental data. This table compares the magnitude of the load between the test specimen and the various constitutive models at 35% compression. Evaluation of the load curves shows that any one of these material models is expected to offer similar results that accurately reflect experimental data.

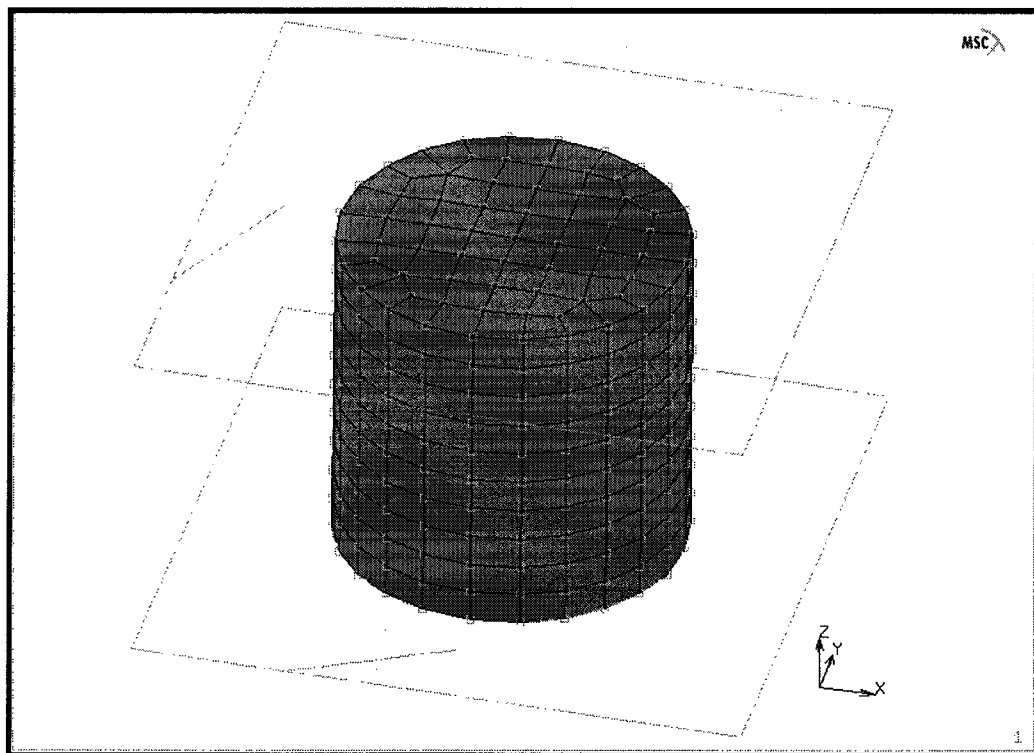


**Figure 2.10.** Finite element model of test specimen

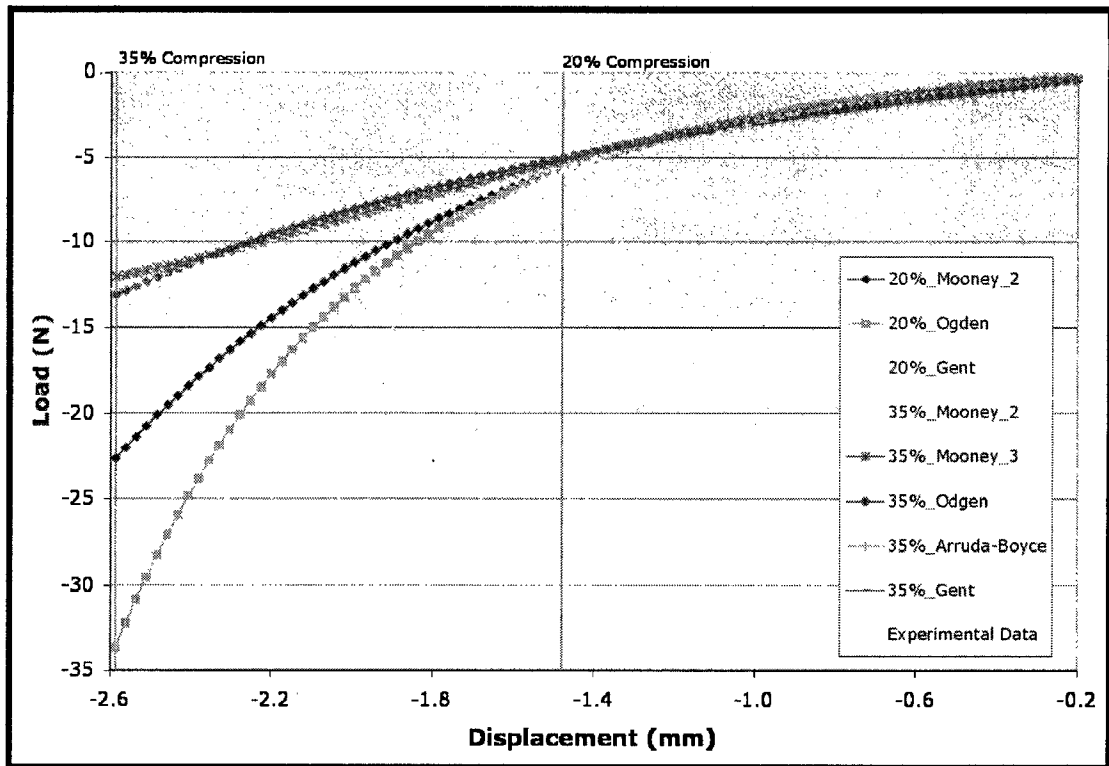


Figure 2.11. Results comparison for finite element analyses of test specimen.

Table 2.5. Percent error between material models and experimental data.

Material Model	Experiment Max Load (N)	Load Magnitude at 35% Compression (N)	Percent Error
Mooney (2)	12.86	12.1	6%
Mooney (3)		12.1	6%
Ogden		13.1	2%
Arruda-Boyce		13.2	3%
Gent		13.1	2%

#### 2.2.4. Fibroelastic tissue model

Similar mechanical testing was performed on right whale fibroelastic soft tissue (Campbell-Malone and Myers, 2006). When the methods described above were used to evaluate the fibroelastic soft tissue, the curve fits generated for the various material models were not as successful as those generated for the

epidermal tissue (figure 2.12). The Mooney-Rivlin, Arruda-Boyce, and Gent models resulted in curves that did not correspond well with the stress-strain curve created from the experimental test data. It has been found that the 2-term Mooney-Rivlin model was inadequate in describing the compression mode of deformation and fails to account for the stiffening of the material at large strains (MSC Software, 2005c). The 3-term Mooney-Rivlin model showed marginally better correlation. However, caution needs to be exercised on inclusion of higher order terms to fit the data, since this may result in unstable energy functions yielding non-physical results outside the range of the experimental data (MSC Software, 2005c). The Arruda-Boyce and Gent models simulate the non-Gaussian behavior of elastomer, however, for this application it was shown to be inadequate.

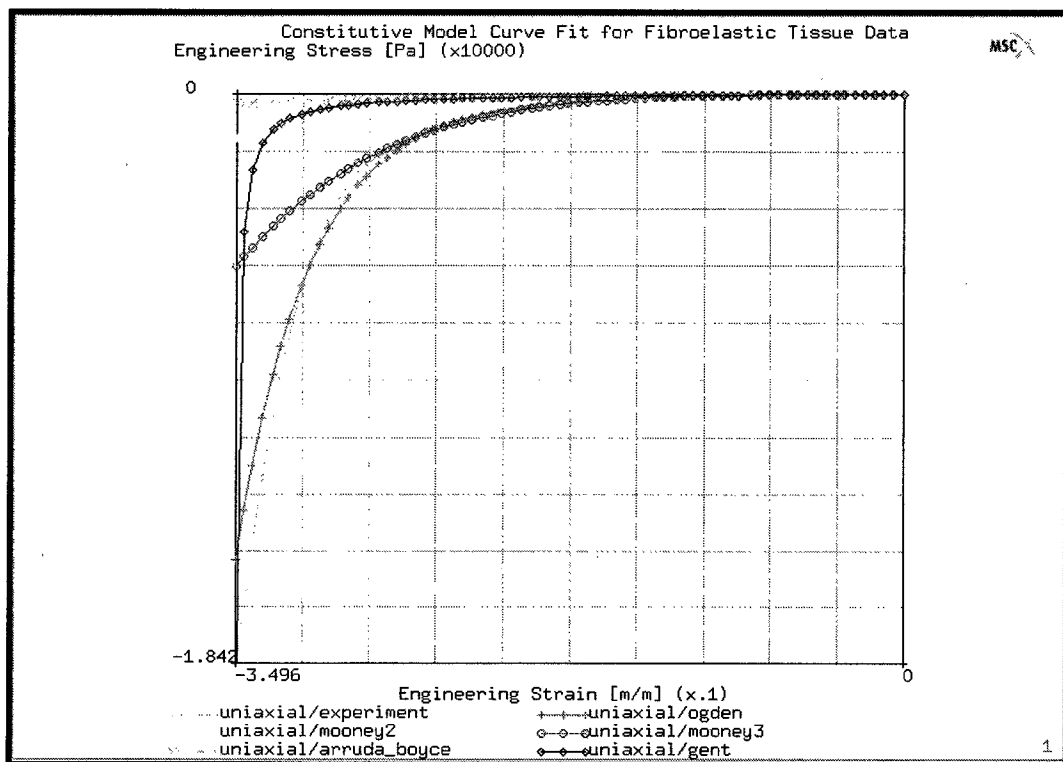


Figure 2.12. Constitutive model curve fit for fibroelastic tissue data.

The decision was made that one material model will be used to represent all the soft tissue in the whale. This assumes that all soft tissues exhibit the same mechanical response to impact. This simplification was required due to lack of information regarding material properties of each type of biological tissue involved, as well as the high level of complexity, which cannot be effectively modeled through numerical simulation. It was determined that the fibroelastic tissue will be used to represent all of the whale soft tissue. The Ogden model, which showed the best correlation with the test data, was selected as the material model to implement in the numerical simulation. The Ogden model has been shown to give good correlation with test data in simple tension up to 700% strain (MSC Software, 2005c). The model accommodates non-constant shear modulus and slightly compressible material behavior. The Ogden model is implemented by *MSC.Marc* using the following strain energy density function (see chapter 1.3 for details):

$$W = \sum_{n=1}^N \frac{\mu_n}{\alpha_n} J^{-\frac{\alpha_n}{3}} (\lambda_1^{\alpha_n} + \lambda_2^{\alpha_n} + \lambda_3^{\alpha_n} - 3) + 4.5K(J^{-1/3} - 1)^2 \quad (24)$$

where  $J$  is the Jacobian measuring dilatancy, defined as the determinant of deformation gradient. In the Ogden model,  $\mu_n$ ,  $\alpha_n$ , and  $K$  (Bulk modulus) were generated to achieve the best fit curve with the experimental data. Function (24) is expressed in terms of the element stretches in three principal directions, as defined by equation (25).

$$\lambda_i = \frac{L_i}{L_{0i}} \quad (25)$$

where  $L_i$  and  $L_{0i}$  are the initial and deformed lengths in direction  $i$ .

For the representative soft tissue material model, a 2-term Ogden model was used. The resulting material parameters, as determined by generating the curve fit of the experimental data in *MSC.Mentat*, are given in table 2.6 below.

**Table 2.6.** Material parameters for 2-term Ogden soft tissue model.

$\mu_1$	11.0877
$\alpha_1$	-2.94854
$\mu_2$	-8.36578
$\alpha_2$	-16.4271
<b>K (Bulk modulus)</b>	425,294 Pa
<b><math>\rho</math> (density)</b>	960.72 kg/m <sup>3</sup>

### **2.2.5. Equivalent linear elastic soft tissue model**

The Ogden soft tissue model described above resulted in convergence problems during the numerical simulation. The material behaved in such a manner that element deformations would become too large before the collision impact force overcame the inertia of the whale. This resulted in numerical instability of the finite element model due to excessive deformation and collapse of the finite elements, causing solution divergence.

This was likely caused by the lack of a full set test data to describe multi-axial states of deformation. To generate a robust material model, it is desired to have test data for uni-axial, bi-axial, simple shear, planar shear, and volumetric deformations. The data set obtained for both the epidermal and fibroelastic tissue consisted of only uni-axial compression. Without a full set of data, the true behavior of the material cannot be characterized.

To overcome this obstacle, the verification model representing the compression test specimen was revisited. Based on the lack of information

regarding the various states of deformation, the verification model was modified in a way that overcomes this lack of information.

During the collision event, the soft-tissue material will not expand laterally with respect to the direction of impact. This is due to the continuous mass of material surrounding the area of impact. The experimental data were obtained from testing performed on a cylindrical specimen, which was free to deform laterally as it was compressed. These lateral movements were not accounted for when generating the various constitutive material models, because no test data describing this movement was available. This situation was recreated in the finite element verification model by constraining the cylindrical surfaces against lateral expansion. In this way we ensure that only axial compression forces are considered. The simulation was run, implementing the Ogden material model, resulting in the Engineering Stress vs. Engineering Strain curve shown in figure 2.13.

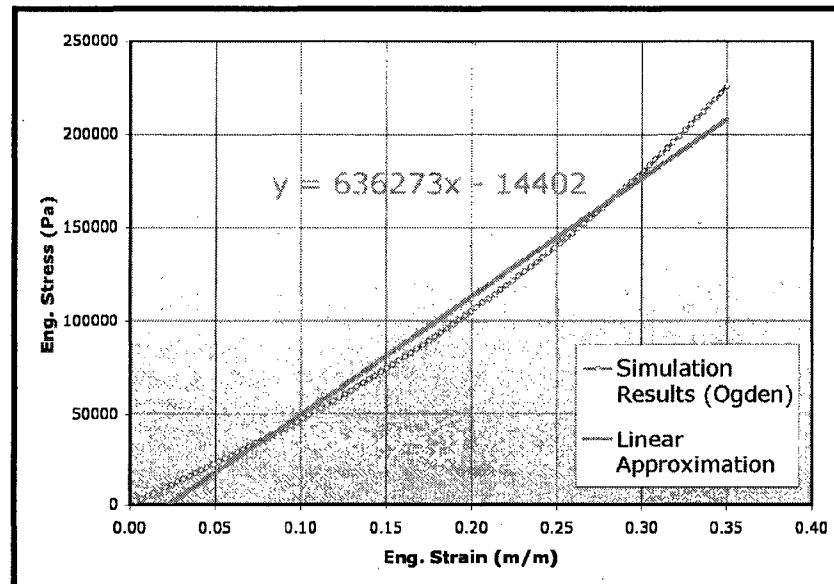


Figure 2.13. Stress-Strain curve for modified specimen finite element model with 2-term Ogden material model



This curve is fairly linear. Using the “trend line” feature in Microsoft Excel, a linear approximation was generated. The resulting slope of this curve, representing the Equivalent Linear Elastic Modulus, was 636,273 Pa. This value was implemented for the representative soft tissue material model in the numerical simulations.

### **2.3. Finite element mesh**

The finite element mesh was created in *MSC.Patran* due to certain mesh generation features that were not available in other pre-processors. *MSC.Patran* was able to mesh between two arbitrary surface shapes to result in a solid mesh containing a void space represented by the inner surface.

The surface model of the skeleton was meshed with 3-node triangular elements with an approximate size of 0.08m. From these surface elements, a solid mesh was generated using 3-dimensional 4-node tetrahedral elements. The resulting mesh contains 27,577 solid elements.

The surface model of the external whale geometry was first meshed with 3-node triangular surface elements. The element size chosen was 0.20m. Next, the same surface element mesh used for the skeleton was copied and superimposed within the external geometry mesh. By doing this, a solid mesh representing the soft tissue was created, leaving a void with the same shape and mesh pattern as the skeleton. The resulting solid mesh is composed of 201,505 3-dimensional, 4-node tetrahedral elements.

Once the appropriate material properties were defined for the bone and soft tissue solid meshes, the skeleton mesh was moved into position within the

soft tissue model. At this point, the coincident nodes at the boundary between the bone and soft tissue were merged to create the complete mesh with the appropriate material properties. Figure 2.14 shows the skeletal mesh within the soft tissue mesh. The soft tissue is shown in a longitudinal section to clearly depict the two separate meshes. The 3-node triangular surface elements were deleted once the solid elements were created. This mesh was then imported into *MSC.Mentat* for the remainder of the pre-processing and post-processing. *MSC.Marc* was used for solution.

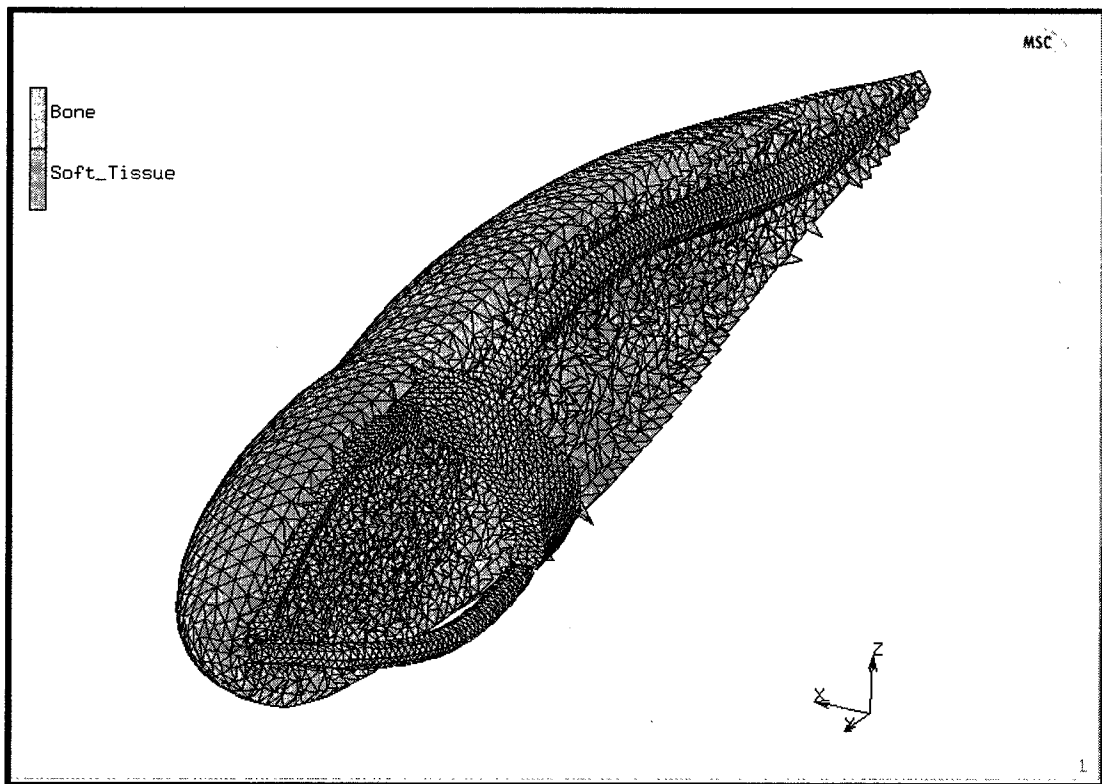


**Figure 2.14.** Finite element mesh section showing bone and soft tissue make-up.

Due to the number of simplifications required to generate a suitable skeletal model, the connection between the rostrum (cranium) and the spine was not included in the solid model. Given the nature of the impact loading

considered in these simulations, and the fact that the bones were supported by soft tissue only, the large lateral forces resulted in excessive relative motion between the rostrum and spine. To model the connection between the rostrum and spine, nodal ties (Rigid Body Elements, RBEs) were incorporated into the skeletal model. This type of element is used to connect the nodal translations and rotations of two or more nodes. In the simulations, twelve links were used to connect translation in the x-coordinate (in the global coordinate system) for nodes within the mesh for both the rostrum and the spine of the whale skeleton, as shown in figure 2.15. This succeeded maintaining the relative position of the bones throughout the duration of the collision.

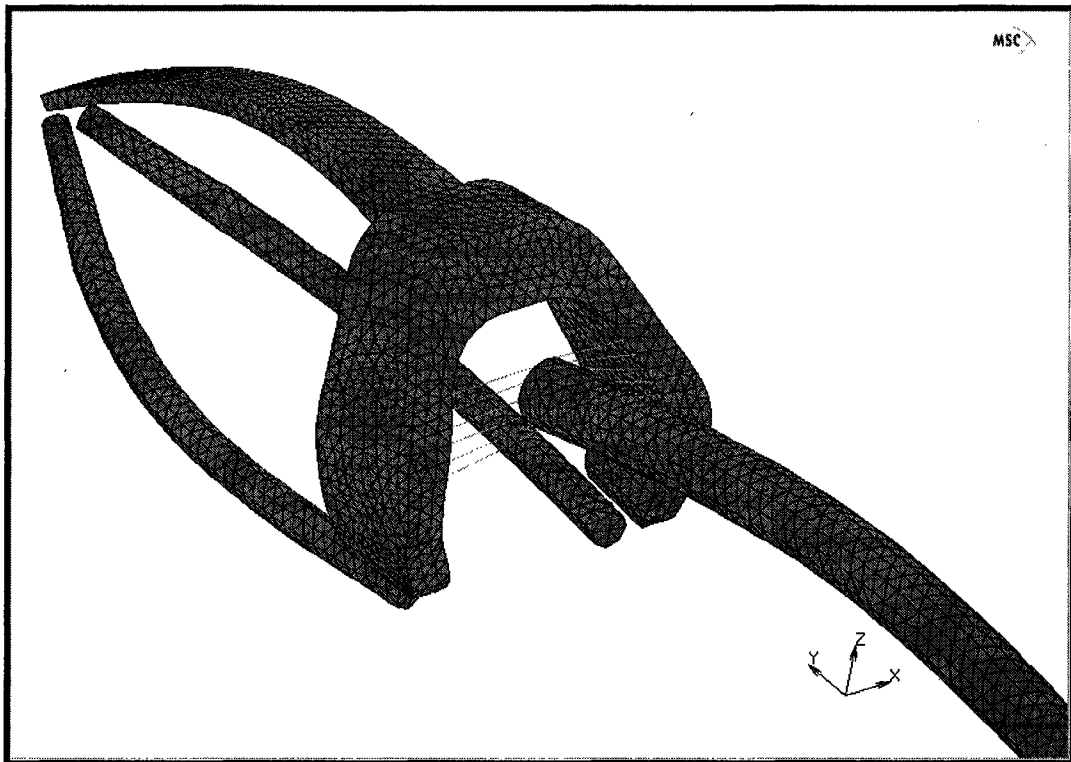


**Figure 2.15.** Rigid links connecting rostrum and spine.

Table 2.8 summarizes the properties of both the bone and soft tissue elements making up the whale model finite element mesh.

Table 2.7. Summary of finite element mesh properties.

	# of Elem.	Class	Type	Geometry
Bone	27,577	Tetra4	Full Integration (134)	3-D Solid
Soft Tissue	201,505	Tetra4	Herrmann-Full Integration (157)	3-D Solid w/Constant Dilatation
Links	12	-	-	1-D Bar

The overall mass of the whale resulting from the material properties applied to the bone and soft tissue elements was checked. This was done in *MSC.Mentat* by using the element mass command under the utility menu. The whale mass is 46,630 kg. Based on the work in (Moore et al., 2005), the expected range of weight for a whale of 13.6 meters in length is between 30,000 kg and 55,000 kg. This is detailed in figure 2.16, shown below. Since the weight of the numerical whale model was within this range, no special consideration was needed to ensure that the model was in the correct weight range. Weight was of concern since the inertia of the whale was assumed to have the greatest effect on the dynamics of the collision.

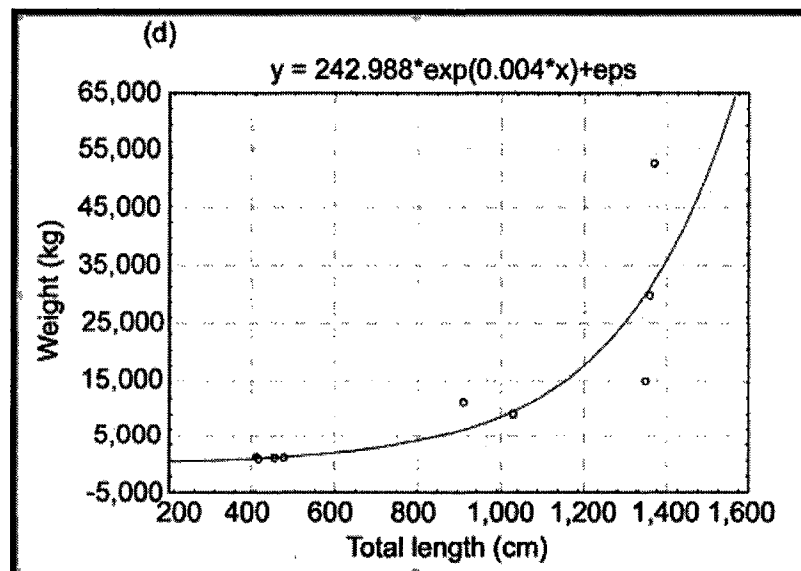


Figure 2.16. Right whale length to weight relationship. Figure 1.d from (Moore et al., 2005).

## CHAPTER 3

### DEVELOPMENT OF SHIP MODEL

#### **3.1. Selection of hull geometry**

There are a great number of vessel shapes and sizes in the oceans today. The representative shape chosen for analysis was that of the very large crude carrier (VLCC). The size of this vessel is an obvious concern with regards to interaction with a right whale, which is much smaller. Add to this the mass, lack of maneuverability, and traveling speeds, and the danger for a whale in its path increases significantly. Figure 3.1 shows an example of the type of ship that is of concern for collisions with right whales. Ships of this type can measure 58 meters (190 feet) wide by 300 meters (984 feet) long.

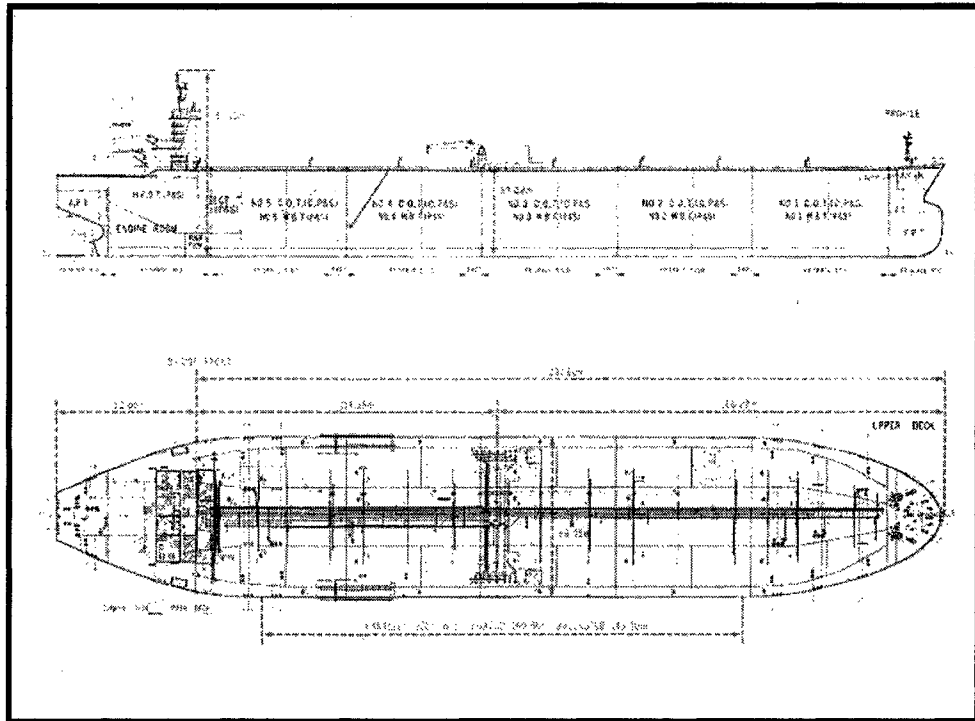
This study focused on a single hull geometry as a representative model. However, once a working simulation is completed, modification to analyze various hull shapes and designs is relatively easy. One reason for this is that *MSC.Marc* allows the definition of rigid contact bodies from geometric surfaces, precluding the need to define a finite element mesh for the hull geometry. Therefore, any hull geometry could be imported into the model and quickly set up to run a new simulation.



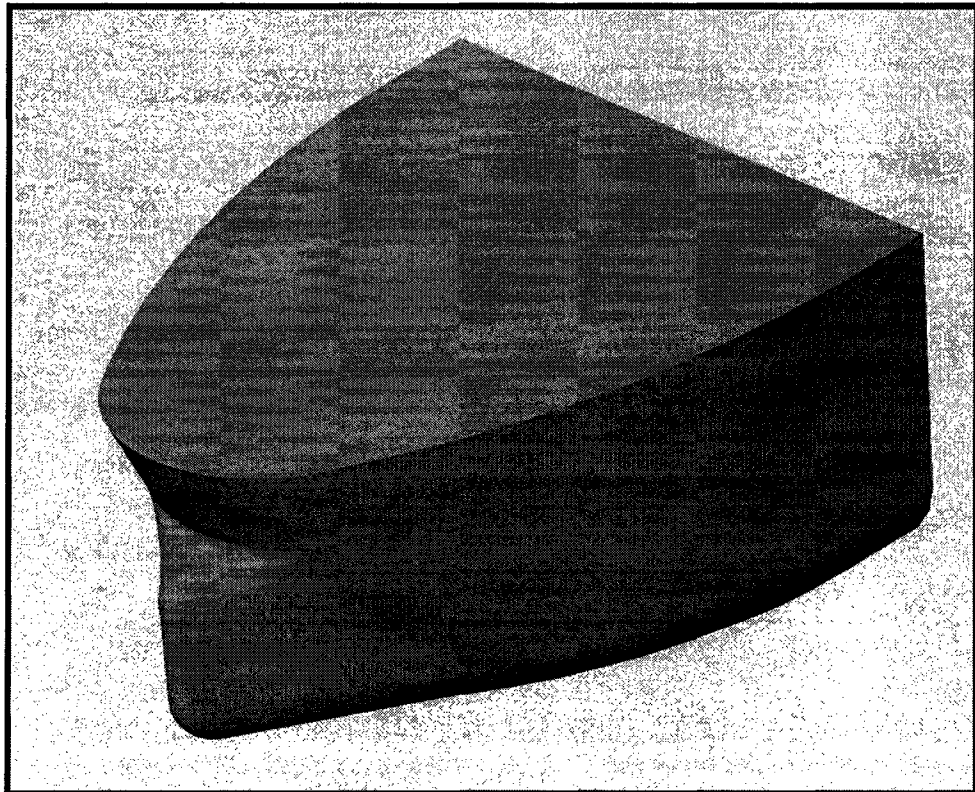
**Figure 3.1.** Typical Very Large Crude Carrier (VLCC) (Photo by Frontline).

Figure 3.2 is the schematic used to help create the model for generation in the solid modeling software SolidWorks®. This figure gives key dimensions for the VLCC. The remaining dimensions were obtained by scaling. Figure 3.3 is the final solid model that was imported into the finite element analysis software pre-processor. The solid model consists of about a quarter of the total ship length, and models the bulbous bow.

Payload of a vessel has an effect on the hull geometry involved in the collision. A heavily laden ship has a greater draft, meaning that a larger portion of the hull is submerged. In the case of a bulbous bow, such as the VLCC selected for this simulation, the depth of draft greatly affects the portion of the hull that may impact the whale. The collision forces are influenced by the relative position of the whale with respect to the approaching vessel.



**Figure 3.2.** Schematic of VLCC used to generate hull model (drawing by Frontline).



**Figure 3.3.** Hull model generated for use in numerical simulations.

For a vessel carrying a large load, the bulbous bow may be below the surface of the water. In this scenario, it might be possible for the whale to get "hung up" on the upper portion of the bulbous bow. This seems to be depicted in figure 3.4. This scenario would be disastrous for a whale that was not killed on impact. However, the objective of this study was determining the impact forces that result in fracture of bone. The hydrodynamic forces involved in "trapping" the whale against the bow were significantly less than those resulting from initial impact. For this reason, the effect of the whale being carried along after the collision was not considered in this study.



**Figure 3.4.** Photo depicting a whale "hung up" on the bulbous bow of a vessel.



## CHAPTER 4

### NUMERICAL SIMULATION OF COLLISION

Numerical simulation of collision, in addition to development of FEA models of the whale and ship, involved:

- Assignment of the required initial and boundary conditions.
- Definition of possible contact areas.
- Choosing the appropriate parameters of the numerical procedure.

These factors are discussed in the following sections. We define the load cases considered in the numerical simulations of ship-whale collision and discuss the challenges associated with proper modeling of the hydrodynamics of ship approach and collision event.

#### **4.1. Parameters of numerical time integration**

The numerical simulation was set up as a dynamic transient analysis. The dynamic analysis in time captures the effects of inertia in the overall behavior during the collision event. Without this, the contributions due to ship and whale mass would not be accounted for. Three iterative solution procedures are available within *MSC.Marc's* solution control menu. These are the Full Newton-Raphson, Modified Newton-Raphson, and Newton-Raphson with strain correction. For this work, the default Full Newton Raphson procedure was used. *MSC.Marc* offers three implicit time integration schemes: The Single Step

Houbolt, Newmark-beta, and Modal Superposition. Refer to chapter 1.5 for details of the numerical procedures. For this analysis, the Newmark-beta method was used. *MSC.Marc*'s default beta ( $\beta$ ) and gamma ( $\gamma$ ) constants were used. These constants are 1/4 and 1/2, respectively. This is proposed to be an unconditionally stable scheme, referred to as the constant-average-acceleration method, or the trapezoid rule (Bathe, 1996). A large strain nonlinear analysis procedure was used. For the load cases with 10 and 15-knot vessel approach speeds, the duration of the simulation was set to 0.4 sec, divided into 1000 time steps. This resulted in a time step of 0.0004 seconds. For the load case with an initial ship speed of 5 knots, the simulation duration was increased to 0.8 seconds, resulting in a 0.0008 second time step. This was to compensate for the slower approach speed relative to the first two cases. Through trial and error, these time steps were determined to be sufficiently small to allow for adequate solution convergence with long enough durations to capture the desired information from the collision event.

#### **4.2. Initial conditions**

Four different initial conditions (load cases) were considered in the numerical simulations. The initial conditions were such that the ship approached at a prescribed velocity and the whale was at rest. The initial velocity was set up within the contact parameters in *MSC.Mentat*, as described below.

The first three load cases represented a direct impact on a static whale, as depicted in figures 4.1 and 4.2. This was assumed to be the worst-case scenario for mandible fracture as the fatal endpoint. This assumption was validated by the

findings of post-mortem data on a number of right whales (Campbell-Malone, 2007). The forth load case considered the vessel to have a greater draft, meaning that the hull was deeper in the water as shown in figure 4.3. In this case, the so-called “indirect” collision occurs, as described in chapter 3.1. This introduces a new impact area and a host of different loading conditions when compared with the direct impact scenario. However, this scenario did not present the worst case for mandible fracture.

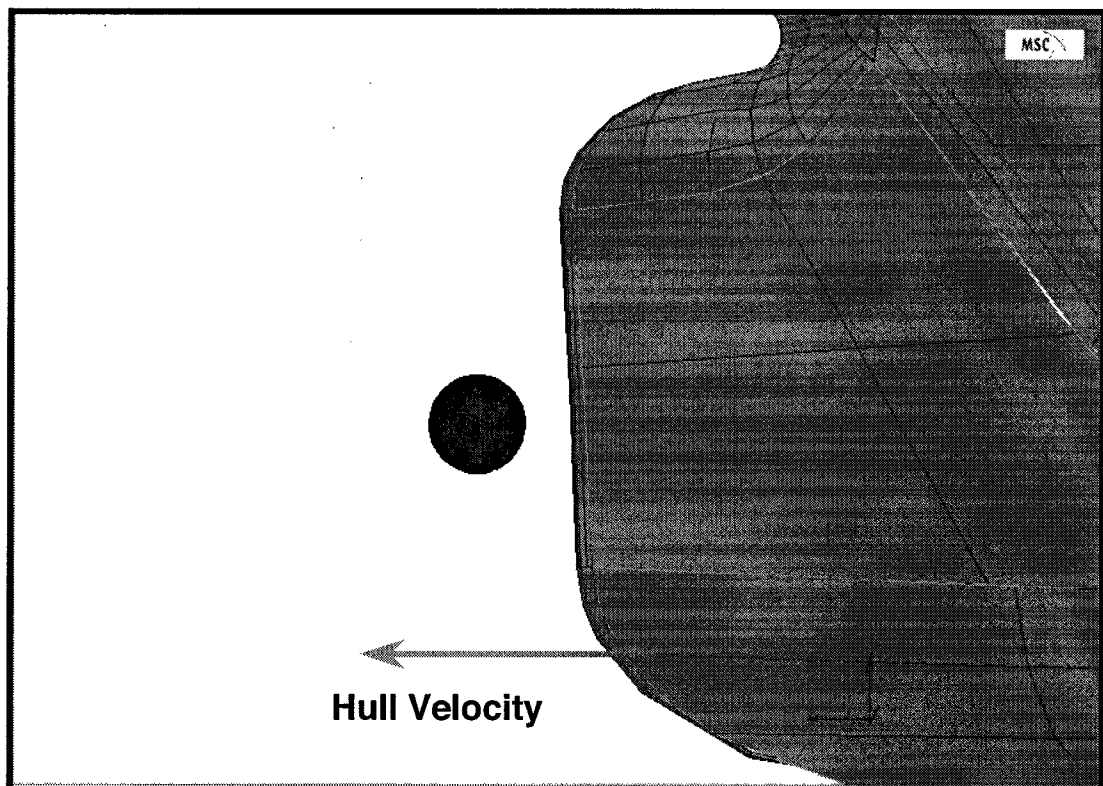


**Figure 4.1.** Direct impact scenario, viewed from side.

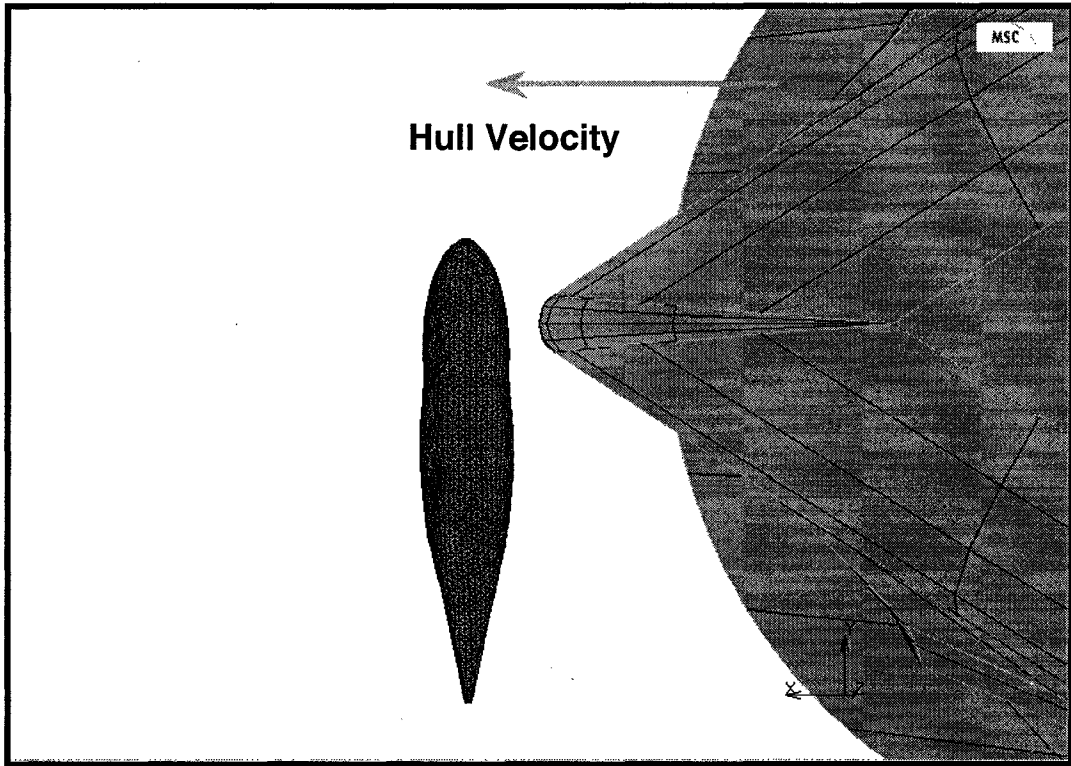


Figure 4.2. Direct impact scenario, viewed from beneath.

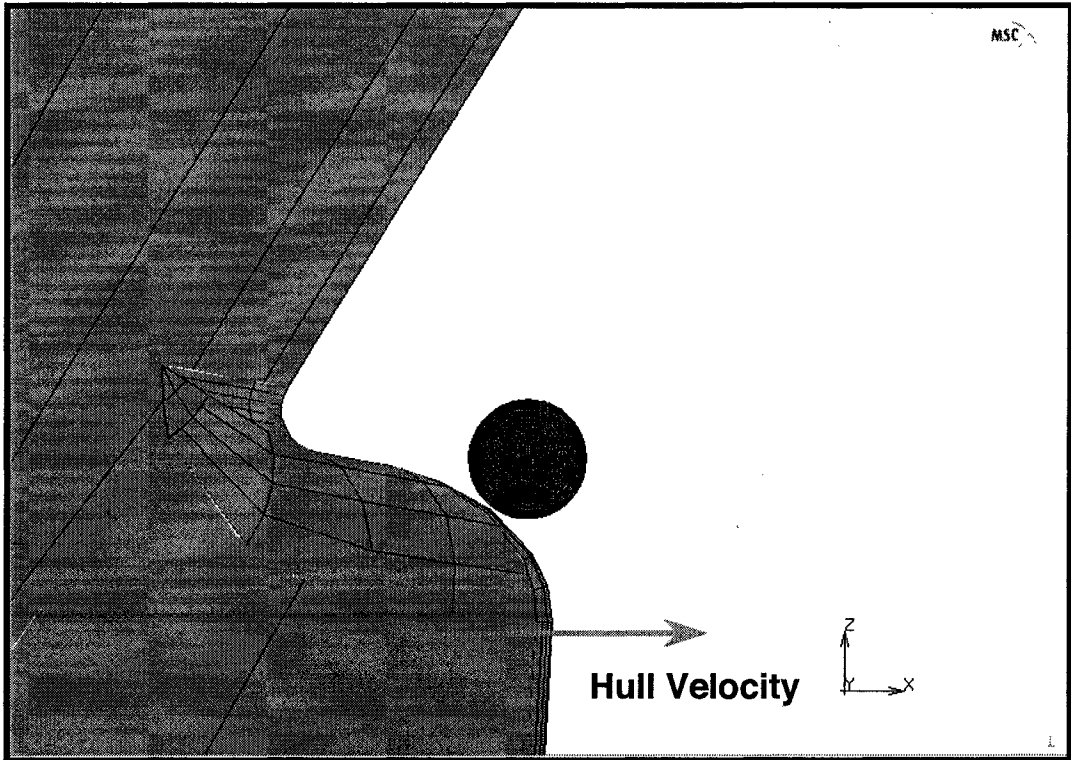


Figure 4.3. Indirect Impact scenario with hull having greater draft.

#### **4.2.1. 15-knot direct impact load case**

The first load case considered was that of a direct impact with a vessel speed of 15 knots. Direct impact refers to the situation where the whale is positioned perpendicular to the movement of the approaching ship. The relative positions were set up so that impact occurs directly at the mandible bone. 15 knots is an estimated average speed for vessels within right whale critical habitats.

#### **4.2.2. 10-knot direct impact load case**

The second load case considered a direct impact with a vessel speed of 10 knots. NOAA Fisheries Service (NMFS) is presently proposing a rule to limit vessel speed to 10 knots or less in specified locations. The results from this load case can be compared to the 15-knot load case to quantify how effective speed reduction is at reducing the risk of mortality.

#### **4.2.3. 5-knot direct impact load case**

The third load case considered a direct impact with a vessel speed of 5 knots. Relative positions were the same as the previous cases. The results of this load case can be combined with the first two load cases to generate a curve representing impact force as a function of vessel speed.

#### **4.2.4. 15-knot indirect impact with greater hull draft**

The fourth load case considered a vessel with greater draft, resulting in the situation where the top of the bulbous bow impacts lower on the whale and moves beneath the whale. This resulted in forces on the whale that were different from the direct impact load cases. This did not result in the worst-case with

regards to mandible fracture. However, it highlights effects of omitting gravity forces, buoyancy, and drag characteristics.

### **4.3. Contact and boundary conditions**

The hull contact surface was specified as a rigid contact body. The “Body Control” parameter in *MSC.Mentat* was set to give the hull the desired initial velocity, in meters per second in the x coordinate, for the load case being considered. The “Boundary Description” was set to “analytical”. When selecting contact surfaces, care was taken to choose the minimal number of areas or elements. This helps to cut down on analysis time. For this reason, two different hull contact segments were employed depending on where contact was expected for the load case being considered. For direct impact, the contact area shown in figure 4.4 is used. For indirect impact, the contact area in figure 4.5 is used.

The whale contact was specified as a deformable contact body. The contact area was defined by selecting elements only in the area where contact was expected. By keeping the number of elements to a minimum, model solution time was reduced. The deformable contact area contains 10840 elements and was given a “discrete” boundary description. This contact area is shown in figure 4.6. No friction was defined between the contact surfaces. It was determined that friction does not play a significant role in the collision event.

The contact table in *MSC.Mentat* was set up to define which contact segments interact together. In this case, there were only two contact segments defined for a given load case, and they are expected to interact. Self-contact was

not expected for either contact segment, so the contact table was not set up to consider for this.

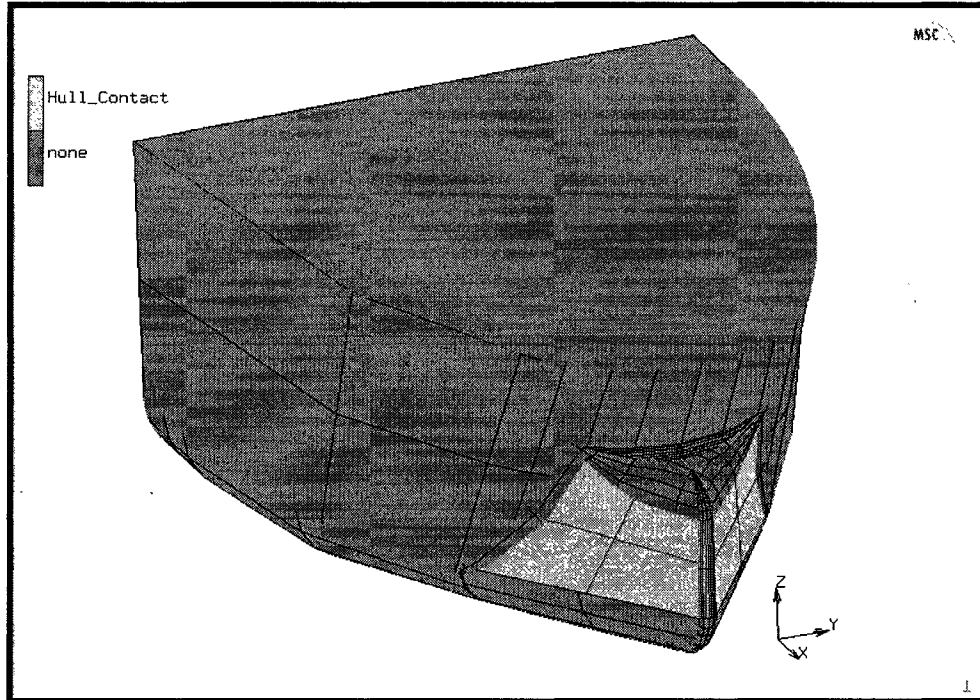


**Figure 4.4.** Contact area applied to rigid hull surface for direct impact collision.

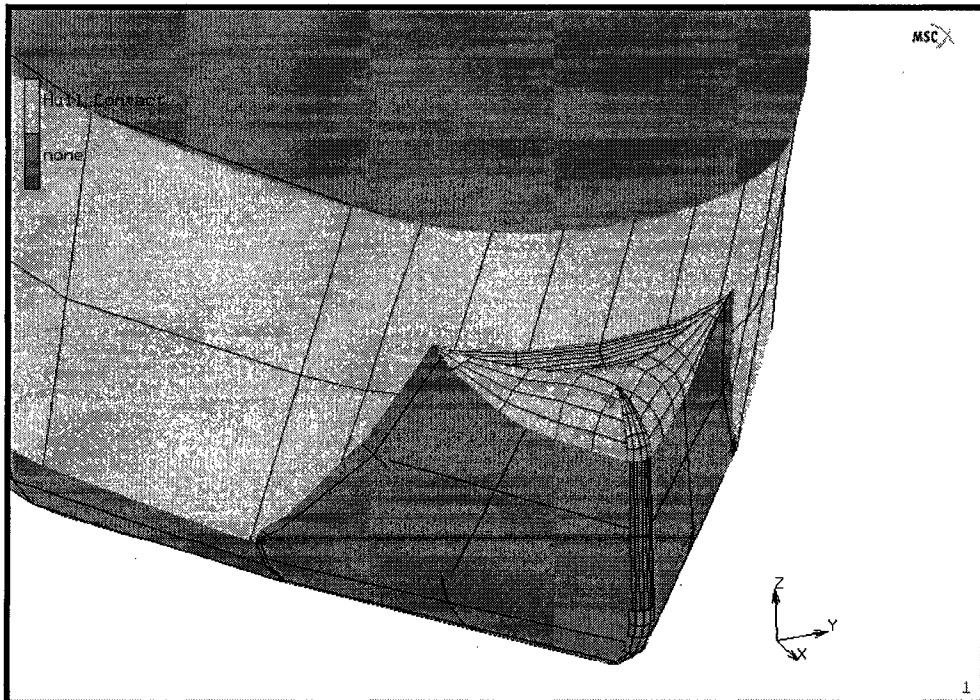


**Figure 4.5.** Contact area applied to rigid hull surface for indirect impact collision.

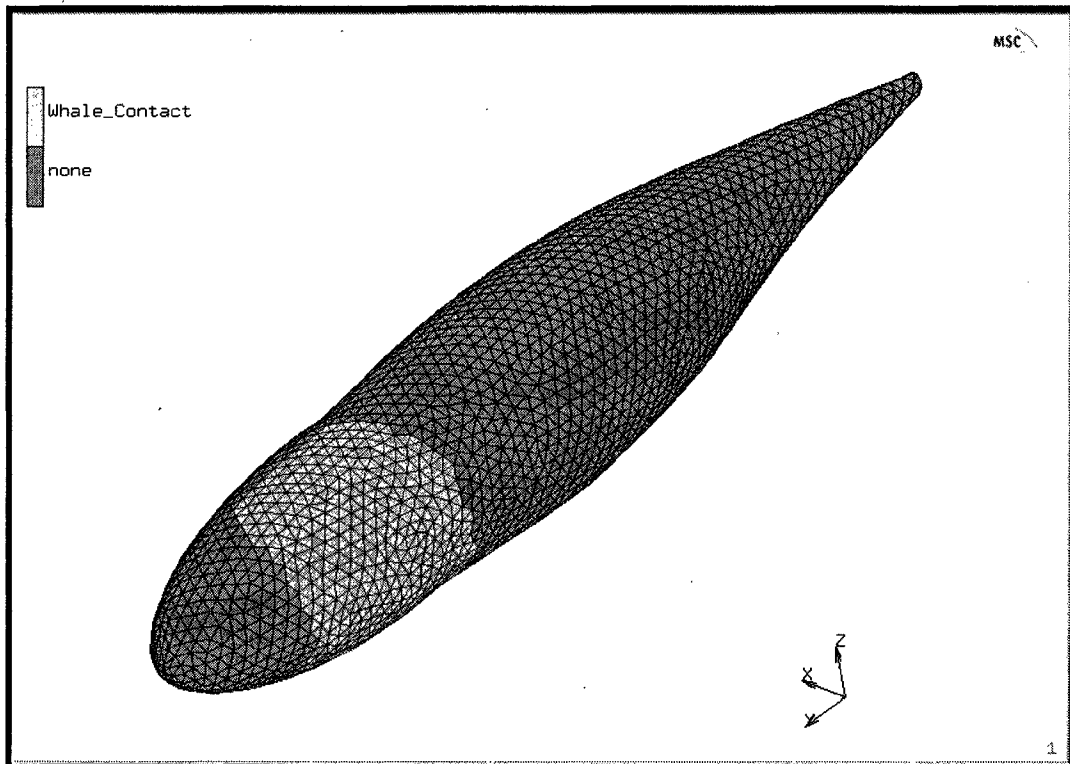


**Figure 4.6.** Contact area applied to whale finite element mesh.

#### **4.4. Hydrodynamics of ship approach**

It has been shown that the hydrodynamics of a large ship moving through the water can have an effect on the characteristics of a ship strike. Depending on relative locations of the ship and whale, bow waves can move the whale just prior to impact. This has the effect of giving a static whale some initial motion, or changing the velocity or orientation of an approached whale. This could possibly be beneficial to the whale, as any amount of initial velocity of the whale reduces the relative velocity of the two at impact. For example, if a ship approaches at 15 knots and the whale is initially static, the relative velocity is 15 knots. However, if the bow wave imposes an initial velocity of 3 knots on the whale just before impact, the relative velocity is now 12 knots.

These hydrodynamic effects make it difficult to assess the true initial



conditions just prior to a collision. For this work, no hydrodynamic effects were considered. Since the static whale is a more dangerous scenario with respect to relative velocities, as described above, this case was used.

In accordance with the findings of (Knowlton, et al. 1998) there are a number of scenarios caused by hydrodynamic effects. These scenarios, such as the whale being pulled into the side of the ship, were not considered in this study. The most elusive variable is how the whale responds to an approaching vessel. Knowlton, et al. (1998) modeled a number of different assumptions of whale reactions and found that this does make a difference with respect to whether or not a collision might occur. There are also a number of studies dealing with the acoustics affecting the ability of the whale to detect an approaching vessel. Theories predict that phenomena such as Lloyd's mirror effect, shadowing, and spherical spreading make it difficult to discern the sound of an approaching ship from ambient surface noise (Blue, et al. 2001). It is also hypothesized that slower ship speeds are more dangerous to whales. This idea is based on the fact that acoustic signature is proportional to propeller tip rotation. Therefore, a slower moving ship, which means a slower propeller rotation, registers a weaker signature. These weaker signatures may be drowned out by the ambient surface noise.

Though these variables could all have a degree of effect on the occurrence and characteristics of a ship strike, they were not considered in the numerical simulations conducted in this study.

## CHAPTER 5

### RESULTS OF SIMULATIONS

The goal of this research was to produce data on overall dynamics of vessel collisions with right whales, forces involved, and loading on the right whale mandible bone for various collision scenarios. By running a number of load cases with varying collision parameters, the dependence of the impact forces on different conditions can be established. This will aid in determining what steps can be taken to reduce whale mortality.

Numerical simulation for various vessel approach velocities has been performed. In this chapter, the results for three direct impact collision scenarios, at velocities of 15, 10, and 5 knots, are discussed in detail. Also, the results for an indirect impact with a greater hull draft are presented, and the modeling challenges for that simulation are discussed. The results of the simulations include:

- Visual presentation of the collision event progression in time.
- Analysis of the overall deformation and stresses in the skeleton during impact.
- Contact forces as a function of time.

- Evaluation of data needed for detailed analysis of the deformation and fracture of right whale mandible during collision. The data processing procedure for this analysis is provided below.

### **5.1. Data processing procedure to find surface loading on mandible**

One of the goals of the numerical collision simulations presented in this thesis was to provide input data for the detailed finite element analysis of the right whale mandible bone. It was determined by (Campbell-Malone, 2007) that mandible fracture is a viable fatal endpoint for many observed blunt traumas resulting from ship collision. To model fracture of the mandible during collision, the stresses acting on the bone and the area of their application must be determined. The final step was to process the numerical simulation results into a form that can be applied to the detailed FEA model of the mandible bone.

#### **5.1.1. Determining the area of impact**

For the purpose of applying load to the detailed finite element model of the whale mandible bone, a representative area for application of impact force needed to be determined. Due to the dynamic nature of the collision event, the stress in the bone varies with time. The goal here was to define a constant area to which a single average pressure can be applied and to determine this pressure for each time step of the collision event. Since the impact of the ship results in compressive load, the minimum value of principal Cauchy (true) stress was considered for determining the pressure acting on the mandible.

The impact area was determined using the time increment at which the maximum impact force occurred. This was done utilizing the post-processing

capabilities of *MSC.Mentat*. A time history curve of contact surface force was plotted and the appropriate increment was selected. For this increment, the highest minimum principal Cauchy stress was located and its magnitude determined. With this information, the contour bands for the stress plot were manually adjusted to show a range from zero to the peak stress, with ten contour levels. With the contour bands set this way, it was easy to evaluate the distribution of stress in terms of percent of peak stress, shown in ten percent increments. The impact area was chosen as the portion of the bone surface with stress ranging from 60% to 100% of the peak minimum principal Cauchy stress. This area is shown in figure 5.1 for the 15-knot load case.

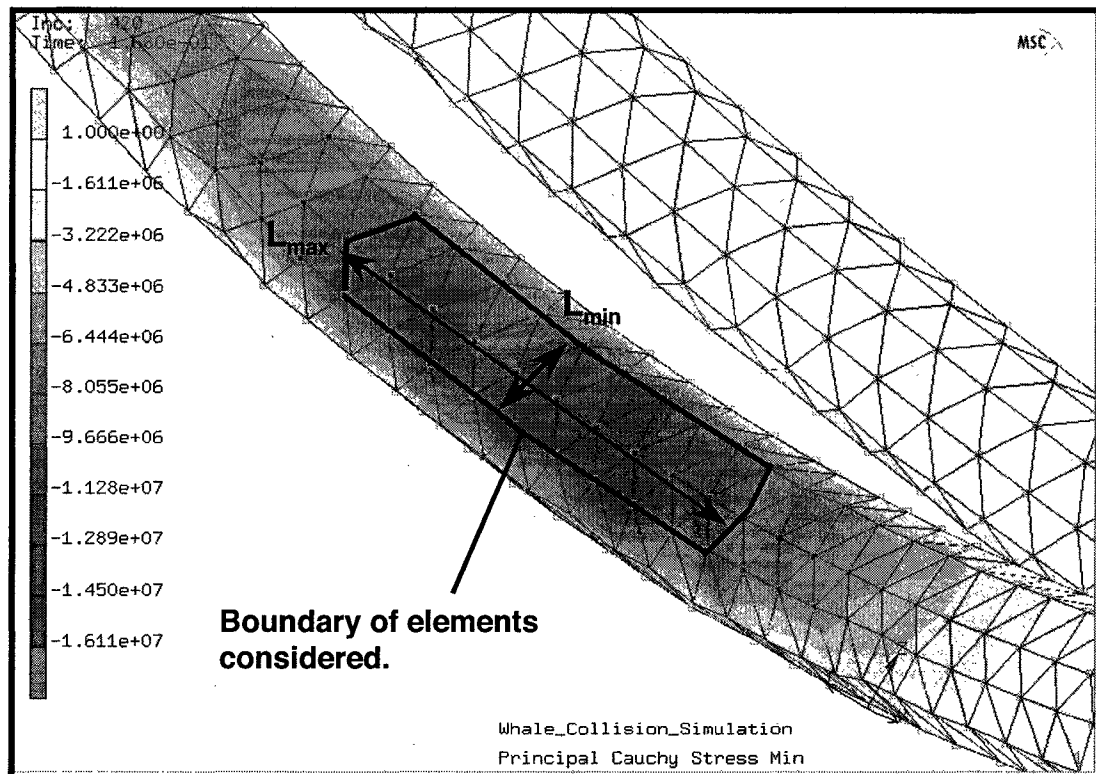


**Figure 5.1.** Determination of mandible impact area – 15 knot load case.

As can be seen in this figure, the area of interest was not necessarily simply defined. The stress contour was very inconsistent. Due to the coarse mesh, the stresses do not form a smooth contour. A regular shape that may have portions with predicted stresses below 60% peak, and does not capture all stresses above 60% of peak approximates the impact area. However, this approximation was within the accuracy of the finite element model used for simulation of collision. The prediction for the mandible's area of impact and the peak stresses for the three direct impact load cases considered are summarized in table 5.1.

**Table 5.1.** Post-processing summary for determination of average impact loads.

Load Case	Time [sec]	Peak Stress [Pa]	Axes [m]		Impact Area [m <sup>2</sup> ]
			L <sub>maj</sub>	L <sub>min</sub>	
15 knot	0.140	-1.167e7	0.7377	0.15	9.15e-2
10 knot	0.164	-0.789e7	0.8314	0.15	1.06e-1
5 knot	0.216	-0.348e7	0.7783	0.15	9.11e-2

Due the coarse discretization in the tangential direction of the bone, the stress distribution in this direction was difficult to estimate. The width of two elements was used for all three load cases. The approach to defining the mandible impact area was based on the peak stresses observed for a given load case. Since the area was defined relative to the peak stress, it was expected that the impact area was similar for each case, though the peak stresses were greater for the higher speed collisions.

The impact area on the detailed mandible model is shown in figure 5.2. This area was chosen using the major and minor axes from the whale skeletal model shown in figure 5.1. Care was taken to locate the impact area in a similar position on the bone as results from the dynamic simulation. The area of the

contact surface shown in figure 5.2 was verified using the face area command in the utilities menu of *MSC.Mentat*. The resulting area was  $0.09234\text{m}^2$ . This was sufficiently close to the estimated values listed in table 5.1.

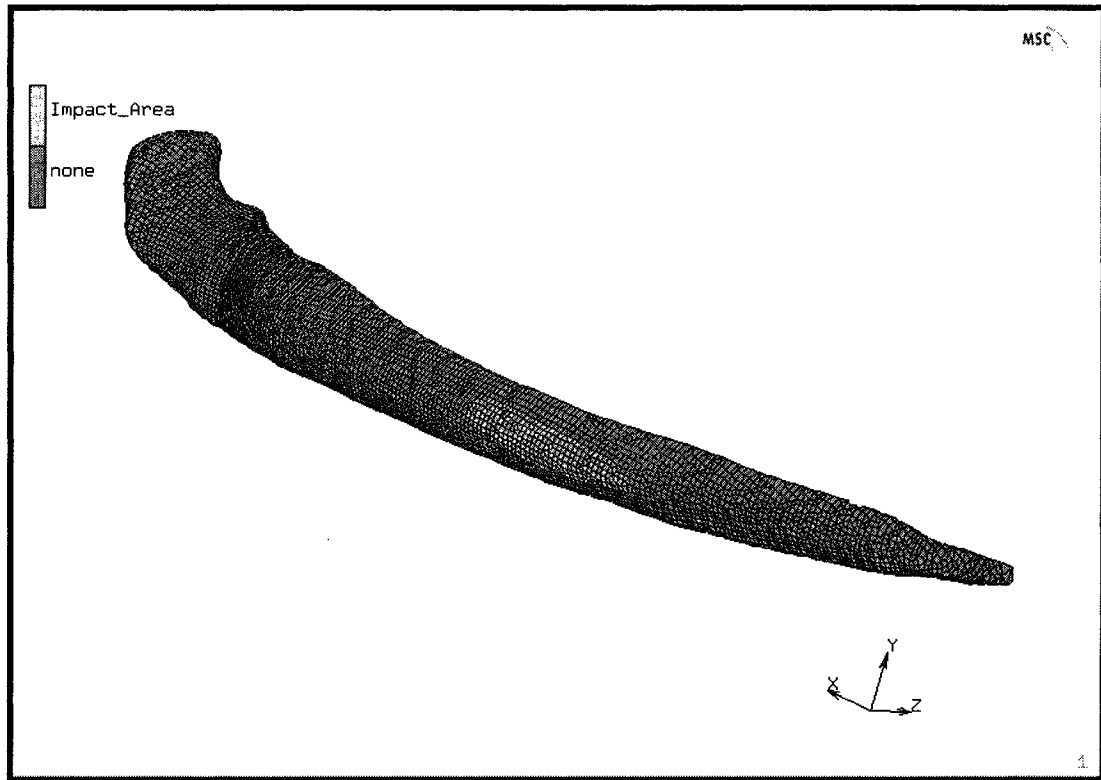


**Figure 5.2.** Detailed mandible model with impact area shown (Tsukrov et al., 2006).

### **5.1.2. Average impact stress**

For each node within the area of impact defined above, a time-history curve for Minimum Principal Cauchy Stress was generated using *MSC.Mentat*. This results in a graph of stress versus time for all the nodes of interest. The data forming this graph was then exported from *MSC.Mentat* and written to a text file. This file was imported into *Microsoft Excel*® as space-delimited data. The data was then processed to find the average value of stress for all the nodal contributions at each time step. This average stress applied over the impact area

defined above was used as input data for the detailed mandible model. The process was completed for the 15-knot, 10-knot, and 5-knot direct impact scenarios. Variation of the average impact stress with time obtained from these simulations is presented in figure 5.3.

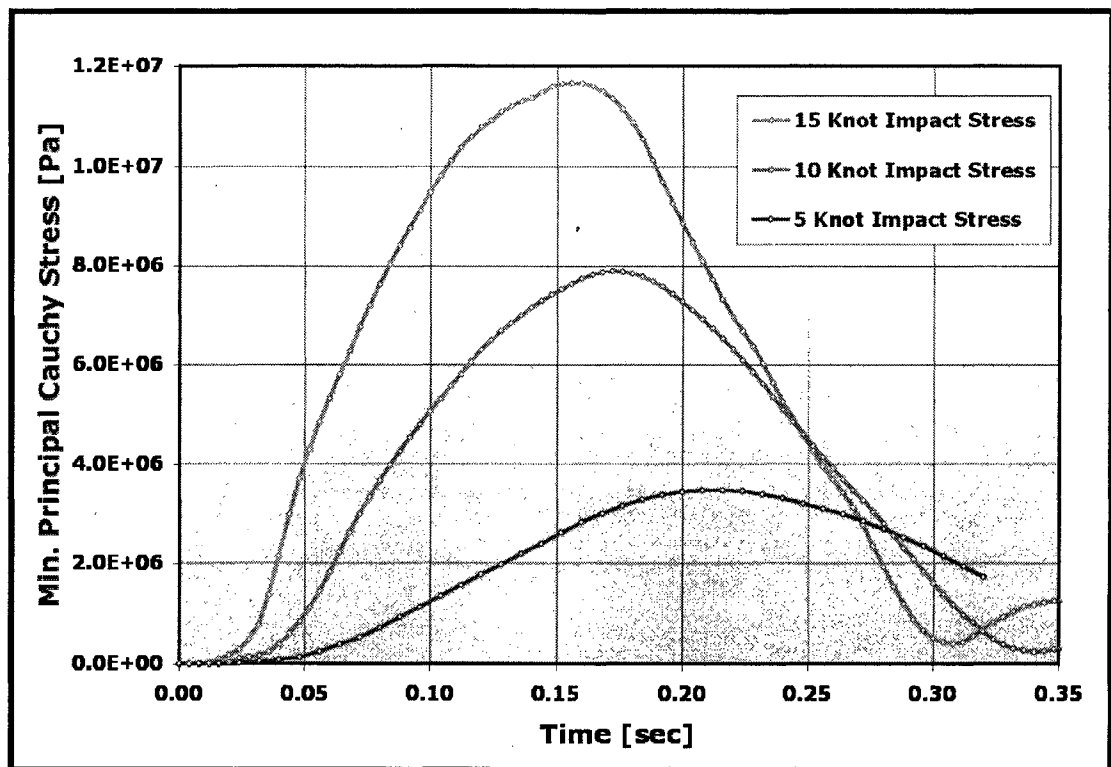


Figure 5.3. Average impact stress on contact area of interest.

The data used to plot the curves in figure 5.3 can be imported into *MSC.Mentat* to generate load tables. Thus the transient load can be applied directly to a specified area on the detailed mandible model.

## **5.2. Summary of results**

The following is a summary of the results for the considered load cases. First, each load case is discussed separately. Then the three direct impact load cases were compared to quantify the effects of varying velocities on the impact

forces imparted on the whale. The indirect load case is evaluated separately for discussion of the effects of drag, buoyancy, and gravity.

#### **5.2.1. 15-knot direct impact collision results**

The first scenario considered was that of a vessel traveling at 15 knots, approaching perpendicular to a static whale. This was assumed to be the worst-case scenario for mandible fracture as the fatal end point. The relative positions are such that impact occurs directly at the location of the mandible bone.

Figure 5.4 shows a progression of displacement throughout the duration of the analysis. Maximum force in the mandible bone occurs at a time of 0.140 seconds from the beginning of the collision. This instance is shown in more detail in figure 5.5.



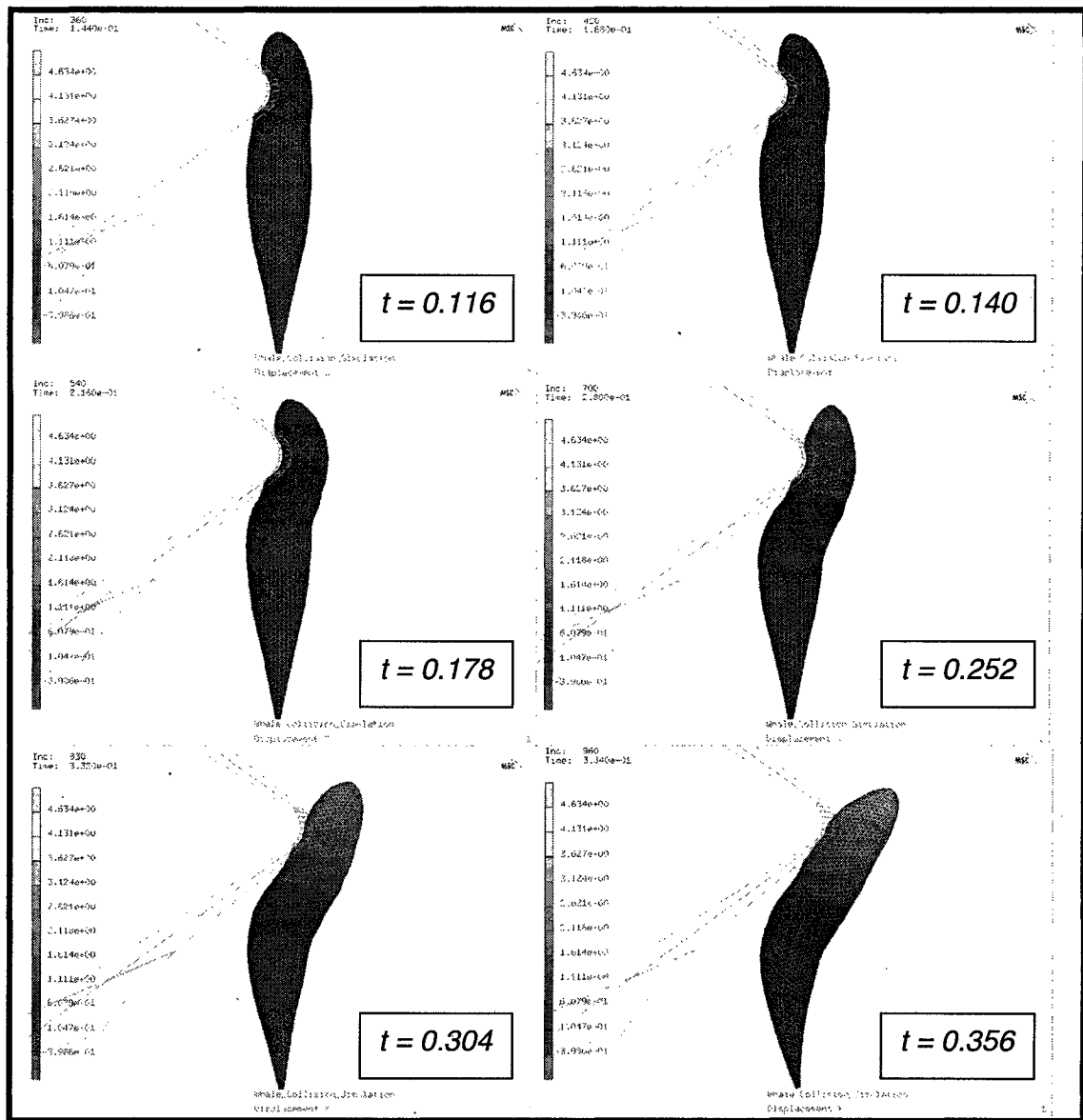
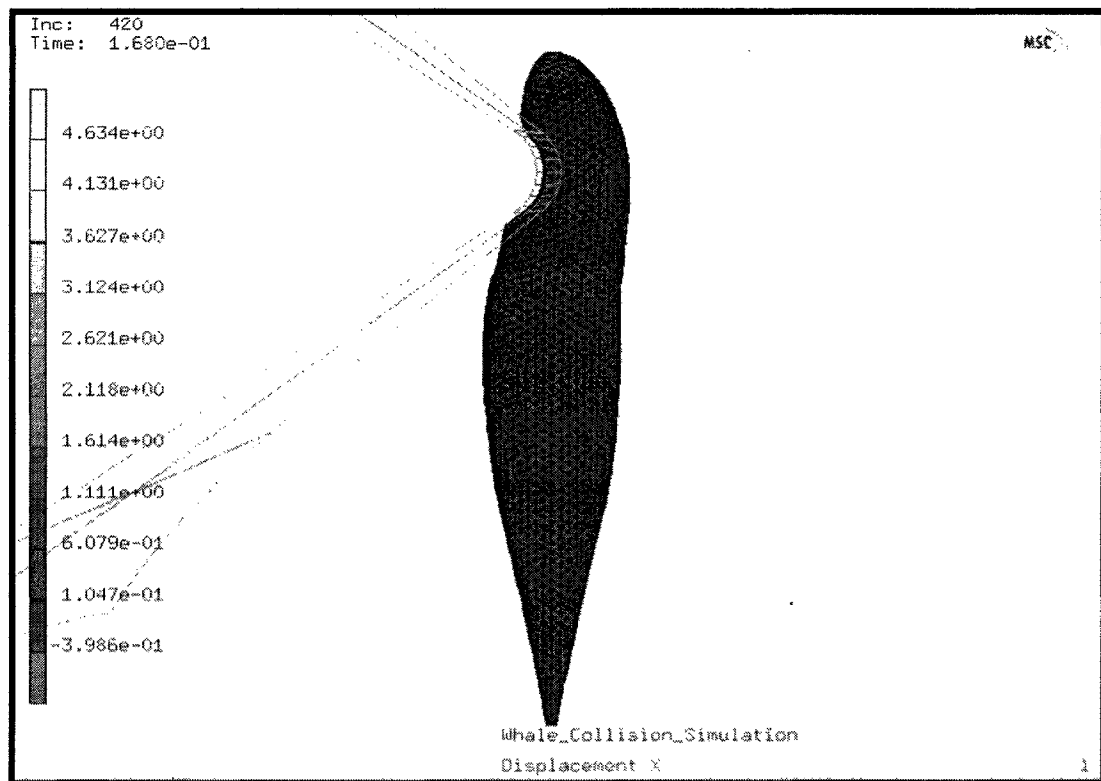


Figure 5.4. 15-knot direct impact collision progression, full whale model.



**Figure 5.5.** 15-knot direct impact, full whale, maximum stress at  $t=0.140$  sec.

The first thing to note is how much the hull penetrates into the whale before the inertia is overcome and the whale begins to move as a whole body. This highlights the issue that results in numerical instability when the hyperelastic soft tissue model was implemented. With the Ogden model parameters determined from unconstrained compression experiment, the tissue was too soft so that the penetration continues until nodal deflection results in collapsed elements before the whale mass was overcome, causing solution divergence.

Figure 5.5 shows that the head began to move before maximum load was developed in the mandible. This motion was minimal, being localized to the area directly opposite of impact, and will not generate any significant drag force. This

validates the assumption that drag force can be omitted from the simulation without affecting the results.

Figures 5.6 and 5.7 show the response of the skeleton to the 15-knot direct impact. The figures show the extent of deflection in the mandible bone during the collision event.

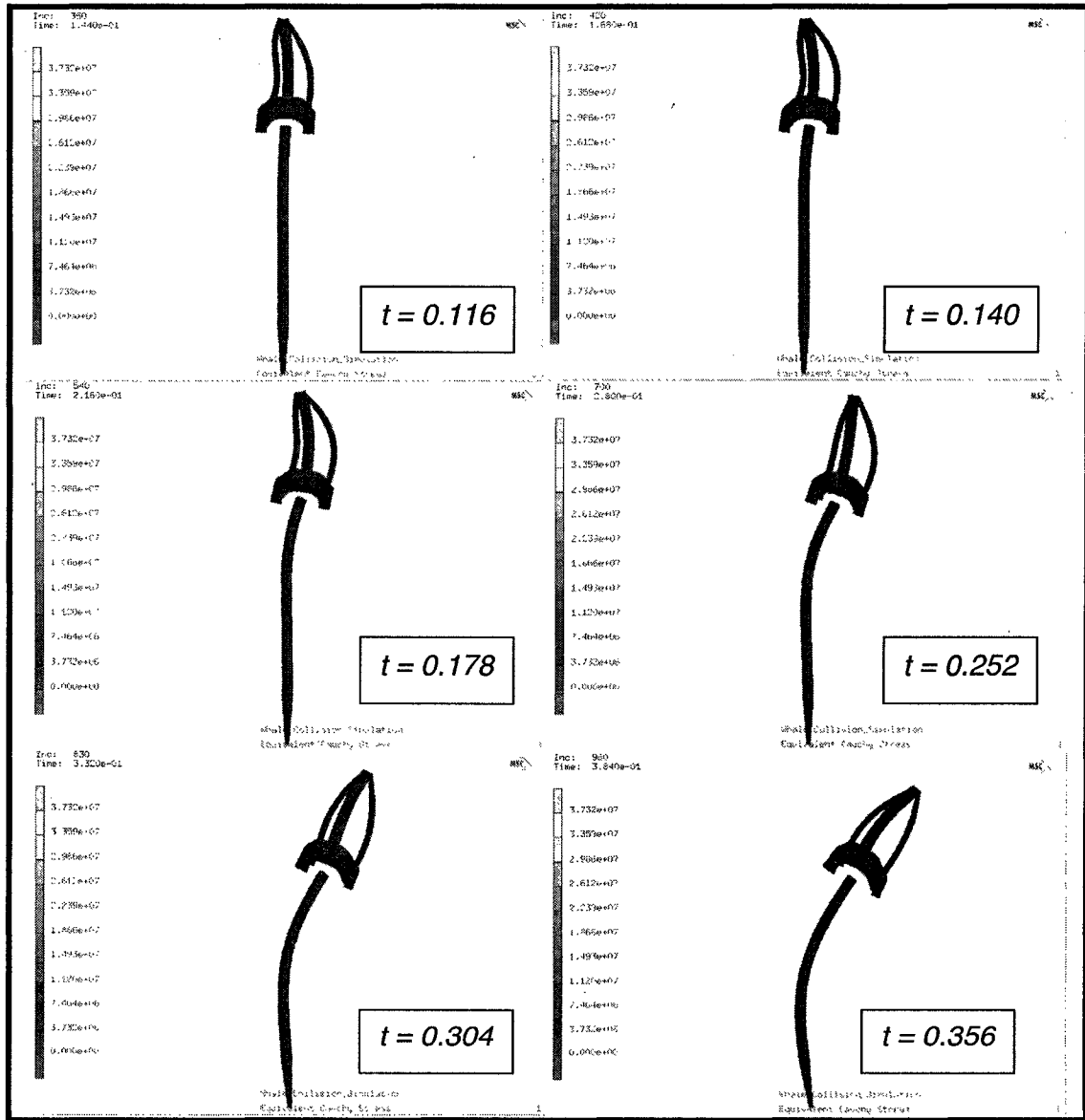
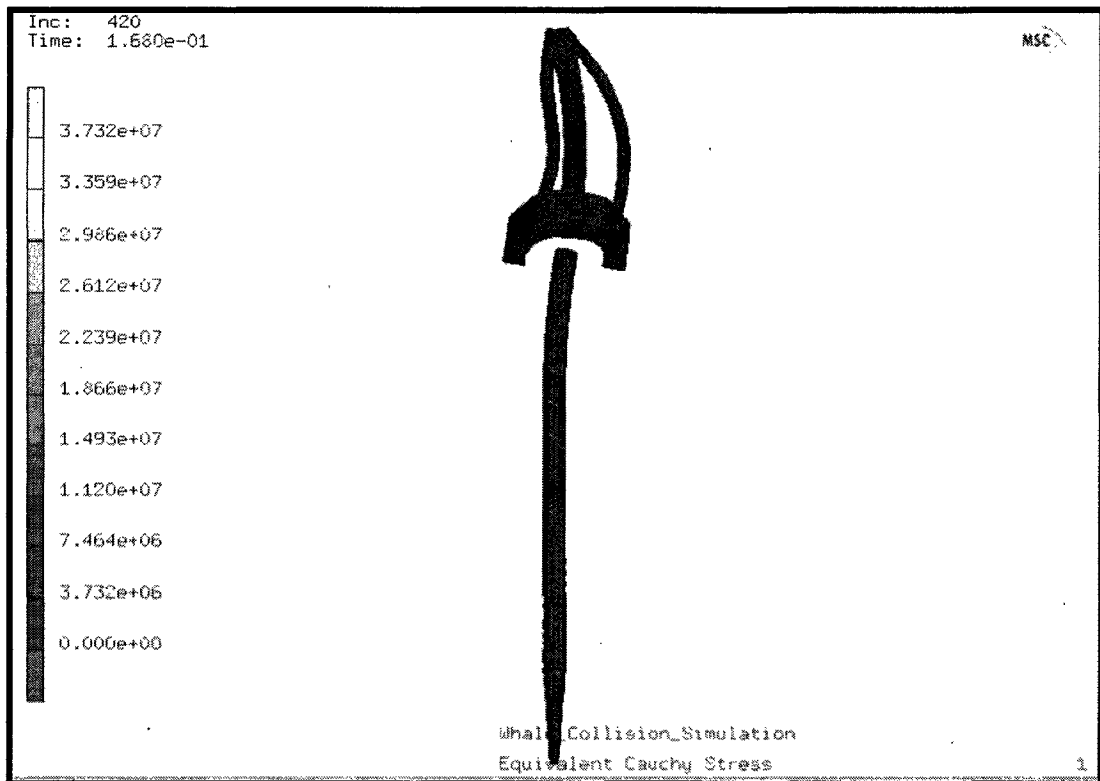


Figure 5.6. 15-knot direct impact collision progression, deformation of skeleton.



**Figure 5.7.** 15-knot direct impact, skeleton maximum stress at t=0.140 sec.

By considering the time increment when maximum load occurs, the maximum pressure load within the bone was evaluated. This was used to determine the load to be applied to the more detailed model of the right whale mandible bone. The maximum compressive stress in the mandible for this load case was -11.67 MPa.

The next set of images, shown in figure 5.8, demonstrates how the stresses propagate through a cross-section of the whale. This cross-section was taken at the plane that the ship impacts the whale. The gray portions represent areas that were above the maximum stress range being plotted. Since the stress in the bone was much greater than that in the soft tissue, a lower stress range was reported to provide the stress contours within the soft tissue. Note that for

convenience of presentation, the stresses are shown with respect to the initial, undeformed configuration of the cross-section. Figure 5.9 shows the cross-section at the point of maximum stress in the mandible.

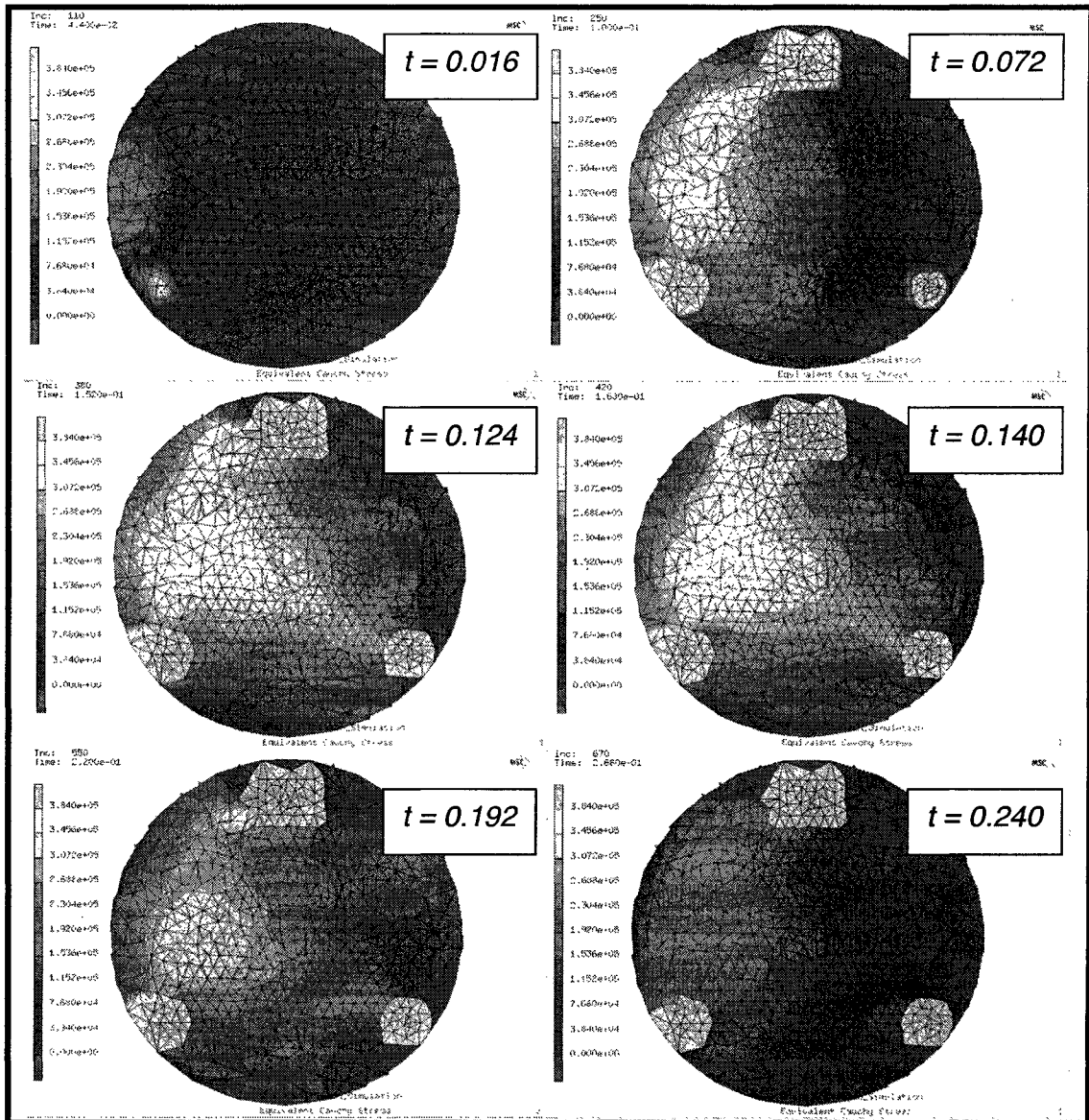
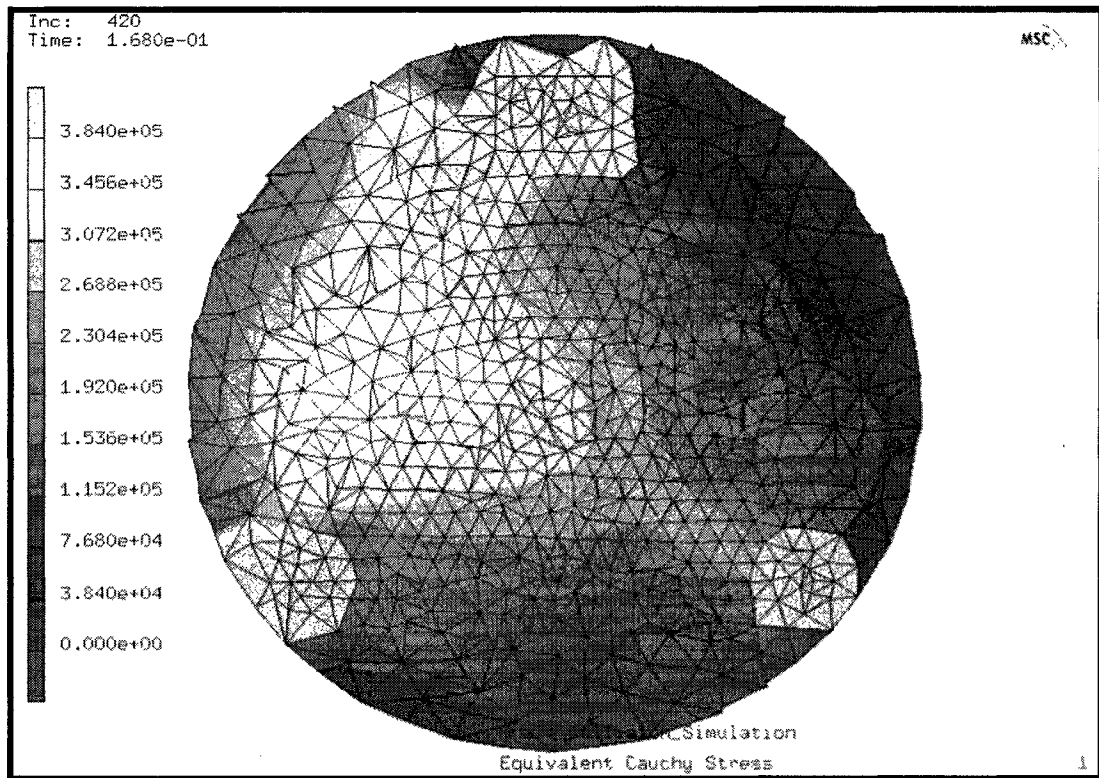


Figure 5.8. 15-knot direct impact collision progression, whale cross-section.



**Figure 5.9.** 15-knot direct impact, cross-section maximum stress at  $t=0.140$  sec.

It was clear that the bones act as stress risers during impact. Thus one may expect that extended damage occurs in the soft tissue surrounding them. Investigation of this stress concentration would require refined meshing and usage of more accurate soft tissue material models. However, the focus of the present numerical study was on the forces transmitted to the bone. These forces were derived from the simulations using the procedure outlined above. Please note that the experimental soft tissue studies of Campbell-Malone and Myers (2006) have not been processed to obtain the adequate right whale fibroelastic tissue failure criterion.

### **5.2.2. 10-knot direct impact collision results**

The second load case has the same relative initial positions of the whale and ship. In this case, however, the initial speed of the ship was reduced to 10 knots. The approach characteristics with regard to impact direction and location are the same. Figure 5.10 shows a progression of images through the duration of the collision event. The maximum impact load occurs at 0.164 seconds. Figure 5.11 shows a larger image for the time increment at maximum impact force.

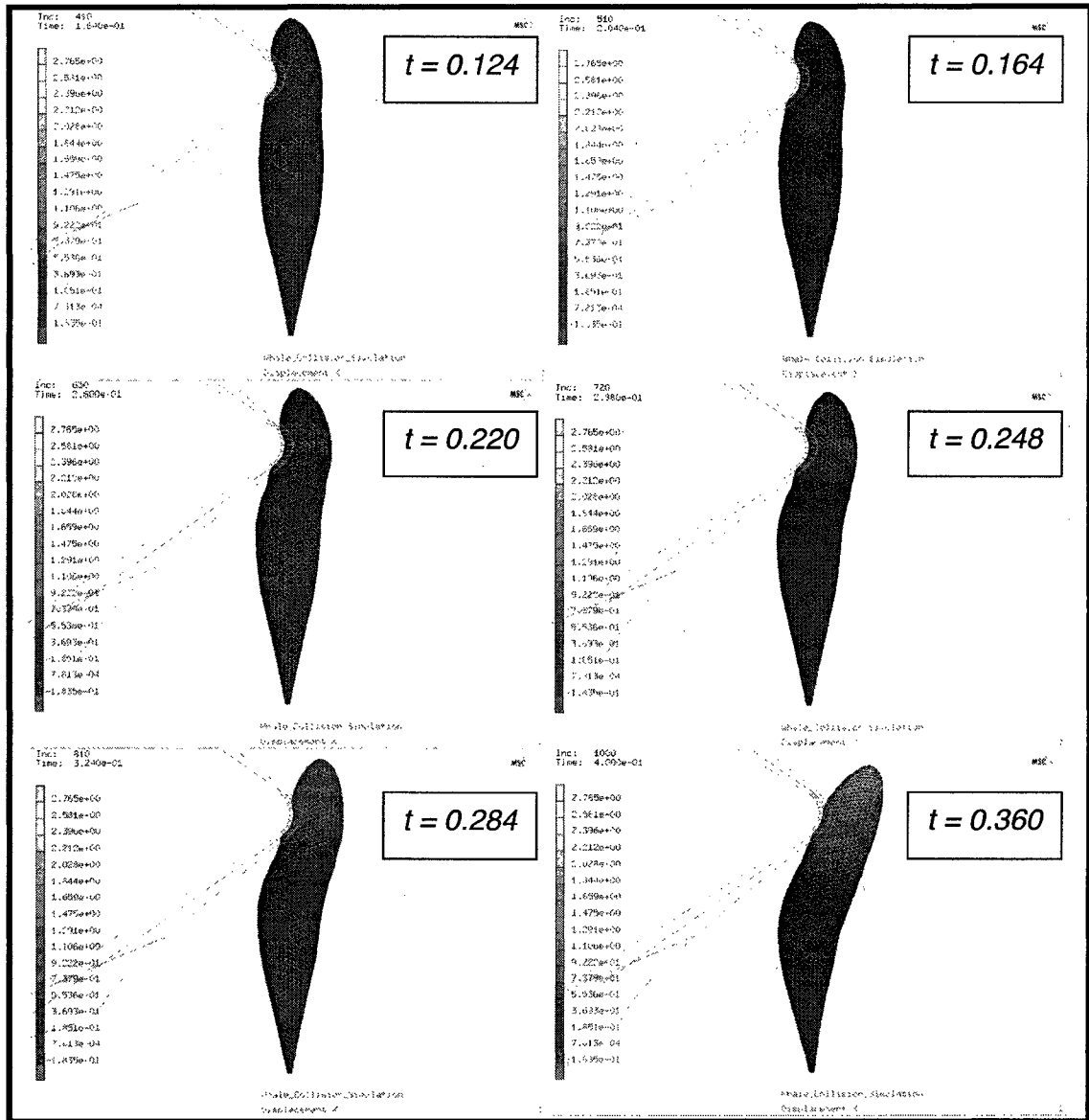
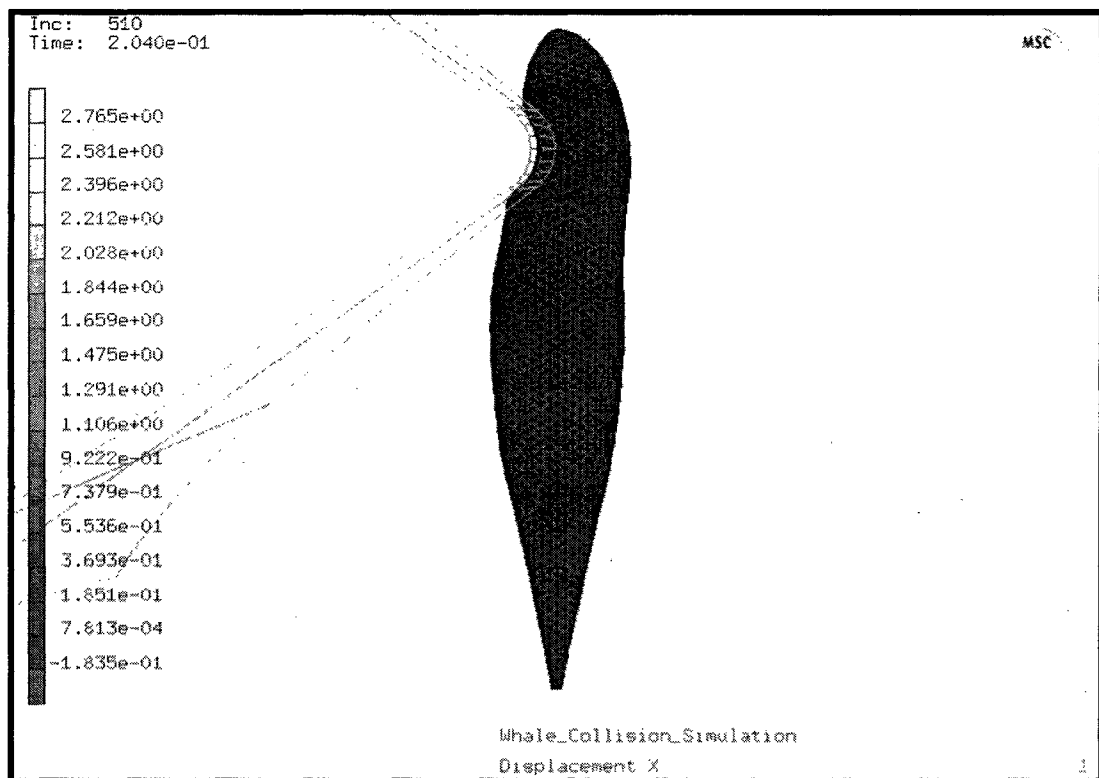


Figure 5.10. 10-knot direct impact collision progression, full whale model.





**Figure 5.11.** 10-knot direct impact, full whale maximum stress at  $t=0.164$  sec.

As expected, the lower impact velocity causes less local deformation at the contact location, resulting in less stress in the mandible bone. Once again it was observed that the head begins to move before maximum load was developed in the mandible. This motion was minimal and would not result in significant drag force. Therefore, the assumption that drag does not affect results still applies.

Figure 5.12 shows the response of the whale skeleton for the 10-knot collision simulation. Figure 5.13 shows the time increment at which maximum stress occurs in the mandible bone.

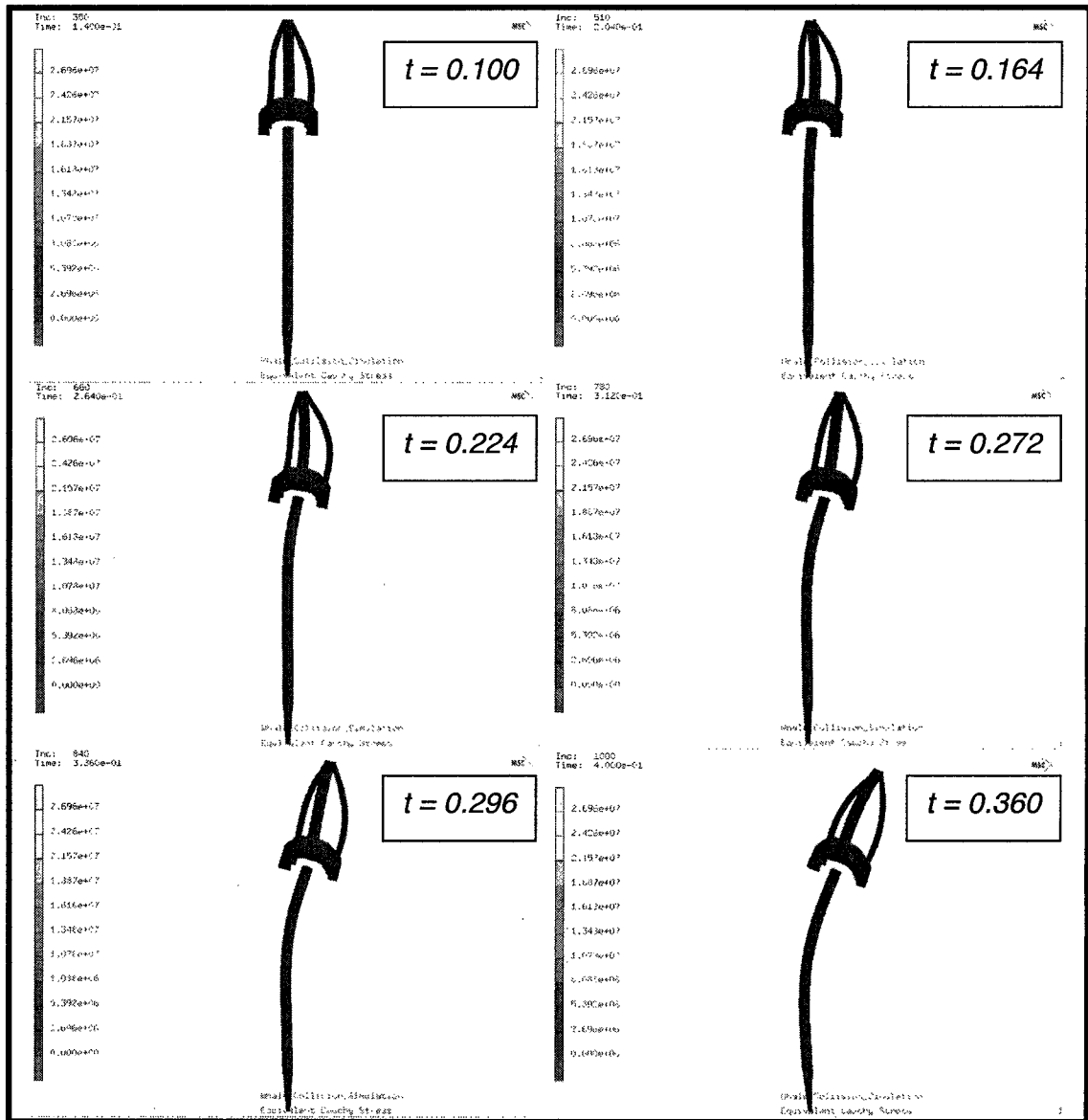
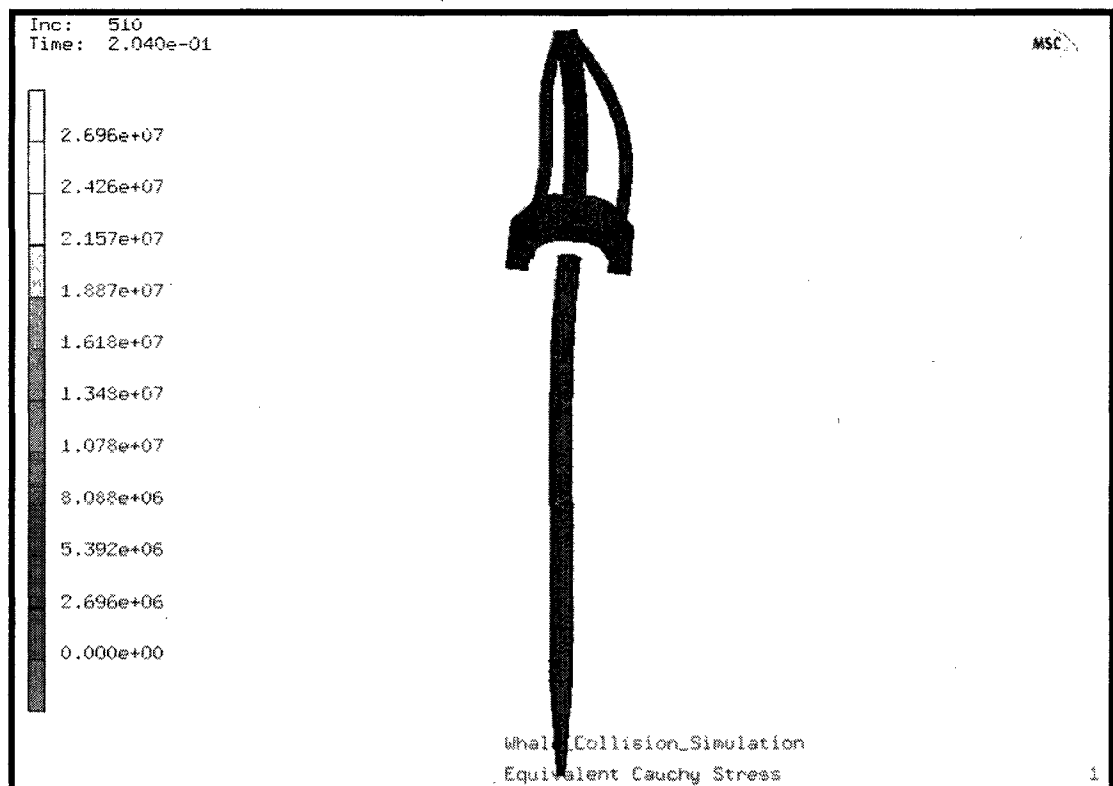


Figure 5.12. 10-knot direct impact collision progression, deformation of skeleton.



**Figure 5.13.** 10-knot direct impact, skeleton maximum stress at  $t=0.164$  sec.

Once again, comparing these results to that of the 15-knot load case, it was seen that the deformation in the bone was less. The resulting compressive pressure load on the bone was  $-7.89$  MPa. This is about 68% of the load magnitude for the 15-knot load case.

### **5.2.3. 5-knot direct impact collision results**

The third load case considered was again similar to the previous two load cases. The approach characteristics were the same, only the approach velocity was reduced to 5 knots. Because the velocity was reduced, the duration of the simulation was increased to 0.8 seconds to ensure that the pertinent information from the collision event was captured. Figure 5.14 shows the results for this load case. The maximum load occurs at a time of 0.296 seconds, shown in figure 5.15.

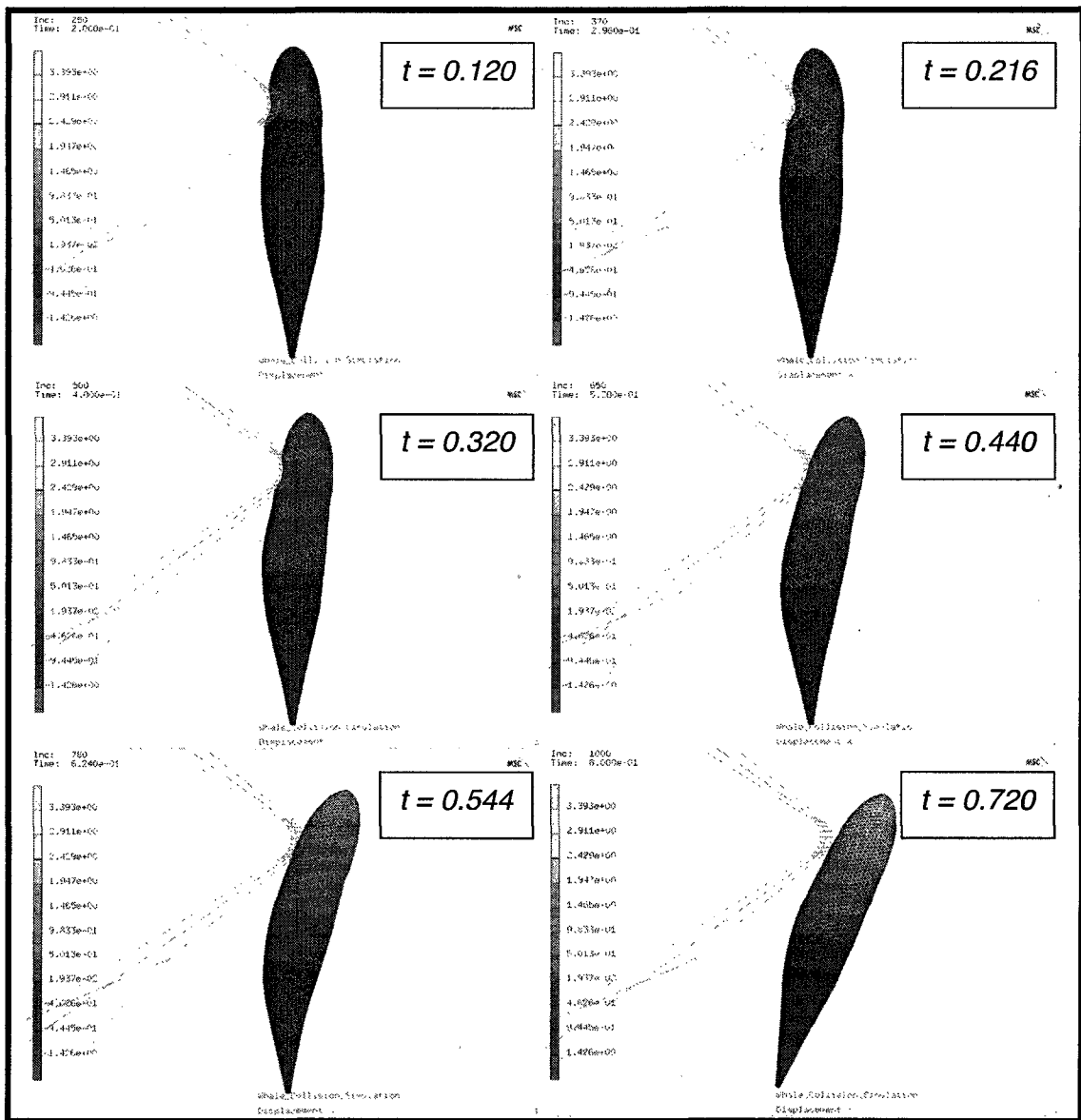


Figure 5.14. 5-knot direct impact collision progression, full whale model.

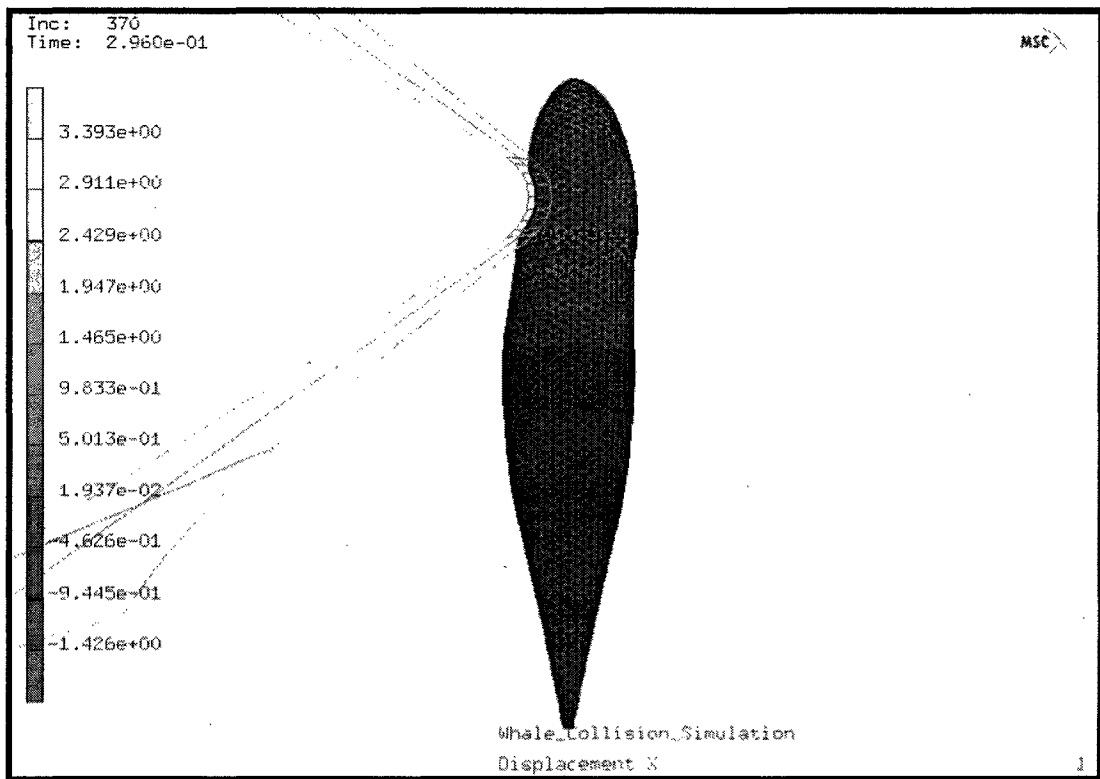
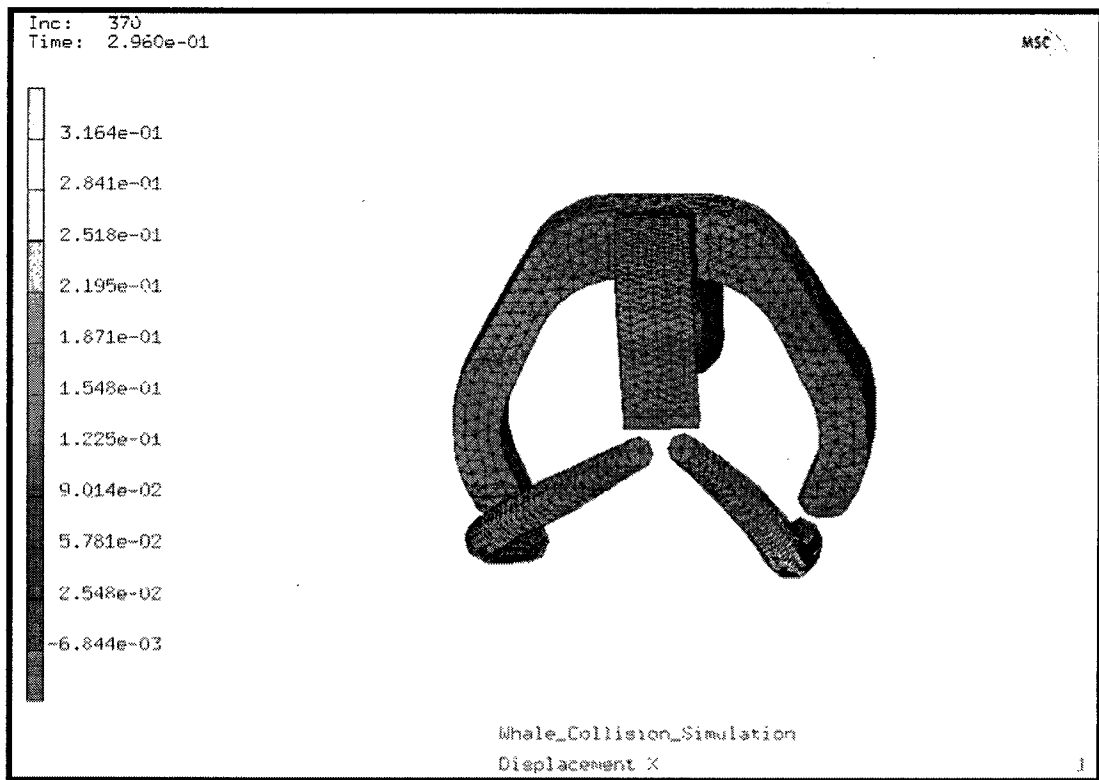


Figure 5.15. 5-knot direct impact, full whale maximum stress at t=0.216 sec.



Figure 5.16. 5-knot direct impact collision progression, deformation of skeleton.



**Figure 5.17. 5-knot direct impact, skeleton maximum stress at t=0.216 sec.**

Figure 5.17, presenting the time increment of maximum impact force, highlights that, even for the reduced velocity, the whale does not experience significant rigid body motion prior to reaching maximum stress within the mandible bone.

#### **5.2.4. 15-knot indirect impact with greater hull draft**

The fourth load case considers a vessel with a much greater draft. This greatly changed the dynamics of the collision event. This change was apparent upon review of figure 5.18, which shows the progression of the collision throughout the duration of the event. If this progression is compared to the previous three load cases, it is seen that the impact results in much different dynamics of the whale.

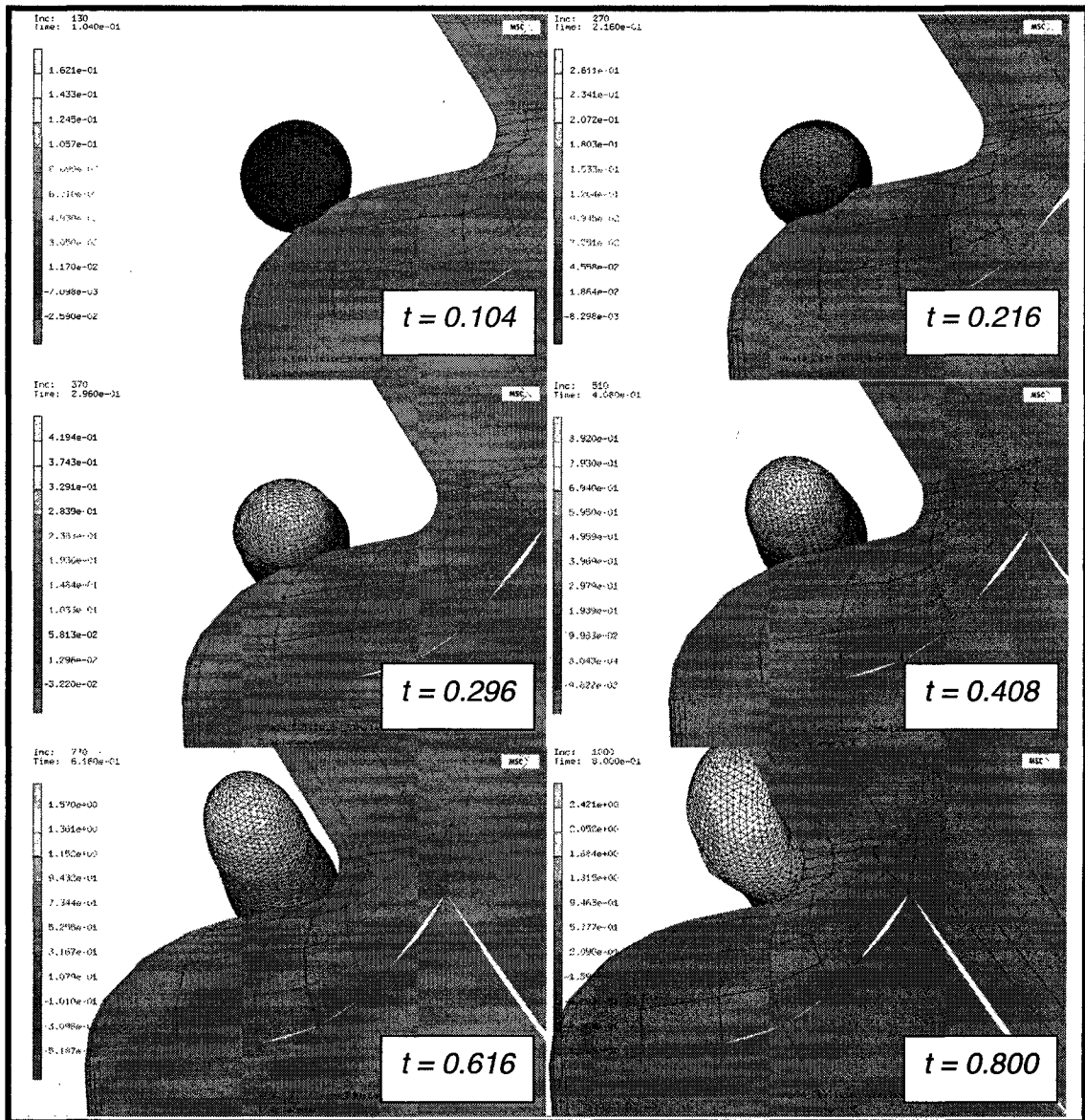


**Figure 5.18.** 15-knot indirect impact collision progression, full whale model.

This result highlights the type of condition that would require consideration of the other forces involved in a dynamic situation. The forces include drag, gravity, and buoyancy. As stated earlier, it has been assumed that for the direct impact load cases that these forces were negligible. By noting how the whale, upon initial contact, experienced upward motion before coming into contact with the hull for a second time, the effect of neglecting the drag and gravitational



forces was seen. Figure 5.19 shows the reaction of the skeleton to this impact scenario.

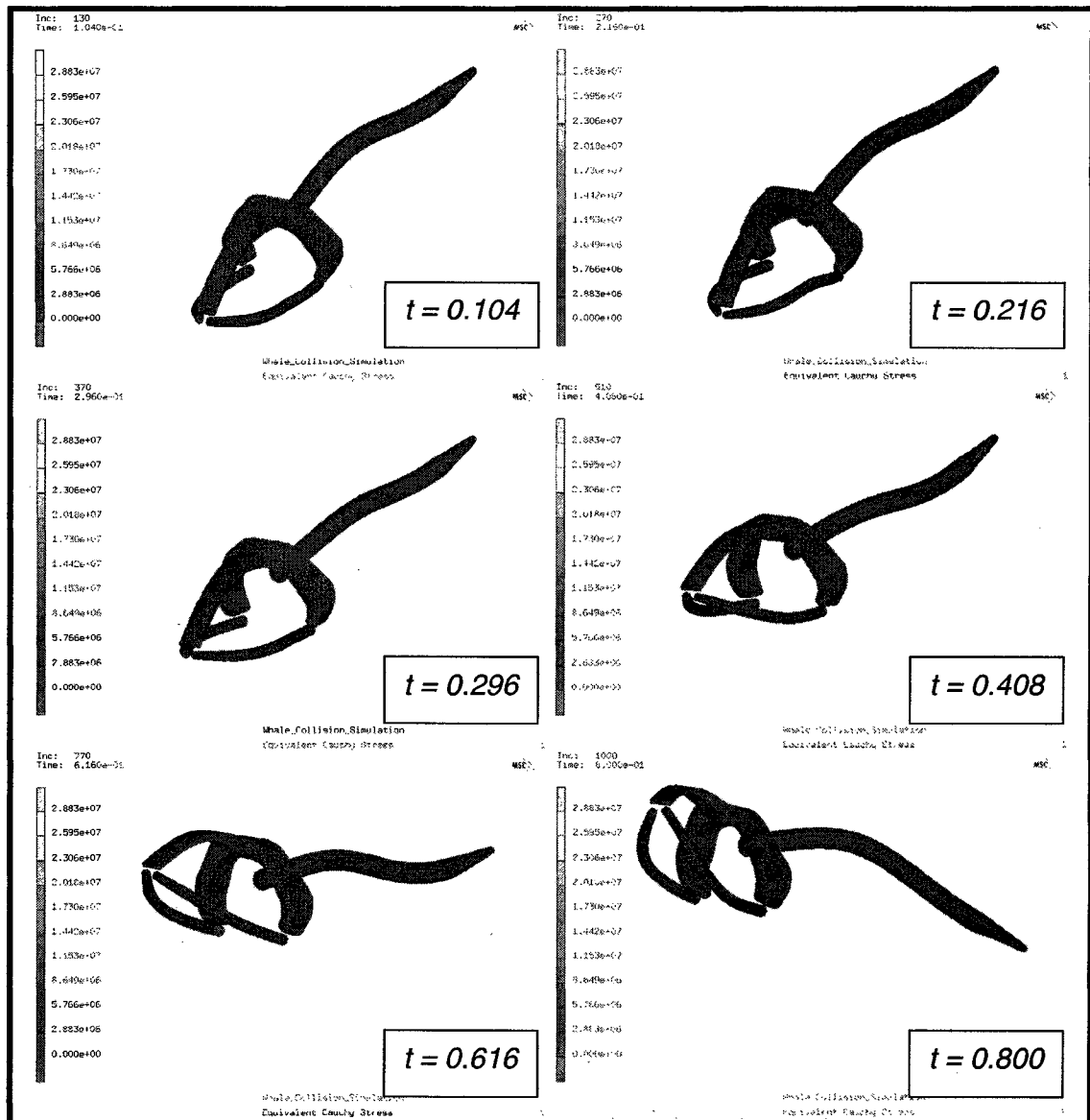


Figure 5.19. 15-knot indirect impact collision progression, skeleton deformation.

### 5.3. Contact forces and overall dynamics of collision

A comparison between the three direct impact load cases was desired to evaluate the effects of changing vessel impact velocity. Figure 5.20 below is a graph showing the total impact forces for each load case, plotted over the

duration of the collision event. As expected, the maximum impact force increases with increasing impact velocity.

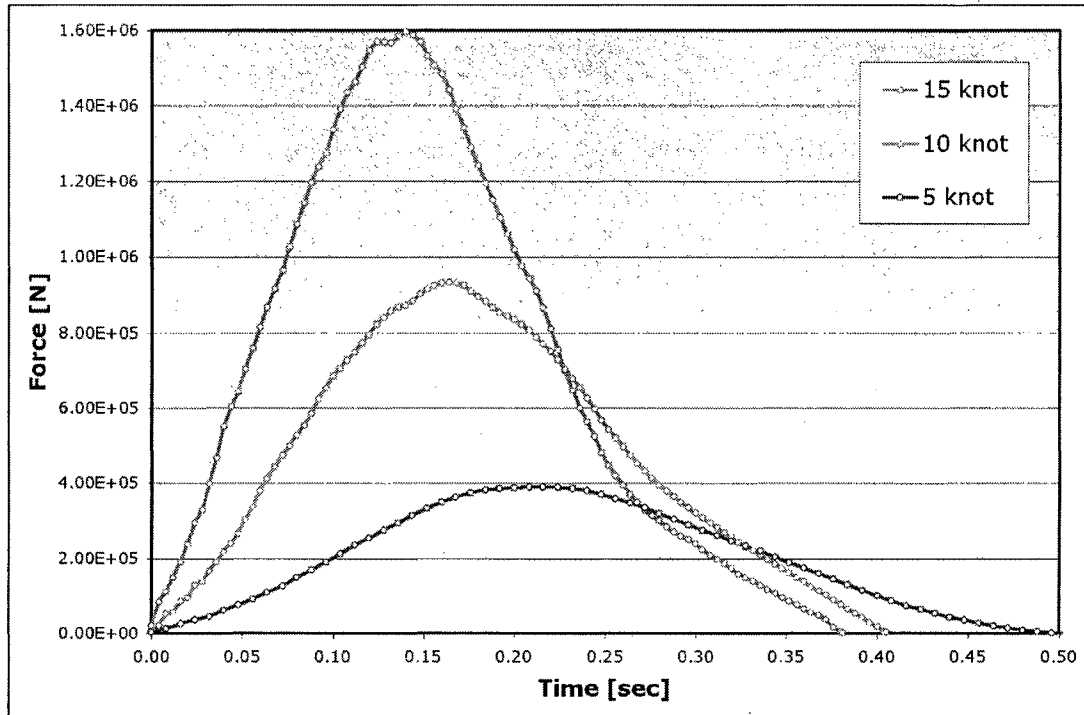


Figure 5.20. Comparison of maximum impact force for direct impact load cases.

The effects of buoyancy and fluid drag were not considered in the simulations described in this work. The assumption was made that inertia has the greatest overall effect on collision dynamics, and that the other dynamic factors do not play a significant role. Analysis of the results for the three direct impact load cases shows that this assumption was satisfactory for the range of impact velocities considered. Figures 5.21 through 5.23 show a comparison between impact force, displacement at the point of impact, and displacement at a point opposite the impact area over the collision duration. Displacement at the location opposite of the impact area gives an indication of when the impact force overcomes the inertia of the whale, at which point the whale begins to move

through the water. Significant motion of the whale would suggest that drag force may need to be considered.

Review of figures 5.21 through 5.23 reveals that in all considered cases the maximum impact force was reached before the whale develops any significant motion. The largest displacement at the instant of maximum impact force occurs for the 15-knot load case. This displacement was about 0.5 meters. This distance is not significant when compared to the local displacement of about 1.2 meters at the point of impact. Since drag force is proportional to velocity-squared, and no significant motion was developed at the point of maximum impact force, it is inferred that negligible drag force is involved.

It was observed that, after the point of maximum force was reached, the whale began to rebound and move away from the hull. This was due to the elastic characteristics of materials used in the simulations. Implementation of a nonlinear soft tissue model, such as the Ogden model, along with the addition of drag forces, would result in an inelastic collision model. Such a model would more accurately predict behavior of the vessel-whale system after the initial collision. However, this behavior would not occur until after maximum load was reached, so omission of these non-elastic effects does not affect the prediction of the highest impact forces.

The fourth load case, which considers a vessel with a much greater draft, highlights what conditions might require a more thorough investigation of the effects of gravity, buoyancy, and drag forces.

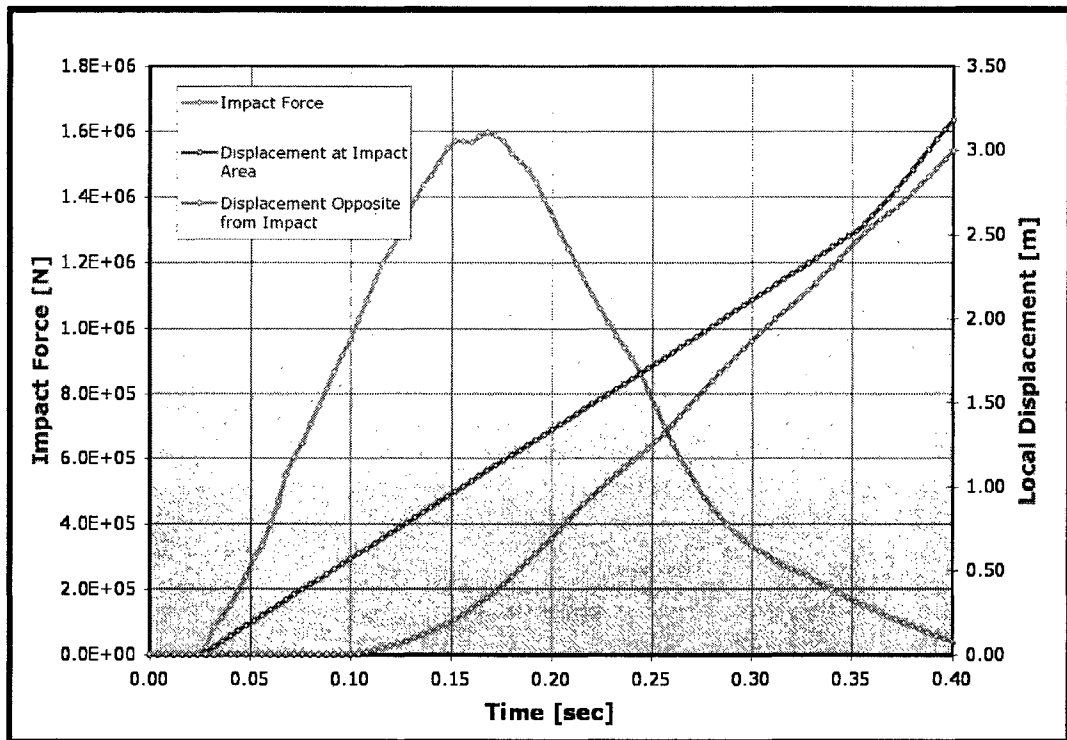


Figure 5.21. Comparison of impact force to whale displacement during 15-knot collision event.

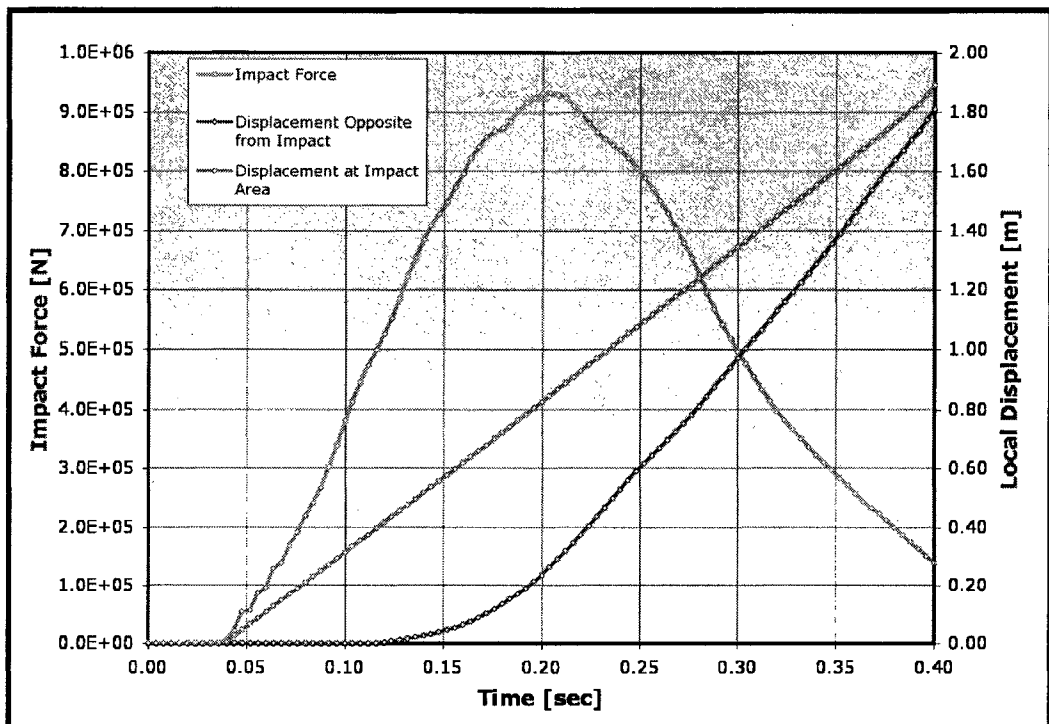


Figure 5.22. Comparison of impact force to whale displacement during 10-knot collision event.

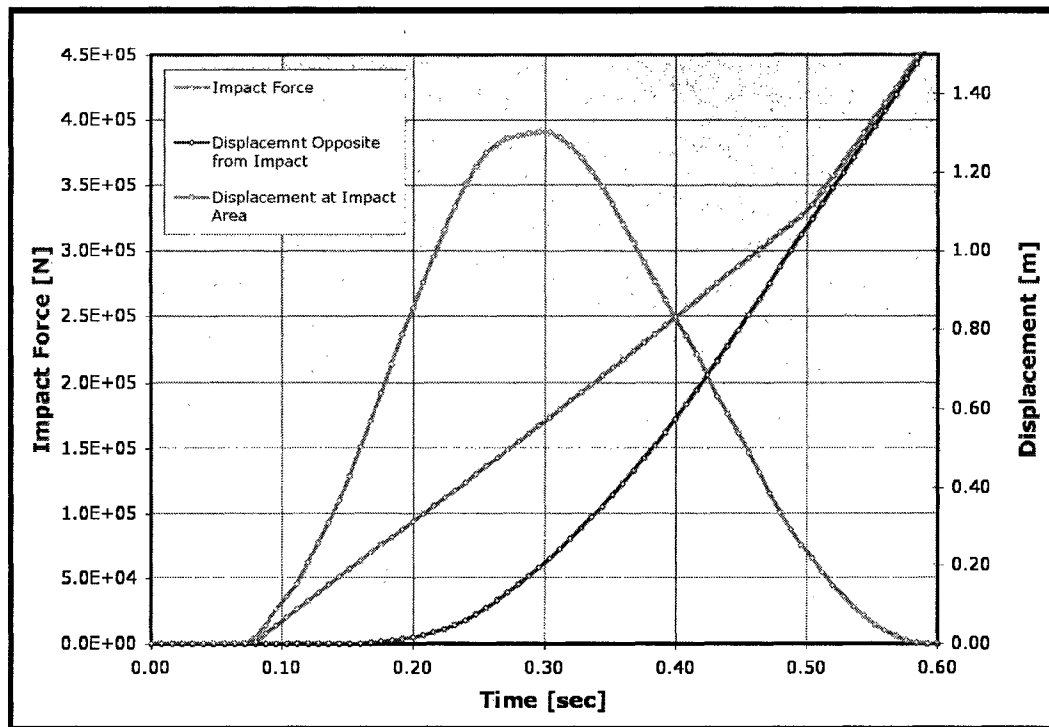


Figure 5.23. Comparison of impact force to whale displacement during 5-knot collision event.

#### **5.4. Comparison of simulation results to classical dynamics solution**

Many researchers use the principle of conservation of linear momentum, as described in section 1.4, to estimate average contact forces during a ship-whale collision event (Vanderlaan and Taggart, 2006). By using the numerical simulations to determine the duration of the collision, an estimation of these forces using classical methods can be obtained and compared to the impact forces directly extracted from the simulations. It was assumed that the ship velocity was unchanged by the collision. The mass of the whale and ship were defined as follows:

$$m_{\text{whale}} = 46,621 \text{ kg}$$

$$m_{\text{ship}} = 311,189 \text{ kg,}$$

It should be noted that in the numerical simulation the vessel was represented as a rigid body with infinite mass.

The collision duration for each load case was defined between the point of initial contact and the point of contact separation. For cases where the simulation did not have long enough duration to capture the contact separation, the total impact duration was estimated. As seen in figures 5.21 through 5.23, the impact curve becomes nearly linear near the end of the simulation. Interpolation of the linear portion of the impact curve was used to estimate the time at which the impact force reached zero, indicating separation of the bodies. This value was used to determine the total impact duration. Table 5.2 is a summary of results from both the numerical simulations and calculations using classical methods.

**Table 5.2.** Summary of collision duration and impact force for direct impact load cases.

Load Case	Impact Duration [sec]	Average Force (estimated) [N]	Average Force (simulation) [N]	Peak Force (simulation) [N]	Percent Difference [%]
15-knot	0.381	9.45e5	6.99e5	15.96e5	41
10-knot	0.417	5.75e5	4.62e5	9.32e5	38
5-knot	0.504	2.38e5	1.94e5	3.90e5	39

The column labeled “Average Force (estimated)” is the results from the methods described in chapter 1.4. The “Average Force (simulation)” column represents the average force from all time steps of the simulation for which contact occurs. The “Peak Force (simulation)” column gives the peak force that occurs during the collision event. Percent difference compares the average calculated force to the peak force of the simulation. Review of the table shows that the classical dynamics approach provides a reasonable estimate of average contact forces, but underestimates the peak force by 39-41%.

## CHAPTER 6

### CONCLUSIONS AND RECOMMENDATIONS

The results obtained from the simulations presented in this work indicate the effect of ship speed on maximum impact force in a right whale. As expected, impact force increases with increased velocity. Numerical modeling provides a quantitative value for the magnitudes of these forces.

Using the procedure defined in this thesis, the impact force was converted into an average impact stress that can be used as input for the detailed mandible bone numerical model. With this data, the simulation can be performed to determine the failure point of the mandible. The load resulting in mandible failure can then be correlated to the impact force, and ultimately to the vessel approach speed. This data can be used to make informed decision regarding effective regulation of vessel speed in critical right whale habitats.

#### **6.1. Observations from modeling**

Since the main goal of this work was to generate loads for detailed mandible analysis, the most important observation was in regards to the relationship between vessel approach velocity and maximum impact force. This relationship is shown graphically in figure 6.1. This graph was generated using data from numerical simulations for 5, 8, 10, 12, and 15 knot vessel approach speed collision scenarios.

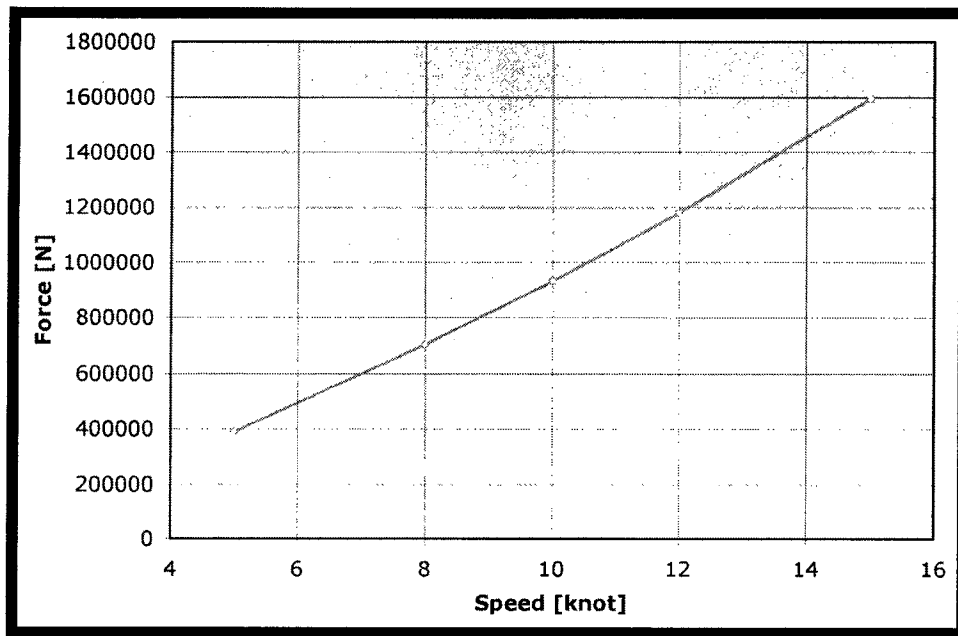


**Figure 6.1.** Plot representing maximum impact force relative to vessel approach speed.

As evidenced by this figure, results of the numerical simulations show an approximately linear relationship between vessel approach speed and total impact force. This result was expected based on the implementation of linear elastic material models to estimate the mechanical behavior of both the whale skeleton and soft tissue. The deviation from linear dependence is caused by inertia effects and changes in total impact times for various vessel approach speeds. The approximate linearity of this relationship tells us that the average impact stress, as determined in accordance with chapter 5.1.2, can be used to estimate forces for any vessel approach velocity desired.

## **6.2. Future work**

Major directions for future work include refinement of the whale model and introduction of additional hydrodynamic parameters. The present whale model was suitable for the simulations discussed above. However, for generating



simulations of a wider range of collision scenarios, a more detailed model may be required. The following sections provide a brief description of some of the areas for possible consideration. Once these considerations are evaluated and implemented, the numerical model will be better suited for a broader range of collision scenarios.

#### **6.2.1. Whale external geometry**

The whale geometry used for these simulations had a number of simplifying assumptions. One of them was the homogeneity of the soft tissue that occupies all space around the skeleton. This does not account for the distribution of mass within the whale due to such things internal organs and void spaces.

An example of this was the space between the rostrum and mandibles, which makes up the mouth of the whale. This area is not made up of continuous soft tissue. There is void space, which reduces the mass in this area of the whale as compared to the numerical model. Modifying the model to represent the reduced mass may help to obtain convergence with implementation of the Ogden soft tissue model. By reducing the mass at the point of collision, the impact force has a better chance of overcoming inertia before the excessive deformation occurs in the finite element mesh, which was the condition that results in solution divergence.

#### **6.2.2. Soft tissue model**

As discussed in chapter 2.2.5, the simulations required an equivalent linear elastic soft tissue model to achieve successful solution convergence. One of the main factors contributing to this was the lack of sufficient fibroelastic soft

tissue experimental data. With additional testing, a more robust set of data could be obtained, resulting in an improved constitutive model to represent the whale soft tissue. The present material model was generated using only uni-axial compression data. With additional data for various modes of deformation, a set of material parameters that more accurately represent the material behavior under complex loading can be obtained.

### **6.2.3. Skeletal model**

The present skeletal model was appropriate for the simulations focused on mandible fracture as the fatal endpoint. However, for consideration of additional fatal endpoints, a modified skeletal structure may be required. For example, if the effect of impact forces on the ribs is desired, the skeletal model would need to be modified to include a sufficient representation of the whale rib cage, making sure that the thickness of the soft tissue surrounding the ribs is accurately represented.

### **6.2.4. Dynamic and gravity forces**

As stated in previous sections, drag, buoyancy, and gravity forces were not included in the numerical simulations. As discussed in chapter 5.3, this was sufficient for the direct impact collision scenarios considered in this work. However, this may not be valid for other possible load cases. An example of such a scenario is the indirect impact case discussed in chapter 5.2.4. This scenario resulted in significant motion of the whale in the vertical direction. To accurately capture the dynamics of this motion, the models should include gravitational and buoyancy forces.

### **6.3. Implications for predicting fatal whale bone fractures**

Future work discussed in the previous section addresses possible modifications and improvements to the present numerical simulation of vessel-whale collision. Though this work estimates the resulting impact force in the right whale mandible during collision, this is only the first step in a larger effort to establish which collision scenarios lead to fatal whale bone fractures. The simplified mandible representation in this model does not give enough information to accurately predict distribution of stresses within the mandible. Therefore, the vessel approach speed resulting in mandible fracture cannot be determined from this study alone. To determine the collision scenarios that result in fracture, the impact forces estimated in this study need to be applied to a detailed finite element model of the mandible as outlined in (Tsukrov et al., 2006). This detailed model was created using a more accurate geometry and includes information regarding distribution of bone densities and material properties within the mandible. Use of this model will give a better indication of peak stresses within the mandible caused by collision. These stresses are then compared with the experimentally obtained failure stresses of the bone material to determine the impact force that results in mandible fracture. The force can then be correlated to vessel approach speed using the findings of the numerical collision simulation results.

## REFERENCES

Bathe, K-J, 1996. Finite Element Procedures. Prentice-Hall, Inc., Upper Saddle River, NJ.

Campbell-Malone, R., 2007. Biomechanics of North Atlantic Right Whale Bone: Mandibular Fracture as a Fatal Endpoint for Blunt Vessel-Whale Collision Modeling. Ph.D. dissertation. Woods Hole Oceanographic Institution, Woods Hole, MA.

Campbell-Malone, R., Barco, S. G., Daoust, Pierre-Yves, Knowlton, A. R., McLellan, W. A., Rotstein, D. S., Moore, M. J., 2006. Sharp and blunt trauma in North Atlantic right whales killed by ships. *Journal of Zoo and Wildlife Medicine*. 35 pages. In press.

Campbell-Malone, R., Myers, K., 2006b. Mechanical behavior of epidermal and fibroelastic tissue from the North Atlantic right whale (*Eubalaena glacialis*). Unpublished raw data.

Blue, J.E., Gerstein, E.R., Forsythe, S.E., 2001. Ship strike acoustics: It is all shadows and mirrors. *Journal of the Acoustical Society of America* 110:2723.

Hibbeler, R. C., 1998. *Engineering Mechanics; Dynamics*, 8<sup>th</sup> Edition. Prentice-Hall, Inc. Upper Saddle River, NJ.

Knowlton, A. R., Korsmeyer, F.T., Hynes, B. 1998. The Hydrodynamic Effects of Large Vessels on Right Whales: Phase Two. Final Report to the National Marine Fisheries Service, Northeast Fisheries Science Center, Woods Hole, MA, under contract no. 40EANFF400534. 31 pages plus 60 figures and 3 appendices.

Laist, D.W., Knowlton, A.R., Mead, J.G., Collet, A.S., Podesta, M., 2001. Collisions between ships and whales. *Marine Mammal Science* 17(1), 35-75.

Moore, M.J., Campbell-Malone, R., 2003. Final Large Whale Necropsy Report Eg2150.

Moore, M.J., Knowlton, A.R., Kraus, S.D., McLellan, W.A., Bonde, R.K., 2005. Morphometry, gross morphology and available histopathology in North Atlantic right whale (*Eubalaena glacialis*) mortalities (1970-2002). *Journal of Cetacean Research and Management* 6(3), (in press).

MSC Software Publication, 2005a.  $F \neq \text{equal } ku$ .

MSC Software Publication, 2005b. MSC.Dytran User's Guide, Version 2005.

MSC Software Publication, 2005c. Nonlinear finite element analysis of elastomers.

MSC Software Publication, 2005d. MSC.Marc Volume A: Theory and user information.

Tsukrov, I., Baldwin, K., DeCew, J., Raymond, J., 2006. Finite element modeling of a right whale mandible strength and ship whale collision dynamics. Final report to Woods Hole Oceanographic Institution. University of New Hampshire, Durham, NH.

Vanderlaan, A.S.M., Taggart, C.T., 2006. Vessel collisions with whales: The probability of lethal injury based on vessel speed. Marine Mammal Science. In press.

[www.algor.com](http://www.algor.com)